The University Of Sheffield.

Miniaturization and Optimization of Electrically Small Antennas, with Investigation into Emergent Fabrication Techniques

A THESIS SUBMITTED TO
THE DEPARTMENT OF ELECTRONIC AND ELECTRICAL ENGINEERING
FACULTY OF ENGINEERING
UNIVERSITY OF SHEFFIELD
FOR THE DEGREE OF
DOCTOR OF PHILOSOPHY

By
Saad Mufti

December 2017

(This page intentionally left blank.)

Abstract

With the paradigm shift in personal communications favouring wireless over wired, the demand for efficient, low-cost, and compact antennas is booming. The proliferation of mobile electronic devices (laptops and tablets, fitness trackers, ‘smart’ phones and watches), together with the desire for longer battery life, poses a unique challenge to antenna designers; there is an unavoidable trade-off between miniaturization and performance (in terms of range and efficiency).

The size of an antenna is inherently linked to the wavelengths(s) of the electromagnetic waves that it must transmit and/or receive. Due to real-estate pressures, most modern antennas found in electronics are classed as electrically small, i.e. operating at wavelength(s) many times greater than their largest dimension. Theory dictates that the best possible compromise between size and performance is achievable when an antenna fully occupies a volume, the radius of which is defined by an imaginary sphere circumscribing its largest dimension.

This Thesis demonstrates the design and optimization of low-cost, easy-to-fabricate, electrically small antennas through the integration of novel digitated structures into a family of antennas known as inverted-F. The effects of these digitated structures are catalogued using simulated models and measured prototypes throughout.

Whereas the limitations of traditional industrial processes might once have constrained the imaginations of antenna designers, there is now tremendous potential in successful exploitation of emergent manufacturing processes – such as additive manufacturing (or 3D printing) – to realize complex, voluminous antenna designs.

This Thesis also presents pioneering measured results for three-dimensional, electrically small antennas fabricated using powder bed fusion additive manufacturing. The technology is demonstrated to be well suited for

prototyping, with recommendations provided for further maturation. It is hoped that these promising early results spur further investigation and unleash bold new avenues for a new class of efficient, low-cost, and compact antennas.

Acknowledgements

I would like to express my heartfelt gratitude for every person that has contributed to this project and provided their support – from my doctorate applications to the writing of this Thesis.

First and foremost, I want to thank my two supervisors, Professor Alan Tennant and Doctor Luke Seed. I deeply appreciate their contributions to my funding along with the Department, and their wisdom, ideas and general mentorship. I am especially grateful for their confidence in me, and for granting me the freedom to explore many projects and ideas.

I would also like to thank Doctor Jonathan Rigelsford for his benevolent aid with antenna measurements and publications, Doctor Gavin Williams for imparting his knowledge of all matters relating to the clean room laboratory, Doctor Christopher Smith for printing 3D antennas, and all the countless other academics, researchers, lab assistants, and administrative staff for their support and cooperation. Thanks also to my colleagues and friends from the Department and beyond, indeed all over the world, for their intellectual engagement and for all the moments of shared joy and laughter.

My sincerest thanks go to my dad, Tahir Mufti, and my mom, Doctor Naira Siddiqi. Their unconditional love and steadfast support is akin to a perennial lighthouse, allowing me the courage to tread uncharted waters.

Finally, it is *my* privilege to thank my wife and partner Tabitha Mufti, for her constant love and encouragement, and especially for her invaluable help with the preparation of this Thesis.

(This page intentionally left blank.)

List of Publications

The following is a list of peer reviewed publications based on the work presented in this Thesis:

S. Mufti, C. Smith, A. Tennant, and L. Seed "Selective Electron Beam Melting Manufacturing of Electrically Small Antennas", *Advances in Science, Technology and Engineering Systems Journal*, vol. 2, no. 6, pp. 70-75, 2017.

S. Mufti, A. Tennant, L. Seed, and C. J. Smith, "Efficiency measurements of additive manufactured electrically small antennas," *International Workshop on Antenna Technology: Small Antennas, Innovative Structures, and Applications*, Athens, 2017, pp. 347-349.

S. Mufti, C. J. Smith, A. Tennant, and L. Seed, "Improved efficiency electrically small planar inverted-F antenna," *10th European Conference on Antennas and Propagation*, Davos, 2016, pp. 1-4.

S. Mufti, A. Tennant, and L. Seed, "3D printed electrically small planar inverted-F antenna: Efficiency improvement through voluminous expansion," *IEEE International Symposium on Antennas and Propagation*, Fajardo, 2016, pp. 811-812.

S. Mufti, A. Tennant and L. Seed, "Electrically small modified planar inverted-F antenna," *9th European Conference on Antennas and Propagation*, Lisbon, 2015, pp. 1-4.

S. Mufti, A. Tennant and L. Seed, "3D electrically small dome antenna," *Loughborough Antennas and Propagation Conference*, Loughborough, 2014, pp. 653-656.

S. Mufti, G. Williams, A. Tennant and L. Seed, “Design and fabrication of meander line antenna on glass substrate,” *Loughborough Antennas & Propagation Conference*, Loughborough, 2013, pp. 559-562.

Table of Contents

List of Figures

(This page intentionally left blank.)

List of Tables

(This page intentionally left blank.)

Nomenclature

2D	Two dimensional
3D	Three dimensional
4D	Four dimensional
AM	Additive manufacturing
AUT	Antenna under test
CAD	Computer aided design
CDIFA	Circular, digitated inverted-F antenna
CDPIFA	Circular, digitated planar inverted-F antenna
CGH	Computer generated hologram/holographic/holography
CIFA	Circular inverted-F antenna
CNC	Computer numerical control
CPIFA	Circular planar inverted-F antenna
CPW	Co-planar waveguide
CST MWS	CST Microwave Studio
dB	Decibel(s)
dBi	Decibels over isotropic
DRA	Dielectric resonator antenna
EM	Electromagnetic
ESA	Electrically small antenna
FBW	Fractional bandwidth
GPS	Global positioning system
HIS	High impedance surface
IFA	Inverted-F antenna
ILA	Inverted-L antenna

IoT	Internet of Things
MHDA	Meanderline hemispherical dome antenna
MLA	Meanderline antenna
NIC	Negative impedance converter
PBF	Powder bed fusion
PCB	Printed circuit board
PEC	Perfect Electrical Conductor
PIFA	Planar inverted-F antenna
RF	Radiofrequency
RIFA	Rectangular inverted-F antenna
RL	Return loss
SEBM	Selective electron beam melting
SGA	Standard gain antenna
SLA	Stereolithography apparatus (type of AM)
SLM	Selective laser melting
SNR	Signal-to-noise ratio
STL	Stereolithography
VNA	Vector network analyzer

a	Radius of an imaginary sphere circumscribing the maximum dimension of the antenna
C	Capacitance/capacitor
D	Directivity
FBW_{-3dB}	Half power fractional bandwidth
f_C	Centre frequency
f_h	Upper frequency

f_l	Lower frequency
G	Gain
G_r	Realized gain
k	Wavenumber
L	Inductance/inductor
M	Impedance mismatch factor
P	Polarization mismatch factor
P_{AUT}	Power received by AUT
P_i	Incident signal power
P_{in}	Input (accepted) power
P_r	Reflected signal power
P_{rad}	Power radiated
P_{SGA}	Power received by SGA
Q	Quality factor (of antenna)
Q_{lb}	Lower bound on Q
$Q_{lb\text{-}Chu}$	Lower bound on Q, derived from the work of Chu, Lan Jen
Q_{ratio}	Ratio of quality factor of antenna under test to the fundamental minimum limit on quality factor for an antenna of the same geometry and radiation efficiency
R	Resistance/resistor
R_A	Total resistance of antenna
R_{loss}	Loss resistance
R_{rad}	Radiation resistance
R_S	Source resistance
S_{11}	Ratio of reflected to incident wave voltage at port 1 (in two-port VNA)
S_{21}	Ratio of reflected wave voltage at port 2 to incident wave voltage at port 1 (in two-port VNA)

S_{FS}	S_{11} for antenna in free space
S_{WC}	S_{11} for antenna enclosed in Wheeler cap
tanδ	Loss tangent
U_0	Radiation intensity of an isotropic source radiating the same power as AUT
U_i	Radiation intensity of an isotropic source operating at the same input power as AUT
U_{max}	Maximum radiation intensity
V_i	Incident signal voltage
V_r	Reflected signal voltage
X_A	Total reactance of antenna
X_C	Capacitive reactance
X_L	Inductive reactance
Z_A	Input impedance of antenna
Z_{NA}	Normalized input impedance of antenna
Z_{TL}	Characteristic impedance of the transmission line
Γ	Voltage reflection coefficient
ε_r	Relative permittivity
η_r	Radiation efficiency
θ	Angle in the *z*-*x* plane
λ	Wavelength
σ	Conductivity
φ	Angle in the *x*-*y* plane

CHAPTER 1

1. Introduction

Miniaturization is perhaps *the* defining trend in the design and manufacture of modern electronics. Spurred by the demand for ever higher productivity and mobility, the constituent parts of modern electronic devices are encouraged to take an ever-smaller form factor. Central processing units have traditionally received the most attention towards this aim, governed loosely by the well-known Moore's Law [1-4], though the philosophy has since been extended to entire systems [5]. Historically, process resolutions (fabrication) and heat dispersal have been the primary hurdles; the trend is so mature that limits on miniaturization are now believed to be set by quantum tunnelling effects present at the molecular level [6, 7]. Batteries and power sources have similarly improved leaps and bounds to keep up pace [8-10].

For electronics relying on wireless connectivity, small antennas are vitally important. In some cases, the antenna even determines the absolute limits on system performance [5, 11]; the miniaturization of these antennas in a similar vein to other electronics components is responsible for the continued development and deployment of ever more sophisticated wireless communications systems and the modern 'information' economy. The original debate over wired versus wireless networks in terms of safety, range, set-up and operational costs, and so forth is as valid as ever. However, the boom in personal computing and communication devices, together with the rise in popularity of 'smart' gadgets – all linked together with the Internet of Things (IoT) – has led to a paradigm shift in the preference of wireless communications over wired [12], due in part to the desire for connectivity at all times and places. Indeed, in many applications, real estate is a prime commodity and wireless networks

employing small antennas are the only viable option; examples include personal communication gadgets (for the sake of portability), healthcare monitoring equipment (for the safety and comfort of the patient), and even military equipment (for ease of concealment). Novel security measures for wireless communications – such as directional modulation [13, 14] – address a relative disadvantage of wireless communications, helping to ensure the continuation of this trend.

Pioneered by Hertz in 1888 and popularized by Marconi in 1901 [15, 16], an antenna is a device which interfaces free space electromagnetic (EM) radiation, specifically radio waves, with guided waves (waveguides) or electrical energy (circuits), and vice versa. In essence, these are conductive structures engineered to 'resonate' at a particular frequency of operation; their physical dimensions are consequently determined primarily by the wavelength at this operational frequency, related by a physical constant – the speed of light in the medium of operation (often free space). To take only a few examples and typical frequencies, the global positioning system (GPS) operates at a typical frequency of 1.5 GHz, 3G and 4G mobile phone systems at 800 MHz, and Wi-Fi and Bluetooth at 2.4 GHz; wavelengths (in free space) at these frequencies are approximately 20 cm, 38 cm, and 13 cm, respectively. For comparison, a typical 'smart' watch has a maximum dimension of 4 cm [17]. Thus, many practical small antennas used in mobile (especially handheld) wireless devices are classed as electrically small – that is, operating at wavelengths several times larger than their physical size.

Research in the field of electrically small antennas (ESA) is centred around the same aims which govern the miniaturization of electronics in general: improved performance for a fixed area/volume, and preventing performance degradation as the volume is shrunk. Consequently, ESAs are most often discussed in terms of their fundamental performance limitations; the field was popularized by a seminal paper authored by Harold Wheeler in 1947 titled 'Fundamental Limitations of Small Antennas' [18]. These limitations, expanded later in this Thesis, are low efficiency, narrow bandwidth, and a poor impedance match to the rest of the radiofrequency (RF) front-end [11, 19-22]. As explained later,

novel three-dimensional (3D) antenna designs may be employed to overcome some of these limitations [11, 19-22]; structures hitherto too complex to fabricate with traditional processes may soon be realized with emergent technologies such as holographic photolithography and three dimensional (3D) printing [23-25].

1.1. Thesis Structure

This Thesis documents research conducted by the author towards practical antenna design, encompassing modifications to the antenna's structure to optimize performance, as well as an investigation of novel manufacturing techniques.

Chapter 1 – **Introduction** – covers the formal definitions of ESAs, and the theoretical and practical limitations on the design of ESAs. This is followed by a literature review of popular and recent antenna designs, grouped by various miniaturization techniques. The chapter concludes with a review of the aims and motivations of this research.

Chapter 2 – **Theoretical Background for Electrically Small Antennas** – covers the various performance metrics used throughout the document to analyse antennas, as well as the measurement techniques and setups used. The second part of the chapter provides an overview of manufacturing processes for antennas, from the traditional photolithography to the emergent 3D printing.

Chapter 3 – **Miniaturization using Centrally Populated Digitated Structure** – covers the design and analysis of two novel ESAs: single resonance inverted-F antenna (IFA), and dual resonance planar inverted-F antenna (PIFA). Simulation and measurement results are provided to illustrate the effects of miniaturization on the antenna's performance; practical considerations for the accurate measurement of radiation efficiency are highlighted.

Chapter 4 – **Detailed Analysis of Centrally Populated Digitated Structure** – provides an in-depth analysis of the novel contribution leading to miniaturized

antennas. An abstraction of the centrally populated digitated structure is introduced for the sake of simplicity, and an extensive parameter study provided to aid rapid design tuning of the digitated IFA. Finally, antenna performance is compared to some recent antennas discussed in the literature review.

Chapter 5 – **Investigation of Fabrication Techniques** – covers three antenna types fabricated in-house as part of a concurrent investigation of fabrication techniques. Pioneering measured results for 3D printed metallic antennas are provided; the advantages and limitations of this emergent fabrication technique in the context of antenna fabrication are also discussed.

Chapter 6 – **Conclusions** – concludes this Thesis. Limitations of the work undertaken are highlighted, and recommendations are made for the refinement of current results, as well as the exploration of related lines of research.

The appendix – **Computer Generated Holograms** – provides a summary of the work undertaken during the early stages of this project towards the realization of holographic photolithography.

1.2. Definition of Small Antennas

In order to distinguish between the physical and electrical size of an antenna, its dimensions are expressed in terms of the operating wavelength (or frequency); generally, the largest dimension of an ESA is a small fraction (typically a tenth) of its operating wavelength. A precise definition is not available in the IEEE Standard for Definitions of Terms for Antennas [26], and thus there are more than one practical definitions considered by the antenna research community. A widely accepted definition for as ESA is one whose maximum dimension is less than or equal to $\lambda/2\pi$, referred to as a *radianlength* (where λ is the symbol for wavelength) [19, 20]. Antenna geometries abiding by this demarcation radiate the first order spherical modes of a small Hertzian dipole [20] – an infinitesimal theoretical construct which provides the basis for the analysis of more complicated antenna geometries. Throughout this Thesis, a popular equivalent formulation is used:

$$ka \leq 0.5$$

Equation 1-1

where k is the wavenumber (equal to $2\pi/\lambda$), and a is the radius of an imaginary sphere circumscribing the maximum dimension of the antenna, also referred to as the *Chu sphere* in acknowledgement of the seminal work on the fundamental limitations of ESAs carried out by Chu in 1948 [27]. This is illustrated in Figure 1-1. If the antenna is mounted on a very large ground plane, then by default the *Chu sphere* will incorporate the 'image' of the antenna within the ground plane; the actual dimension of the ground plane need not be incorporated into the parameter a. However, it becomes necessary to include the entire structure in consideration for a if the ground plane is comparatively sized to the antenna, or is deliberately designed to affect the antenna's performance (e.g. defected ground structures).

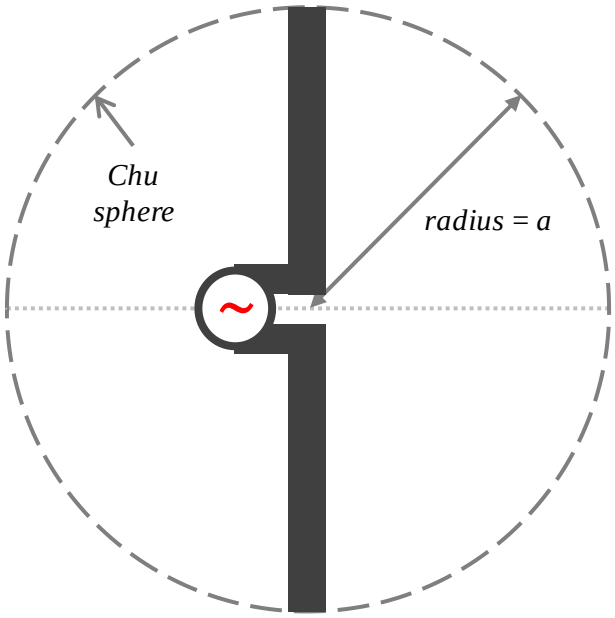

Figure 1-1. 2D illustration of the *Chu sphere*, with radius a, circumscribing the maximum dimension of a generic antenna structure. For ka = 0.5, the enclosed volume equals $\lambda^3/48\pi^2$.

Another commonly used definition for ESAs is $ka \leq 1$, so that the radius and not the diameter of the antenna equals one radianlength. Such an antenna would

be enclosed in a *radiansphere*, which represents the boundary between the *near-* and *far-field* radiation for a small Hertzian dipole [20, 28].

As such, a physically small antenna of maximum dimension 5 cm (i.e. a = 2.5 cm) would be considered electrically small if operating at 1 GHz (ka = 0.5), but not if operating at 3 GHz (ka = 1.6). In general, the performance of an antenna will suffer as it is forced to operate in the region where it would be considered electrically small.

1.3. Fundamental Limitations of Electrically Small Antennas

As the electrical size of an antenna is reduced, its radiation pattern tends towards that of a Hertzian (very small) dipole [19, 20], and is therefore not a property that can be engineered towards specifications. Note that the radiation pattern of a Hertzian dipole is similar to that of the half-wave dipole shown in Figure 2-2 (with maximum directivity ≈ 1.8 dBi* instead of 2.1 dBi). In fact, most applications requiring ESAs often tend to demand omni-directional patterns; handheld and body-mounted devices, for instance, may be positioned in any number of orientations during use. Additionally, many modern wireless devices are employed in environments polluted with scattered and multipath fields, resulting in received signals arriving from multiple directions and with varying polarizations. The polarization mismatch factor, P (≤1), is thus often ignored in the analysis of ESAs. Due to this limitation on directivity, and the non-consideration of polarization mismatch, a good impedance match and high radiation efficiency are the main influences on antenna gain which can be engineered towards a specific target. These are often combined into a single metric called the Q_{ratio}, described here.

The quality factor, Q, of an antenna can be related to its impedance match and fractional bandwidth (FBW):

* dBi is decibels over isotropic (see Chapter 2).

$$Q_{antenna} = \frac{(VSWR_{-3dB} - 1)}{FBW_{-3dB}\sqrt{VSWR_{-3dB}}}$$

Equation 1-2

This relationship is explained in greater detail in Chapter 2, with Equation 1-2 repeated as Equation 2-26. Considerable work has been carried out on the theoretical performance limitations of ESAs, resulting in the formulation of key limits on the lower bound of Q, termed Q_{lb}. These limits can be formulated in terms of the electrical size and radiation efficiency of the antenna, as presented in Equation 1-3. A specialized figure of merit, namely the Q_{ratio} (which is simply the ratio of the Q of an antenna over its theoretical lower bound), is therefore a useful way of quantifying the performance of any ESA. It also allows for an easier comparison across various ESA topologies and designs.

The earliest work on fundamental limitations of ESAs was conducted by Wheeler in 1947 [18], refined subsequently by Chu [27] and McLean [29], amongst others [30-33]; see [20] for a summary of major contributions to this line of research. For linearly polarized, single-mode antennas, the following expression for the lower bound on Q (the Chu limit) is commonly used [19]:

$$Q_{lb-Chu} = \eta_r \left(\frac{1}{(ka)^3} + \frac{1}{ka} \right)$$

Equation 1-3

where η_r is the radiation efficiency of the antenna (see Chapter 2).

The lower bound for Q is plotted in Figure 1-2 for three different values of radiation resistance. The corresponding limit for a circularly polarized antenna is approximately half of this limit [20]. The main implication is that there are fundamental upper limits on the radiation efficiency and/or bandwidth for a given size of antenna; moreover, as the electrical size of the antenna is reduced, the quality factor tends to increase. Considering again the imaginary Chu sphere illustrated in Figure 1-1, work by Wheeler and others has also indicated that for the same maximum dimension, an antenna fully utilizing the available volume

has the lowest Q compared to any other geometries within the same volume [11, 19, 20]. In other words, the 'best' compromise between the occupied volume, bandwidth, and efficiency is realized when most of the available volume is utilized for the radiating structure. Much of the work mentioned focuses on establishing an upper limit on the bandwidth (so that the bandwidth is expressed as a function of the lower bound on Q), as ESAs typically exhibit very narrow fractional bandwidths, down to a few percent [19]. Considered in isolation, high radiation efficiencies ($\eta_r \geq 90\%$ [19]) are possible with the use of highly efficient conductors and a very good impedance match at resonance, though the resulting bandwidth is inevitably narrow.

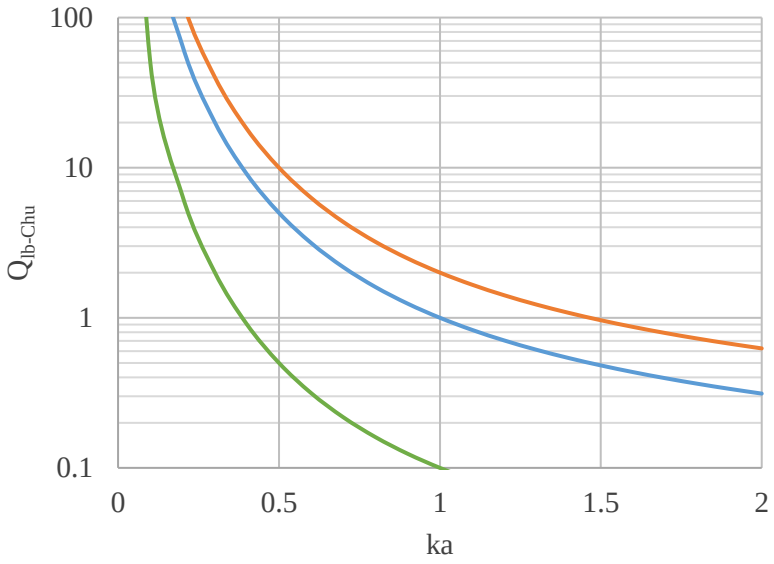

Figure 1-2. Lower bound on Q plotted for three different values of radiation efficiency, (orange) 100%, (blue) 50%, (green) 5%.

From Equation 1-2 and Equation 1-3, an expression for Q_{ratio} can be derived:

$$Q_{ratio} = \frac{Q_{antenna}}{Q_{lb-Chu}} = \frac{(VSWR_{-3dB} - 1)(ka)^3}{\left(FBW_{-3dB}\sqrt{VSWR_{-3dB}}\right)(1 + (ka)^2)(\eta_r)}$$

Equation 1-4

Large parts of Chapter 3 and the entirety of Chapter 4 deal with linearly polarized ESAs, with a single impedance resonance within the antenna's fractional bandwidth. Under these conditions, the expression for Q_{ratio} given in

Equation 1-4 is valid and therefore included in the discussion. However, parts of Chapter 3 and Chapter 5 deal with ESAs where the intent is to tune two resonances close together such that they fall within a single fractional bandwidth (as a means of further increasing bandwidth). There is still no consensus as to what fundamental limits apply to such antennas [19, 34], and therefore the parameter Q_{ratio} is not used in the discussion of such antennas.

1.3.1. Practical Design Considerations

It can be observed from Equation 1-2 that the Q of an antenna is inversely related to its fractional bandwidth, and from Equation 1-3 that the degree of miniaturization (note that this is the inverse of ka) is inversely related to the antenna's radiation efficiency, through a lower bound for Q. It is also understood from Equation 1-5 (note: repeated as Equation 2-22 in Chapter 2 where radiation efficiency is formally defined) that a high radiation resistance, R_{rad}, leads to a higher radiation efficiency.

$$\eta_r = \frac{P_{rad}}{P_{in}} = \frac{P_{rad}}{P_{rad} + P_{loss}} = \frac{R_{rad}}{R_{rad} + R_{loss}} = \frac{R_{rad}}{R_A}$$

Equation 1-5

Therefore, it is important not only to match the resistive component of an antenna, R_A, to 50 Ω (in a typical 50 Ω system), but also to ensure that R_{rad} and not R_{loss} (loss resistance) is the main contributor to R_A. This is particularly challenging since electrically small antennas tend to have a low radiation resistance, with a large reactive component of impedance [19].

From this discussion, it is clear that miniaturization is at odds with performance. Bandwidth and radiation efficiency are the two key properties which may be improved (within fundamental limitations), though there is often a trade-off between miniaturization and performance depending on the application at hand. For instance, it is a known practice to purposefully mismatch an ESA to obtain marginal improvements in its bandwidth [19], a practice not immediately obvious from the metric Q_{ratio}. Narrower bandwidth antennas are more susceptible to frequency detuning from nearby objects (due to narrow

bandwidths, a slight shift in the resonance frequency from the actual operational frequency could significantly increase the mismatch factor).

Taking a broader view still, material considerations and even ease of manufacture all play a big part in the final structure and make up of an antenna. Cell phone antennas, for example, have transitioned from monopole whip antennas encased in radomes and strategically placed away from the main phone circuitry to complex configurations often printed on the same printed circuit board (PCB) as the rest of the electronic circuitry. It would not be a wild claim to make that material losses due to the dielectric of the PCB are unavoidable for practical modern antennas. Despite the knowledge that utilizing the full available volume (theoretically) generally improves antenna performance [11, 19, 20], it might not be practical to design such an antenna where the real estate is simply not available for voluminous structures. There are questions over whether standard manufacturing techniques can be suitably adapted to the manufacture of such antenna structures. Solutions may be found via the use of novel fabrication techniques, such as 3D printing, though it is yet unclear if such processes can deliver to the tolerance levels expected by antenna designers all the way through to the end-user.

1.4. Literature Review

This section provides a non-exhaustive list of common miniaturization techniques for the design of ESAs, grouped by the type of materials, structures, and/or components required. Often, two or more of these techniques are combined for the design of practical ESAs. This is highlighted in an overview of recently reported ESAs, and a case study on the evolution of the IFA from a wire monopole. For a more extensive survey of influential ESAs, refer to [11], [20], and [35].

1.4.1. Common Miniaturization Techniques

Miniaturizing may be viewed from two perspectives, which are often combined for practical antenna design. The first is to simply lower the resonance

frequency for an antenna of given dimensions (i.e. same physical size). Often, care is taken to minimize the deterioration in the performance of the antenna as its electrical size is reduced. Another approach is to improve the performance of an antenna for a given electrical size, in terms of its impedance match, radiation efficiency, and fractional bandwidth. (It should be noted that the electrical size is defined by the largest dimension and its circumscribing sphere; however, expansion into the 3rd dimension is not always a practical option.)

As explained later in Chapter 2, a well matched resonant antenna has no reactive component in its feed point impedance, with the resistive component matched to that of the feed line (cable). Note that it is still possible to impedance match antennas where the condition of zero net reactance is not satisfied through the antenna geometry itself, with the use of a capacitor or inductor, as required, to tune the perceived feed point reactance to zero [19, 20]. These passive components may be integrated into the geometry of the antenna itself (for instance chip capacitors may be directly soldered onto tracks on a PCB), or used to create an external two-port (i.e. one input, one output) matching network. Such reactive components may theoretically be used to tune any antenna to resonance at a desired operational frequency, thereby resulting in an electrically small radiator. Practical usage of this technique, however, is limited by the range of frequencies over which matching is required, and the degree to which additional losses are introduced by the matching components [11, 19, 20]. That is, any gains made by an improved mismatch factor may well be negated by the extra losses incurred due to these matching components. The complexity of fabrication is also increased leading to slower throughput and increased costs.

Wideband matching is possible with the use of negative impedance converters (NIC) [11, 20, 36]. These are two-port networks comprised of a combination of active devices (diodes) with the usual passive reactive components, and designed to cancel out the reactive part of an antenna's impedance over a wide band of frequencies. A biasing DC voltage is required for the active components, thereby increasing the energy drain. Moreover, such an external matching network would need to be considered as part of the antenna structure, effectively raising the *ka* value of the antenna to be miniaturized.

An alternative technique to achieve the same tuning effect is the clever use of geometry, shaping the antenna structure such that equivalent inductance or capacitance is added to its feed point impedance. One approach to reducing the resonance frequency is simply to increase the total length of wire or printed metal tracks, or equivalently, increasing the path of current flow (e.g. with the use of slots and notches on a planar antenna) [11, 19, 20]. In particular, to increase self-inductance, structures such as meanderlines and helical coils may be employed [11, 19, 20]. Another way to increase self-inductance is the use of a parallel stub (as in an inverted-F antenna) near the feed point of the antenna [19, 20]. A top hat (as in the case of top loaded monopoles) may be used to increase the self-capacitance [11, 19, 20]. On planar topologies, this may be accomplished with a bend in the main radiating arm, as is the case with an inverted-L antenna (ILA). Such modifications to geometry can be viewed as a 'better' use of the available space or volume.

The same approach can be extended to the use of fractal geometries [37], and further abstracted to the use of optimization algorithms (such as the genetic algorithm [38]) to extract the best possible performance from a given shape or volume through any possible geometrical configuration [11, 19, 20]. A bowtie antenna is a modification on a simple dipole which results in an improvement in bandwidth; a less constrained current path can support more radiating modes [11, 20]. Similarly, two resonances forced close together, such that they share the same half-power fractional bandwidth, FBW_{-3dB} (see Chapter 2), act to practically improve the antenna's bandwidth [19].

Material loading is another technique to reduce the resonance frequency of an antenna for a given dimension [11, 19, 20], as seen with dielectric resonator antennas (DRA). For instance, the antenna may be encased in a high permittivity and/or permeability dielectric, resulting in a slower phase velocity for the current and increasing the electrical length. Once again, there is a trade-off between miniaturization and increased dielectric losses.

Yet another miniaturization technique is based on the exploitation of metamaterials – structures or materials designed with unusual physical

properties. For instance, high impedance surfaces (HIS) can be incorporated into the antenna's ground plane to smooth out the forward radiation pattern (by suppressing currents on the edge of a ground plane), or reduce the profile of antennas mounted horizontally and in close proximity to a ground plane (by reinforcing the currents on the antenna rather than cancelling them out) [39]. Recent advances in the miniaturization of metamaterial structures [40, 41] (typical periodicity reduced from ~ $\lambda/10$ to $\lambda/50$) using lumped components can potentially lead to further reduced profile of ESAs mounted over HIS, albeit at the cost of reduced efficiency. Metamaterial-inspired antennas [42-44] make use of the resonance behaviour of the unit cells which comprise metamaterials. One to a few unit cells are placed in close proximity to an antenna such that coupling fields excite the unit cells at their designed resonance frequency. This frequency may be much lower than that of the antenna by itself, thereby effectively realizing a miniaturized antenna structure [11, 20]. Similar structures may also be incorporated as slots in planar antennas to accomplish radiation at a lower frequency to that of the antenna by itself.

1.4.2. Recent Developments

This section provides an overview of recent (since 2000) developments in ESA design; effort is made to present a wide array of design philosophies and miniaturization techniques. Selected references are given, with a brief summary of the design principle and reported performance. None of the antennas discussed here violate the physical limits on performance set by the lower bound on *Q*. Where possible, the figures of merit *ka* and radiation efficiency, at resonance, are reported; otherwise, the dimensions of the antenna are presented in terms of the operating wavelength. Bandwidth is omitted, as there are several possible definitions (see Chapter 2 for more on these metrics); instead, the Q_{ratio} (either reported, or calculated from the information provided in order to be consistent with the definition used in Equation 1-4) is highlighted. A brief review of antennas manufactured with novel fabrication techniques is also provided towards the end of this section.

A scatter plot of the Q_{ratio} versus *ka* for selected antennas is presented in Figure 1-3 with individual markers annotated with the reference number in square brackets. The markers are grouped by references where measurements were fully characterized, and others where simulations and measurements were combined in reporting the various performance metrics.

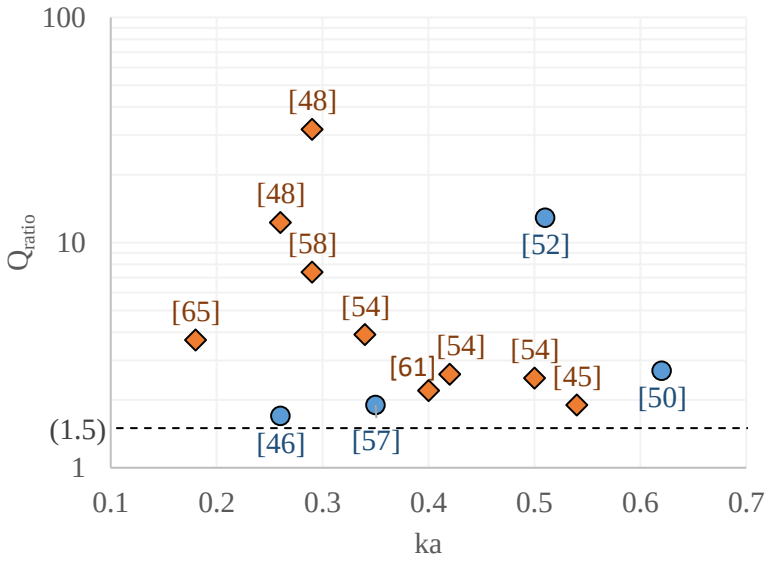

Figure 1-3. Q_{ratio} vs *ka* value scatter plot for selected antennas from literature review; (orange-diamond) antennas with measured radiation efficiency either reported or extractable from data provided, (blue-circle) antennas with simulated radiation efficiency provided. Note that for a linearly polarized ESA, the limit for Q_{ratio} is 1.5.

In 2007, Stuart and Tran [45] reported a multi-arm spherical ESA and demonstrated fabrication using planar printed elements mechanically joined together; a coplanar strip feed line populated with chip capacitors was used to match the impedance of the radiator to 50 Ω. A single resonance version of the antenna has a *ka* value of 0.54, radiation efficiency 94%, and a corresponding Q_{ratio} of 1.9. Bandwidth enhancement is demonstrated by increasing the number of arms, resulting in two closely spaced resonances. In 2010, Best and Hanna [46] compiled the theoretical properties of various wire-grid voluminous antennas. In particular, a spherical capped (top loaded for increased self-capacitance) dipole, with a helical (for increased self-inductance) vertical element was shown to have a *ka* value of 0.26, (simulated) radiation efficiency of 93%, and a corresponding Q_{ratio} of 1.7.

In 2004, Anguera *et al.* [47] reported a microstrip patch antenna ($a \approx 28$ mm) miniaturized with the use of slots in the radiating patch to influence the self-inductance and self-capacitance of the antenna. They report a reduction in *ka* from 1.20 to 0.70, with respective Q_{ratio} of 48.9 and 166.7. Over this range, the reported (simulated) radiation efficiency drops from 86% to 23%. Finally, a parasitic patch is suggested as a means to excite two closely-spaced resonances, improving the bandwidth and the directivity of the antenna. In 2007, Feldner *et al.* [48] reported on the miniaturization of a PIFA ($a \approx 30$ mm; excluding 1.5 m^2 ground plane), accomplished with capacitive loading and switchable (using transistors) shorting pins. The tuneable antenna is demonstrated to cover *ka* from 0.26 to 0.29, with respective Q_{ratio} of 12.3 and 31.8 at these extremes. The efficiency is reported as 5.5% over the corresponding frequency range (note that radiation efficiency varies depending on how many switches are in the "on" state and contributing to insertion loss). A key attraction of this structure is that the PIFA is designed as housing for the battery and required switching network. The same year, Wong, Chang, and Lin [49] demonstrated improved shielding for PIFAs mounted on mobile phone PCBs with the use of shielding strips at the ends of the antenna to suppress fringing fields.

In 2006, Waterhouse and Novak [50] reported a slot antenna ($a \approx 69$ mm), miniaturized with the use of a meandered slot, impedance matched to 50 Ω using a co-planar waveguide (CPW) feed [51]. The antenna has a *ka* value of 0.62, reported efficiency of 75%, and a corresponding Q_{ratio} of 2.7. The antenna is designed to be uni-planar (all tracks on a single face of the substrate), and thus well-suited to existing fabrication techniques. In 2008, Hong and Sarabandi [52] reported a cavity-backed composite slot loop antenna ($a \approx 52$ mm), which makes use of meandering tracks and an integrated feed network to miniaturize a standard loop and improve its impedance match. At its operating frequency, the antenna has a *ka* of 0.51, (computed) radiation efficiency of 49%, and Q_{ratio} of 12.9. The authors also demonstrate that halving the height of the antenna, with the rest of its dimensions unchanged, has the effect of dropping the radiation efficiency to 30%, with a respective Q_{ratio} of 26.6. In 2005, Latif, Shafai, and Sharma [53] demonstrated the use of self-complementary slot

structures to excite multiple modes and enhance the bandwidth of miniaturized slot antennas.

In 2005, Hosung *et al.* [54] utilized a genetic algorithm to generate high efficiency, arbitrarily-shaped wire antennas. They report measurements on three designs (aimed resonance frequency of 400 MHz), with *ka* values of 0.34, 0.42, and 0.50. The respective radiation efficiency values are 84%, 92%, and 94%, with the corresponding Q_{ratio} of 3.9, 2.6, and 2.5. All antennas are inherently 3D, with no dielectric materials; hence the high values of efficiency. The extremely low values of Q_{ratio} are testament to the utility of optimization techniques in ESA design, though these come at the cost of a lack of intuitive understanding of the antenna's behaviour. Further miniaturization at the expense of bandwidth and efficiency was demonstrated in [55], where computationally optimized antennas are immersed in a high permittivity dielectric powder. In 2004, Altshuler [56] demonstrated the improvement in matching for computationally optimized antennas with the placement of an inductive matching post near the feed point, principally similar to their application in IFAs.

In 2006, Rodenbeck [57] demonstrated an ESA designed to be integrated on the reverse of a PCB housing control electronics and batteries. The antenna comprises a meanderline section fed with a capacitive strip for improved impedance matching. The *ka* value at resonance is 0.35, reported (calculated) efficiency 40%, and the corresponding Q_{ratio} 1.9. Measurements taken without the batteries provide similar results, thereby proving the antenna's performance is insensitive to the presence of the batteries. In 2014, Deepak *et al.* [58] reported a compact printed antenna using a chip inductor to miniaturize the radiator, and a CPW feed for impedance matching. The antenna has a *ka* value of 0.29 at resonance, with efficiency reported at 70%, and a corresponding Q_{ratio} of 7.4.

In 2010, Ghosh *et al.* [59] reported an easy-to-fabricate wire dipole ($a \approx 16$ mm), loaded with loops (increasing the self-inductance) to reduce its electrical size. The antenna has a *ka* value of 1.04 at resonance, radiation efficiency 97%, and a corresponding Q_{ratio} of 2.7. The unloaded version of the same antenna has a

ka value of 1.40 and Q_{ratio} of 6.1. A counterpart loaded monopole has a *ka* value of 1.07 and a Q_{ratio} of 1.7 (due to improved bandwidth over the dipole). This simple technique is shown to provide considerable reduction in electrical size; however, the very low figures for Q_{ratio} correspond to antennas slightly over the widely accepted *ka* limit for an ESA.

In 2013, Tang and Ziolkowski [60] reported on a metamaterial-inspired antenna ($a \approx 40$ mm), based on the design guidelines introduced in [42, 43]. The antenna consists of a ground plane integrated with complementary split ring resonators, excited by a perpendicularly placed, miniaturized (with the use of a top hat) monopole. The authors highlighted the need for a sleeve balun (length approximately 70 mm) to minimize the impact of the leakage currents on the coaxial cable during measurements. The antenna (excluding balun) has a *ka* value of 0.86, (simulated) radiation efficiency of 98%, and a corresponding Q_{ratio} of 49. Theoretical Q_{ratio} as low as 5.2 (for *ka* of 0.8) has been reported for similar antenna designs in [61]. Preliminary results by the same group show improvements in the bandwidth of similar metamaterial-inspired antennas with the use of an integrated NIC matching network [62], though efficiency values were not reported (still under investigation).

In 2010, Zhu *et al.* [63] reported a loaded split ring dipole antenna ($a \approx 43$ mm) placed over the miniaturized HIS surface of [40, 41], with a combined antenna/metamaterial thickness at resonane of $\lambda/44$. Further modifications on this design were reported in [64], making the antenna tuneable with the use of varactor diodes. The tunable antenna is demonstrated to cover *ka* of 0.33 to 0.45, with a corresponding Q_{ratio} at the upper end of operational frequency of 3.9, and radiation efficiency 24% (measured radiation efficiency not reported at lower end of operating frequency).

In 2010, Kim [65] reported a 3D spherical antenna ($a \approx 40$ mm) where split rings are coupled to a centrally excited radiating element; the design approach is to establish a uniform current distribution over the surface of the sphere. At resonance, the antenna has a *ka* value of 0.18, with a radiation efficiency of 73%, and a Q_{ratio} of 3.7. A planar variant using a similar design approach [66]

reported a Q_{ratio} of 7.5, for a *ka* of 1.3 and radiation efficiency 23%. In 2016, Madsen, Zhou, and Sievenpiper [67] presented a simplified variant of the 3D spherical antenna for ease of manufacture, also exhibiting dual resonances for bandwidth enhancement.

In 2002, Lee *et al.* [68] reported on the miniaturization of a dielectric (relative permittivity, ε_r = 10) resonator antenna with a top hat. Excluding the ground plane, the electrical size of the radiator is reduced from 0.19λ to 0.15λ at the expense of bandwidth. A patch antenna loaded with a dielectric (ε_r = 10) resonator was reported in [69] as having a *ka* value of 0.62; bandwidth enhancements through an increase in the height of the antenna are proposed in [70].

The various contributions highlighted so far feature either antennas that have been designed for fabrication using traditional methods, or complex antennas where the primary aim has been to push the boundaries on performance versus miniaturization, with fabrication as an afterthought. As a specific example, the antenna described in [67] is an approximation of the spherical antenna described in [65] for ease of fabrication; still, the authors of [67] comment on how the accuracy of their approximation was constrained by fabrication considerations. In light of such limitations (primarily the patterning and metallization of non-planar substrates), there has been an upturn recently in the attention given to non-traditional fabrication techniques for the manufacture of inherently 3D antenna designs, such that the geometry of the antenna is not limited by fabrication.

In 2010, Anagnostou *et al.* [71] reported a flexible IFA ($a \approx 28$ mm), realized by direct-write printing of metal tracks onto a paper substrate. The antenna has a *ka* value of 1.4 at resonance, with a reported efficiency of 82%. A key benefit of this fabrication technique is the ability to manufacture flexible antennas, which can be used in wearable electronics, for example. The direct-write process is well-suited to rapid prototyping, but is not ideal for mass fabrication due to the serial, time-consuming nature of the process. In 2011, Adams *et al.* [72] reported electrically small, multi-arm conformal meandered antennas, with

values of Q_{ratio} ranging from 1.5 to 2.5 (*ka* values for all antennas below 0.5) and maximum reported efficiency of 71%. The radiating structure was printed onto a glass hemisphere using conductive ink in a direct-write process. In 2013, Toriz-Garcia *et al.* [73] reported a similar structure (Q_{ratio} reported as 2.15; measured radiation efficiency 46%), fabricated using holographic photolithography, resulting in a faster fabrication process for mass manufacture. It should be noted that due to the hemi-spherical geometry of this antenna (low light intensities at the equator), the authors found it necessary to rotate the substrate for each of the eight total meanderline tracks to be defined. Thus, whilst the modified photolithographic process is much faster than the serial write process used in [72], there is still a serial element to fabrication. Both techniques are limited to 'thin' metal tracks, which in turn limits practical application to only a subset of antenna types.

In 2012, Pfeiffer *et al.* [74] used direct transfer patterning to fabricate a multi-arm helical antenna ($a \approx 20$ mm) onto a hemispherical substrate, using a polymer stamp. The antenna has *ka* value of 0.23, radiation efficiency of 52%, and a corresponding Q_{ratio} of 2.1. The process, as with direct-write and holographic lithography, is suited to narrow metal tracks. The main disadvantage is that it is a contact process, subject to stamp wear, and is limited to simple conformal substrate geometries. In 2014, Kgwadi *et al.* [75] employed thermal transfer printing to fabricate a meanderline monopole antenna ($a \approx 38$ mm) on a flexible polyester substrate. The antenna has a *ka* value of 0.67 with low radiation efficiency, primarily attributed to losses in the novel substrate material; the authors further outline improvements to the antenna design which increases the measured gain of the antenna to be more in line with counterparts fabricated with the more common inkjet printed techniques. The fabrication method is advantageous over inkjet techniques in terms of its simplicity and speed, though it is limited by the range (and properties) of available compatible substrates, and is essentially a subtractive technology which leads to greater amounts of wasted raw material.

In 2013, Nassar and Weller [76] reported the use of additive manufacturing (AM) to fabricate a 3D cube antenna as a proof of concept. The substrate was

fabricated using stereolithography apparatus (SLA) [24], and subsequently patterned with conductive ink. In the same year, Kim [77] reported a multi-arm helical antenna ($a \approx 26$ mm), similar to the one presented in [74], where a plastic support structure was fabricated using AM and subsequently coated with several layers of copper paint. The antenna has a *ka* value of 0.40, radiation efficiency of 80%, and a corresponding Q_{ratio} of 2.2. Both examples illustrate the benefits of AM as a means of rapid prototyping and initial testing of complex antenna geometries. The metal coating process can be improved and automated by the nascent Aerosol Jet technology [78, 79], which is able to spray coat metals onto conformal substrates. Extending the use of AM to outright 'print' metallic structures is another alternative which can lead towards the potential adoption of the technology for mass manufacture as well as rapid prototyping.

1.4.3. Case Study: From Monopole to Inverted-F Antenna

This case study looks at the evolution of an IFA from a monopole (illustrated in Figure 1-4), as an early example of an ESA design which combines geometrical shaping techniques for miniaturization and matching.

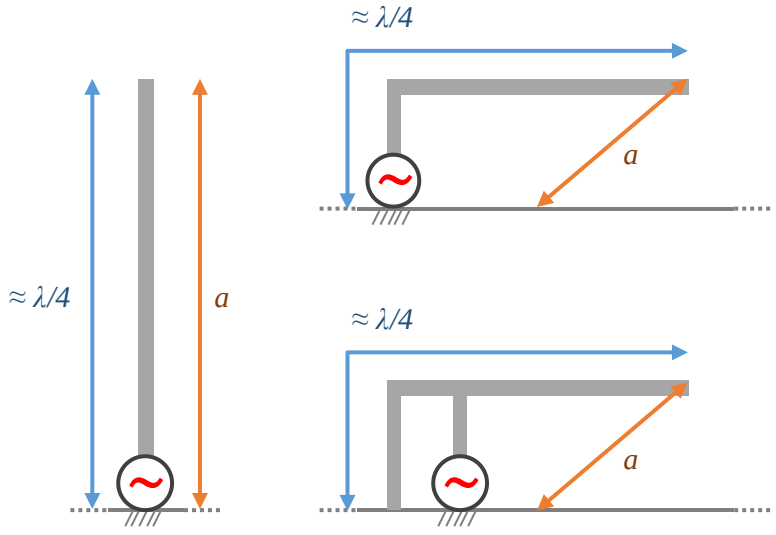

Figure 1-4. Illustration of three types of antennas: (*left*) wire monopole, (*top-right*) inverted-L antenna, and (*bottom-right*) inverted-F antenna.

A brief summary of the impedance properties of these antennas is provided here; full discourse can be found in many RF textbooks, such as [22]. The ILA is

realized simply by bending the monopole, with the resultant geometry resembling the letter 'L'. This serves to reduce the profile (height) of the antenna; moreover, the horizontal section acts to increase the capacitance to ground. The addition of the shorted shunt stub results in an IFA (named so because the resultant geometry resembles the letter 'F'); this stub acts to increase the inductance of the antenna (the exact value is determined primarily by the length and width of this stub). The resulting structure thus has increased self-capacitance and self-inductance, with the ability to tune these separately for optimization at a desired frequency. An added benefit of implementing a shunt stub (as shown) to increase the self-inductance is that the radiation resistance of the antenna structure is increased. The impedance can be tuned by the relative positioning of the feed with respect to the shorting pin. Note that the reduction in *ka* value is accompanied by a reduction in gain.

The S_{11} (see Chapter 2; measure of how well antenna is matched to feed – lower is better, minima gives frequency of resonance) results are provided in Figure 1-5. It can be seen that the IFA has a lower *ka* value than the monopole, and a better match to 50 Ω than the ILA. Metal tracks were modelled as infinitely thin, with a width of 1 mm and total length 25 mm (equal to λ/4 at 3 GHz). All configurations were modelled separately over a perfect electrical conductor (PEC) ground plane several times the operating wavelength. Note that in computing the *ka* value of the monopole, the parameter *a* equals 25.0 mm. However, for the ILA and IFA, *a* is halved to 12.5 mm, with the chosen configuration. (Note that for an antenna above a large ground plane, the parameter *a* is determined with the inclusion of the 'image' of the antenna in the ground plane.)

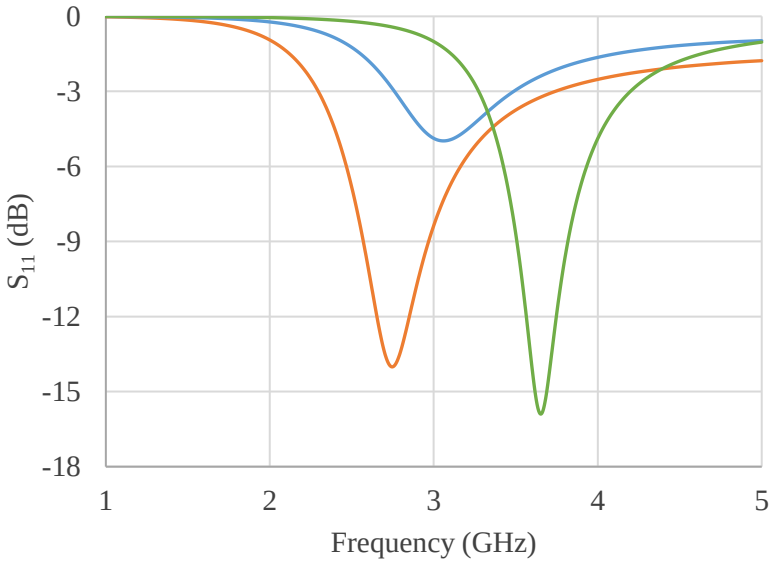

Figure 1-5. Simulated S_{11} for (orange) monopole, (blue) ILA, and (green) IFA. The repective resonance frequencies (and *ka* values) are 2.75 GHz (1.4), 3.00 GHz (0.78), and 3.75 GHz (1.0).

1.4.4. Comments

Various miniaturization techniques were covered in the literature review, and their application to modern antenna design demonstrated through a host of recently published ESAs. It is important to note that in the design of an antenna, the desired application (and in turn specific design parameters such as range, coverage, power consumption, etc.) determine which of these techniques are employed. For instance, lumped reactive components can be used to easily tune an antenna to resonance at frequencies lower than their corresponding physical dimensions would dictate; however, in certain applications, the added losses might be undesirable, even at the cost of a more complex design process. Tuneable antennas using active components exemplify novel solutions to the bandwidth limitations of ESAs, but the added complexity to fabrication is a potential hindrance to low cost and high-volume production. A small antenna that requires a large and complex feed network would in fact be as impractical as a larger design; in this instance, an antenna designer might be willing to sacrifice performance for a less-than-optimal matching network. Even a well-designed ESA might require imaginative metamaterials in order to keep a low overall profile and improved platform tolerance.

The case study provided an illustrative summary of the design and evolution of the IFA, which is one of the more common antenna types used in modern electronics due to its compact size and ease of tuning [22]. The following chapters provide a more in-depth study of geometrical manipulation techniques applied to such antennas to further lower their resonant frequency and provide greater control over their input impedance, whilst keeping the maximum occupied volume constant. Such an approach is favoured over others due to the simplicity of design, and consequently, fabrication. Limitations are addressed with the use of advanced, pioneering manufacturing methods – with the consistent aim of ease of fabrication.

The antenna designs presented in this Thesis were modelled and optimized using a specialist 3D EM simulation tool: CST Microwave Studio ® (CST MWS) [80]. Measurements were subsequently conducted to complement the simulated results, for which one or both of the time and frequency domain solvers were used. The time domain solver was typically used initially, with a hexahedral mesh, to efficiently (computationally) obtain the broadband frequency behaviour of the antenna under consideration. The frequency domain solver is typically more computationally intensive, and was employed subsequently, with a tetrahedral mesh, to obtain results over a narrow frequency range; this setup is especially apt for antennas possessing electrically small features and/or 3D features, according to the software's application notes. For both solvers, the mesh was sequentially refined to obtain results with a suitably low error threshold; results from both solvers and measurements were used to settle on a suitable compromise between accuracy and computational intensity.

1.5. Research Objectives

There were two main research objectives set out for this project.

The *first*, addressing antenna design, was twofold: (i) investigate and implement novel miniaturization techniques for planar antennas suited to traditional fabrication techniques, and (ii) investigate and implement techniques for improving the performance of the realized ESA.

A novel digitated structure was integrated into a compact, circular profile IFA, and is introduced in Chapter 3. The same principle is abstracted into a simpler design to provide a more intuitive understanding of the antenna's behaviour, presented in Chapter 4.

From the various techniques available for improving ESA performance, dual mode operation and voluminous expansion were investigated further; these are reported in Chapter 3 and Chapter 5, respectively.

Following on from this, the *second* objective was set to investigate suitable and viable fabrication techniques for the voluminous, 3D antenna variants.

Holographic photolithography was briefly considered, but additive manufacturing was ultimately chosen for prototyping and further investigation, with findings reported in Chapter 5.

A further, overarching objective set out for this project was the fabrication and measurement of any antenna designs put forth for discussion, so as to improve confidence beyond only simulated predictions.

CHAPTER 2

2. Theoretical Background for Electrically Small Antennas

This chapter starts with an overview of the performance metrics commonly used in the analysis of ESAs, and the measurement setup employed for each of them. The antenna quality factor is also introduced, to tie in with the commonly used Q_{ratio} metric discussed in Chapter 1. This is followed by an introduction to antenna fabrication techniques, with focus set on photolithography and additive manufacturing.

2.1. Antenna Performance Metrics

This section provides a primer on relevant ESA performance metrics, and provides a description of the measurement techniques and setups used for the data presented in this Thesis.

2.1.1. Radiation Pattern and Gain

The **radiation pattern** of an antenna is a spatial representation the EM field generated by the antenna, as characterized by quantities such as radiation intensity, directivity, realized gain, etc. [22, 26]. An antenna's radiation pattern may be represented either graphically or mathematically, and is typically described in the **far-field** (where the pattern shape is invariant over distance from antenna), along a spherical surface around its centre. Figure 2-1 and Figure 2-2 illustrate the directivity patterns of a typical patch antenna (directional pattern) and a half-wave dipole antenna (omni-directional pattern), respectively.

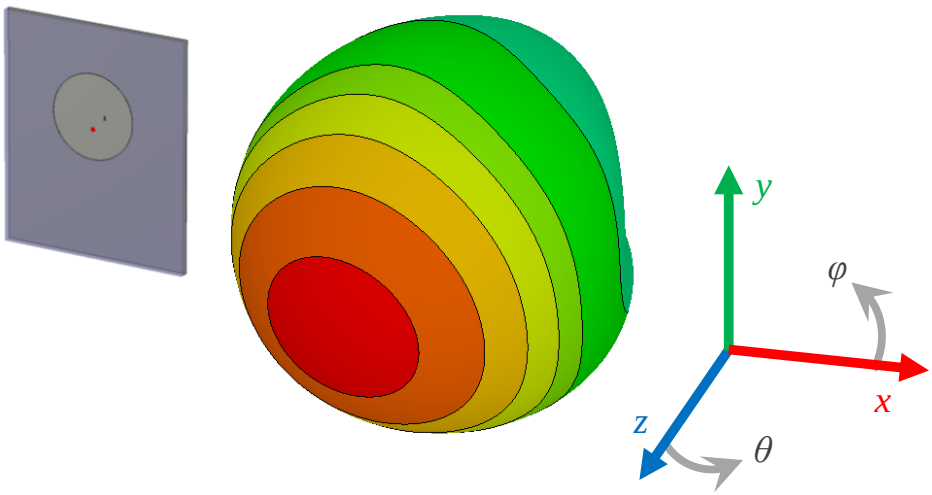

Figure 2-1. CST MWS model and simulated radiation pattern (3D, directivity) of a typical circular patch antenna, designed for resonance at 3 GHz (*ka* = 3.7). Color scheme: red (max) – green – blue (min); max. directivity ≈ 7.5 dBi.

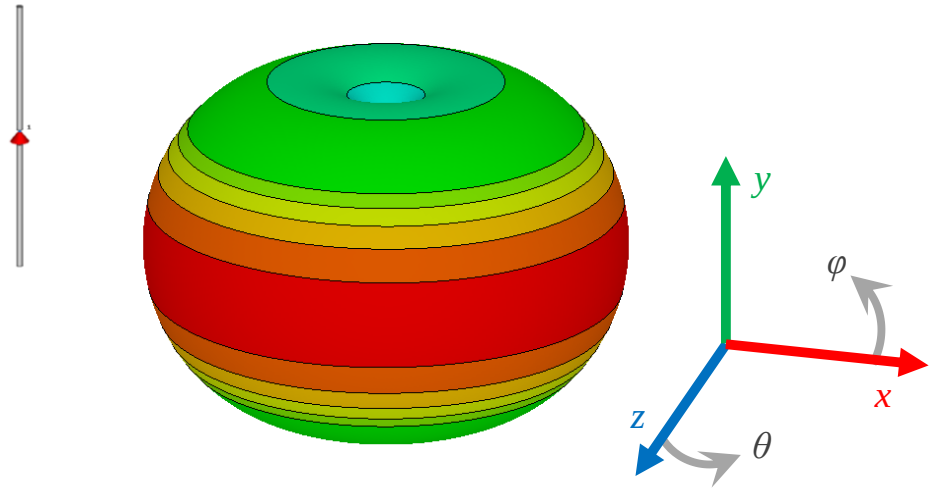

Figure 2-2. CST MWS model and simulated radiation pattern (3D, directivity) of a typical half-wave dipole antenna, designed for resonance at 3 GHz (*ka* = 1.4). Color scheme: red (max) – green – blue (min); max. directivity ≈ 2.1 dBi.

3D patterns like the ones shown in Figure 2-2 are often split up into two two-dimensional (2D) **principal plane patterns**. Typically, these are the *E*-plane (containing the electric field vector in the direction of maximum radiation) and *H*-plane (containing the magnetic field vector in the direction of maximum radiation) patterns. For the sake of convenience, the *E*-plane is further usually aligned with one of the geometrical principal planes: either *azimuthal* or

elevation [22]. Figure 2-3 shows the 2D principal plane patterns in decibels (dB) and linear scale for a half-wave dipole antenna with the *E*-plane aligned with the geometrical *x*-*y* plane (elevation), and the *H*-plane aligned with the geometrical *z*-*x* plane (azimuth). The decibel (dB) system is employed to accentuate finer details when there are large variances in a quantity; it is a logarithmic transformation of a linear scale, depending on whether the displayed quantity is a power or field (voltage) ratio:

$$value|_{dB} = \begin{cases} 10\log_{10}\left(value\,|_{linear,\ power}\right) \\ 20\log_{10}\left(value\,|_{linear,\ field}\right) \end{cases}$$

Equation 2-1

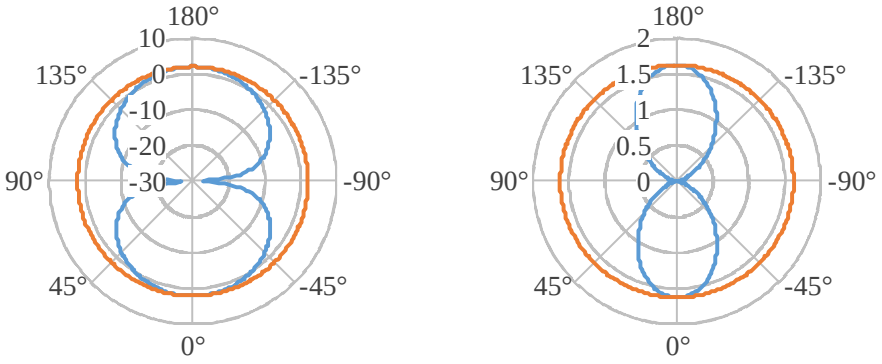

Figure 2-3. Simulated direcitvity in (*left*) decibels and (*right*) linear scale, for the half-wave dipole of Figure 2-2; (orange) azimuth plane, (blue) elevation plane; max. directivity ≈ 2.1 dBi or 1.6 (linear).

In reality, it is rare for the *E*-plane and *H*-plane to coincide perfectly with the principal geometrical planes. For the sake of consistency, all subsequent radiation patterns provided in this Thesis are presented as 2D patterns in the azimuth (*z*-*x*) and elevation (*x*-*y*) planes, with magnitudes given in the dB scale; local coordinates are displayed with each new geometry to aid the reader.

The **directivity**, *D*, (in a particular direction) of an antenna is defined as the radiation intensity of the antenna (in that direction) relative to the radiation

intensity of an isotropic† source (uniformly, in all directions) radiating the same power [22, 26]. In other words, it reveals whether or not the antenna favours radiation in certain directions over others, and to what extent. Usually quoted for the direction where radiation intensity is maximum, it can be expressed mathematically as [22]:

$$D_{max} = \frac{U_{max}}{U_0} = \frac{4\pi U_{max}}{P_{rad}}$$

Equation 2-2

where U_{max} is the maximum radiation intensity (units: W/steradian) of the antenna, and U_0 is the radiation intensity of an isotropic source radiating the same power. U_0 can be expressed in terms of the total power radiated, P_{rad}, as [22]:

$$U_0 = \frac{P_{rad}}{4\pi}$$

Equation 2-3

Another useful metric for characterizing the behaviour of an antenna is obtained by considering the antenna's conductional and dielectric losses. The **gain**, *G*, (in a particular direction) of an antenna is defined as the radiation intensity of the antenna (in that direction) relative to the radiation intensity of an isotropic source radiating with the same input (accepted) power [22, 26]. Also typically quoted for the direction where it is maximum, gain can be expressed mathematically as [22]:

$$G_{max} = \frac{U_{max}}{U_i} = \frac{4\pi U_{max}}{P_{in}}$$

Equation 2-4

† An isotropic source is an ideal point source that radiates energy uniformly in all directions [22,26]; as seen in the definition of directivity, it serves as a useful reference to practical, real antennas.

where U_i is the radiation intensity of an isotropic source radiating with the input (accepted) power, P_{in}. U_i can be expressed mathematically as:

$$U_i = \frac{P_{in}}{4\pi}$$

Equation 2-5

Thus, gain is similar to directivity, and takes into account the power accepted by the antenna rather than simply the power it radiates. Accordingly, the two can be related by a simple expression [22]:

$$G = \eta_r D$$

Equation 2-6

where η_r ($\leq$1) is termed the **radiation efficiency** of the antenna. If the losses due to impedance mismatch are included, a new metric called **realized gain** (G_r) is obtained. It may be expressed in terms of directivity and the impedance mismatch factor, M ($\leq$1), as [22, 26]:

$$G_r = \eta_r M D$$

Equation 2-7

Gain is typically presented in the dB scale; being a power ratio, the conversion from linear to dB (using Equation 2-1) is:

$$G_r|_{dB} = 10\log_{10}(G_r)$$

Equation 2-8

Since the ratio is defined with respect to an isotropic radiator (G = 0 dB, or 1), gain is often expressed as dBi (dB over isotropic).

In a system of antennas (i.e. at least one transmitting and one receiving), the **polarization** of the radiated EM field may be considered, depending on the application. The polarization of an antenna is essentially the orientation of the *E*-field vector which composes the radiated EM field. For maximum power transfer between two antennas, they should have the same polarization [22];

losses due to polarization mismatch can be reflected in the gain by adding the polarization mismatch factor, P ($\leq$1), to the right-hand side of Equation 2-7. Figure 2-4 shows the same data as shown in Figure 2-3, in dB, but separated for the φ and θ components; for this example, these can also be designated the *co-* and *cross-* polar patterns, respectively. In practice, for linear polarization, magnitude in the co-polar plane is generally around 20 dB above that in the cross-polar plane. The relationship between the total gain, in dB, and partial gains in the φ and θ components, is simply [22]:

$$G|_{dB} = 10\log_{10}\left(G_{\varphi} + G_{\theta}\right)$$

Equation 2-9

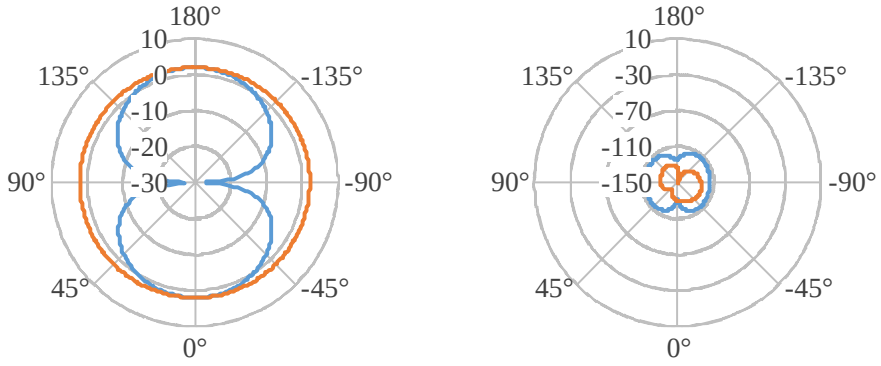

Figure 2-4. Simulated direcitvity in decibels for (*left*) φ component, and (*right*) θ component, for the half-wave dipole of Figure 2-2; (orange) azimuth plane, (blue) elevation plane. Note that average magnitude for φ component is at-least 100 dB above that for θ component.

There are a few different techniques for measuring the gain of an antenna; the most common of these is the gain transfer method [22]. The technique uses a standard gain antenna (SGA) as a reference antenna, to which the gain of the antenna under test (AUT) is related. The gain, G_{SGA}, and polarization (typically linear) of the SGA are pre-known. Figure 2-5 depicts a typical laboratory setup for gain measurement, with the transmit and receive antennas placed inside an anechoic chamber (to minimize wayward radiation and noise). A photograph of the laboratory setup at the University of Sheffield is shown in Figure 2-6.

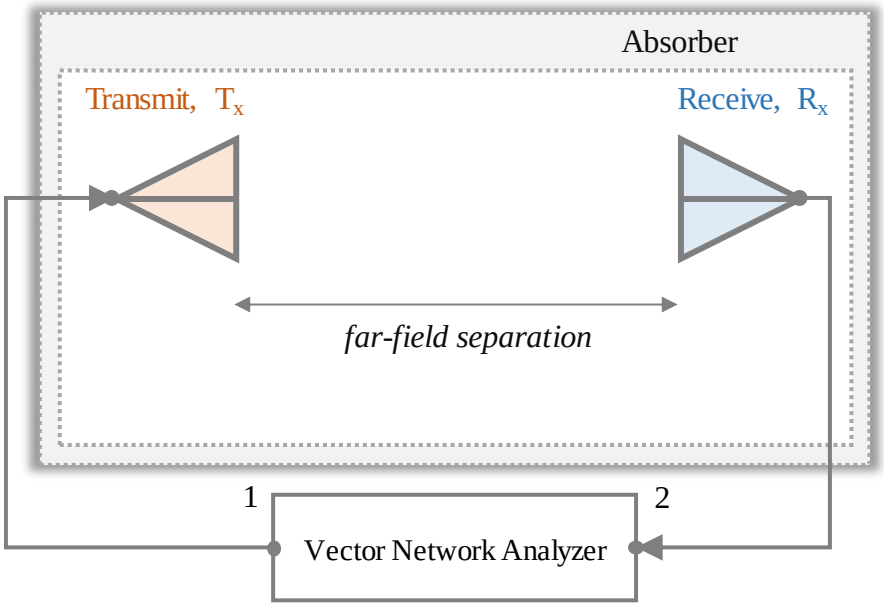

Figure 2-5. Setup for S_{21} measurements using VNA. The transmit and receive antennas are placed inside an anechoic chamber (absorber covered room walls) and separated from each other by a far-field separation.

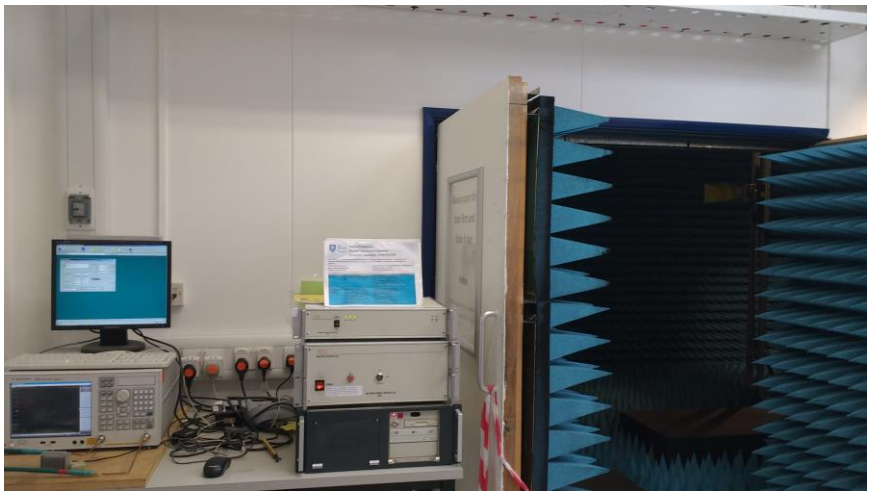

Figure 2-6. Photograph of the laboratory room showing the control circuitry and anechoic chamber for S_{21} measurements using Agilent E5071C VNA. NSI 800F-10 mounting arm (not visible) holds the AUT; a Rhode & Schwartz HF906 horn antenna is barely visible inside the chamber.

With the SGA fixed as the transmit antenna, two sets of S_{21} measurements are performed on the receive antenna: once for the power received with the AUT, termed P_{AUT}, and subsequently for power received with an identical SGA, termed P_{SGA}. For each set of measurements, the geometrical position of the transmit and receive antennas is fixed, as is the input power. In a two-port vector

network analyzer (VNA) system, S_{21} is essentially an expression of voltage gain (or attenuation) [81, 82], and can be expressed in terms of the voltage at port 2, V_2, and the incident voltage at port1, V_1, (or power) as :

$$S_{21} = 20\log_{10}\left(\frac{V_2}{V_1}\right) = 10\log_{10}\left(\frac{P_2}{P_1}\right)$$

Equation 2-10

Polarization and impedance mismatch factors are inherently present in such measurements. The total realized gain can then be expressed as [22]:

$$G_r|_{dB} = G_{SGA}|_{dB} + 10\log_{10}\left(\frac{P_{AUT}}{P_{SGA}}\right)$$

Equation 2-11

The measurement steps undertaken are:

1. Set the SGA‡ as the transmit antenna (port 1 of VNA) and the AUT as the receive antenna (port 2 of VNA)
2. Note the S_{21} measurement at the frequency of interest, in dB, as $S_{relative}$
3. Replace the AUT with an identical SGA as the receive antenna (port 2 of VNA); frequency, input power, and separation are kept constant
4. Note the S_{21} measurement, in dB, as $S_{reference}$
5. Note the gain of the standard gain antenna, G_{SGA}, at the frequency of operation
6. The realized gain of the AUT at that frequency is then:

$$G_{AUT}|_{dB} = G_{SGA}|_{dB} + \left(S_{relative}|_{dB} - S_{reference}\big|_{dB}\right)$$

Equation 2-12

Note from Equation 2-10 and Equation 2-11 that $S_{relative}$ is the relative gain of the AUT over the SGA. The term $S_{reference}$ is the gain of the SGA (receive) over the SGA (transmit), and may be thought of as a calibration term to find the absolute gain of the AUT by calibrating out the propagation losses.

‡ Note that it is not necessary to use an SGA as the transmit antenna; it was used as per laboratory convention.

For measurements where the frequencies of interest were above 1 GHz, a Rhode & Schwartz HF906 horn antenna [83] was used as the transmit and reference antenna. For frequencies below 1 GHz, no SGA was available, and the same measurement setup was used to obtain the radiation patterns of the AUT without peak gain information.

2.1.2. Input Impedance

Antennas being transducers, it is important to establish a metric which quantifies the coupling between the input signal and the radiated EM fields. Generally referred to as the **matching** of the antenna, it may be characterized by several metrics, including voltage standing wave ratio, return loss, and S_{11}. All of these depend on the **input impedance** (impedance at the terminals) of the antenna; the antenna's input impedance, Z_A, (as a function of frequency) is typically written in terms of its real and imaginary components as [22]:

$$Z_A = R_A + jX_A = (R_{rad} + R_{loss}) + jX_A$$

Equation 2-13

where R_{rad} is radiation resistance, R_{loss} is loss resistance (comprising of conductional and dielectric losses), R_A is the total antenna resistance, and X_A is reactance (determined primarily by the self-inductance and self-capacitance within the antenna structure). Denoting the characteristic impedance of the transmission line feeding into an antenna as Z_{TL} (note that Z_{TL} is treated as 50 Ω throughout this Thesis), its normalized input impedance, Z_{NA}, is given by:

$$Z_{NA} = \frac{Z_A}{Z_{TL}}$$

Equation 2-14

At the frequency of operation (often resonance), Z_{NA} for an antenna should ideally equal $1 + j0$, implying the absence of a reactive component, and with the resistive component of the antenna's impedance equalling that of the transmission line. Resonance is defined as the frequency point(s) where the reactive component of impedance equals zero [22]; an antenna can be made self-

resonant by tuning the feed point inductance, L, and capacitance, C, such that the total feed point reactance equals zero. This condition can be expressed mathematically in terms of the capacitive and inductive reactances, X_C and X_L respectively, as [19]:

c

With the reactance tuned to zero, there is still the remaining challenge of tuning the feed point resistance of the antenna to 50 Ω – assuming typical usage in a 50 Ω system. (Note that if the antenna is meant to be incorporated in a system with a different characteristic impedance, say 10 Ω, then its resistive component needs to also be 10 Ω for a good match.)

The preceding is an ideal scenario which would result in a impedance mismatch factor, M, of 1; the relationship between M and impedance is given by [22]:

$$M = 1 - \left|\frac{Z_A - Z_{TL}}{Z_A + Z_{TL}}\right|^2 = 1 - |\Gamma|^2$$

Equation 2-15

where Γ is termed the **voltage reflection coefficient** and is the complex ratio of the reflected signal, V_r, to the incident signal, V_i, at a terminal [22]:

$$\Gamma = \frac{V_r}{V_i}$$

Equation 2-16

The reflections (illustrated in Figure 2-7) occur where a mismatch exists between the antenna and the transmission line; the ratio of the peak-to-minimum amplitude of the resulting standing wave is termed the **voltage standing wave ratio** (VSWR), which can be expressed in terms of Γ as [22]:

$$VSWR = \frac{1 + |\Gamma|}{1 - |\Gamma|}$$

Equation 2-17

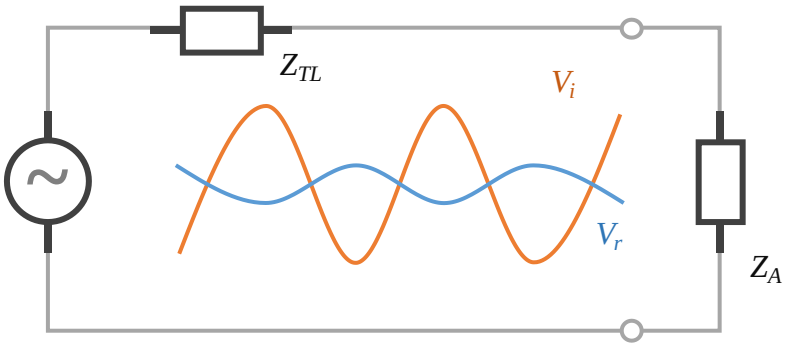

Figure 2-7. Illustration of incident, V_i, and reflected, V_r, signal at the input terminals of an antenna connected to a transmission line.

A similar ratio of the incident to reflected power is termed **return loss**, RL, given in the linear scale by [11]:

$$RL = \frac{P_i}{P_r} = \left(\frac{V_i}{V_r}\right)^2$$

Equation 2-18

where P_i is the power in the incident signal, and P_r is the power in the reflected signal. As with directivity and gain, return loss is often presented in the decibel scale; using Equation 2-18 and Equation 2-1, the expression becomes:

$$RL|_{dB} = 10\log_{10}\left(\frac{P_i}{P_r}\right) = 20\log_{10}\left(\frac{V_i}{V_r}\right)$$

Equation 2-19

Using Equation 2-16 and Equation 2-19, return loss can therefore be represented as a function of Γ as:

$$RL|_{dB} = -20\log_{10}|\Gamma|$$

Equation 2-20

The parameter return loss can also be expressed in terms of the parameter S_{11}, which is often the parameter measured using a VNA. In a two-port VNA system, S_{11} is essentially the voltage reflection coefficient, Γ [81, 82]. Thus, using Equation 2-20, it may be equated, in the dB scale, to the return loss and the input impedance of the antenna as:

$$S_{11}|_{dB} = 20\log_{10}\left(\frac{V_r}{V_i}\right) = -RL|_{dB} = 20\log_{10}\left|\frac{Z_A - Z_{TL}}{Z_A + Z_{TL}}\right|$$

Equation 2-21

Figure 2-8 shows the Agilent E5071B VNA in the University of Sheffield research laboratory, which was used for all S_{11} measurements reported in this Thesis; the required steps are:

1. Connect a transmission line cable with Z_{TL} 50 Ω to port 1 of VNA
2. Calibrate to the termination of the cable so that the unloaded S_{11} response is 0 dB over the entire range of frequencies
3. Capture the S_{11} data; post-process as desired

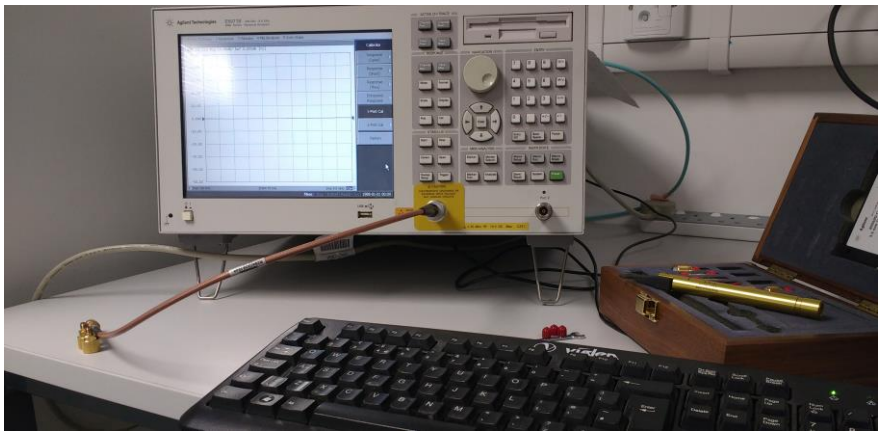

Figure 2-8. Photograph of the Agilent E5071B VNA used for S_{11} measurements, shown here with the accompanying calibration kit.

S_{11} is the parameter used throughout this Thesis to evaluate the impedance match of antennas presented. An S_{11} of 0 dB implies that all the incident power is reflected from the antenna; a value of −3 dB implies that half of the incident power is reflected, and is commonly used to mark the **half-power bandwidth** of the antenna. In other words, half of the incident power is available to the antenna – split in some ratio into the power that is radiated and the power that is absorbed as losses in the antenna. It is common to define the practical bandwidth of an antenna as the range of frequencies where its S_{11} is below −10 dB (10% of incident power reflected, 90% available to antenna). The S_{11} of an antenna therefore tells us how well the antenna is matched at resonance, and the

range of frequencies over which it can be expected to perform up to some pre-defined standards. Note that other metrics might ultimately influence the practical bandwidth, including but not limited to gain, polarization, and/or efficiency.

2.1.3. Radiation Efficiency

The efficiency of an antenna may be characterized by its radiation or total efficiencies. From Equation 2-6, we observe that the radiation efficiency can be derived from the gain and directivity of the antenna, if both are available. **Radiation efficiency** is defined as the power radiated by an antenna, P_{rad}, relative to the power accepted by the antenna, P_{in}, [22, 26] and may be related to the radiation resistance and loss resistance as :

$$\eta_r = \frac{P_{rad}}{P_{in}} = \frac{P_{rad}}{P_{rad} + P_{loss}} = \frac{R_{rad}}{R_{rad} + R_{loss}} = \frac{R_{rad}}{R_A}$$

Equation 2-22

If the losses due to impedance mismatch are considered, the realized radiation efficiency (or **total efficiency**) of the antenna is obtained, and is a useful practical metric for assessing the performance of an antenna in a system.

A common measurement method employs the use of a Wheeler cap [28] to separate the R_{rad} and R_{loss} terms to subsequently compute the efficiency. Theoretically, a PEC in the shape of a sphere and the electrical size of one radiansphere would prevent any radiation from the antenna, whilst not disturbing the antenna's near-field [84, 85]. In practice, the geometry may be different, for instance a cuboid, and the size is non-critical as long as radiation is prevented and near-fields left undisturbed [11].

Using the constant-loss-resistor method [86], reflectivity (or S_{11}) measurements easily obtained from a VNA can be used to obtain the R_{loss} and R_A terms required to compute efficiency. The technique works for resonant antennas (i.e. ideally no reactive component), with the key assumption that R_{loss} remains constant

with and without the Wheeler cap encasing the AUT. An equivalent circuit model showing only the resistive components is shown in Figure 2-9.

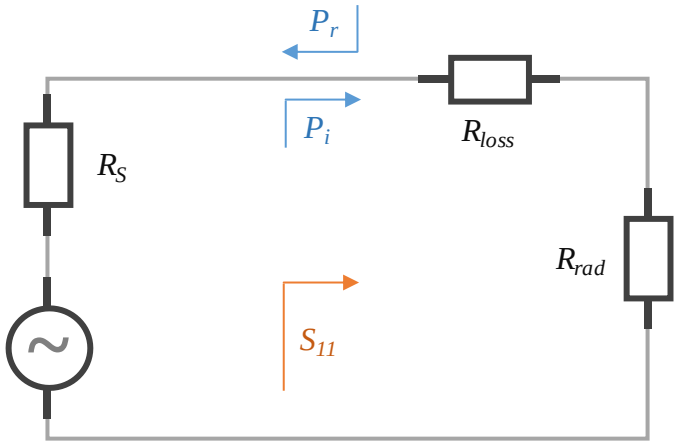

Figure 2-9. Equivelent circuit model of an antenna showing source resistance, R_s, and the loss and radiation resistance terms in antenna.

The technique is shown to compute the efficiency to satisfactory levels and is commonly employed for ESA measurements; it is favoured here over other, more precise techniques due to comparative ease of measurement [11]. Figure 2-10 illustrates a typical measurement setup. With the cap in place, reflecting all the power radiated by the AUT, R_{rad} equals zero, leaving only the R_{loss} term. The expression for $S_{11(WC)}$ becomes [86]:

$$S_{WC} = \frac{R_{loss} - R_S}{R_{loss} + R_S}$$

Equation 2-23

A subsequent measurement in free space then yields R_A. The expression for $S_{11(FS)}$ is [86]:

$$S_{FS} = \frac{(R_{rad} + R_{loss}) - R_S}{(R_{rad} + R_{loss}) + R_S}$$

Equation 2-24

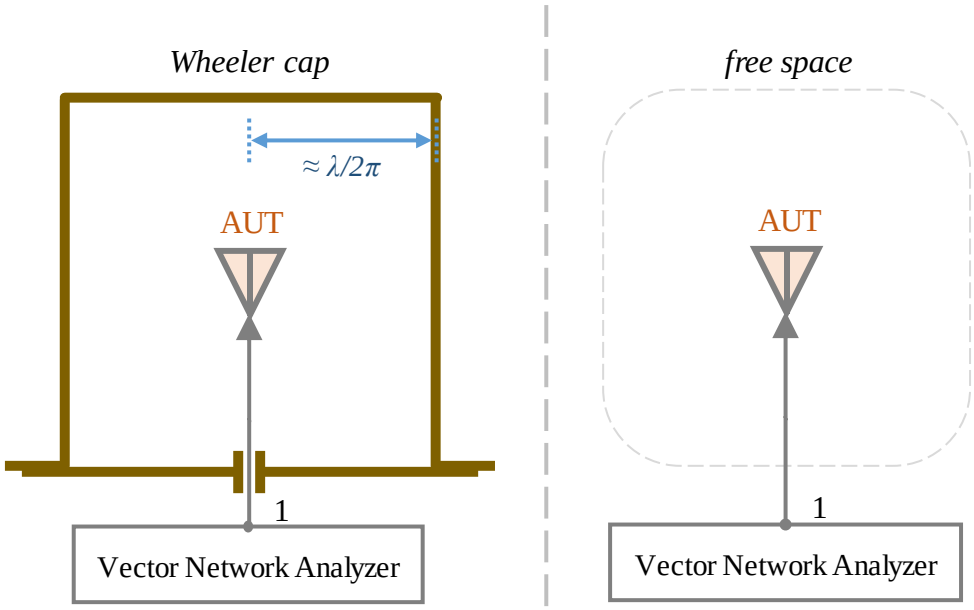

Figure 2-10. S_{11} measurement setup with (*left*) Wheeler cap on, and (*right*) in free space. Cross-sectional view.

This method is used to compute radiation efficiency from measurements for all such data presented in this Thesis. The measurement steps undertaken are:

1. Connect a transmission line cable with Z_{TL} 50 Ω to port 1 of VNA
2. Calibrate to the termination of the cable so that the S_{11} response is 0 dB over the entire range of frequencies
3. Place the AUT inside a suitably sized Wheeler cap and note the S_{11} measurement, in linear scale, as S_{WC}
4. Remove the Wheeler cap and note the free space S_{11} measurement, in linear scale, as S_{FS}
5. Manipulating Equation 2-23 and Equation 2-24 to obtain expressions for R_{rad} and R_{loss}, the radiation efficiency is given by:

$$\eta_r = 1 - \frac{(1 - S_{FS})(1 + S_{WC})}{(1 + S_{FS})(1 - S_{WC})}$$

Equation 2-25

2.1.4. Quality Factor

As previously mentioned, S_{11} is the metric most often used to define the bandwidth of an antenna. However, there is inherent ambiguity in any such definitions; it is equally common to find the bandwidth quoted in terms of half-power (S_{11} = −3 dB), 2:1 VSWR (S_{11} ≈ −9.5 dB), 90% accepted power (S_{11} = −10 dB), and so on. To do away with this vagueness, an alternative metric is often employed when analysing ESAs: the quality factor, *Q*. Defined as the ratio of reactive energy to accepted power, *Q* can also be related to the FBW of a resonant antenna [19]:

$$Q_{antenna} = \frac{(VSWR_{-3dB} - 1)}{FBW_{-3dB}\sqrt{VSWR_{-3dB}}}$$

Equation 2-26

where $VSWR_{-3dB}$ is the half-power voltage standing wave ratio (equivalent S_{11} value is −3 dB), which equals approximately 5.85:1, and FBW_{-3dB} is the half-power fractional bandwidth about resonance. For an antenna resonant at some centre frequency, f_c, located midway between a lower frequency, f_l, and an upper frequency, f_h, FBW is defined as [19]:

$$FBW = \frac{f_h - f_l}{f_c}$$

Equation 2-27

The relationship given by Equation 2-26 gives an approximation, formed under the assumptions that the self-resonant (or tuned) antenna exhibits a single impedance resonance and that the FBW is not too large [19]. ESAs exhibiting multiple, closely spaced resonances within their FBW might not be subject to this relationship – this is in fact an active topic of current research [26]. Note that for FBW_{-3dB}, f_h and f_l are the frequency points between which the S_{11} is equal or lower than −3 dB. It is acceptable to input VSWR and FBW values for some other value of S_{11} in Equation 2-26, as long as this is done consistently, e.g. $VSWR_{-6dB}$ and FBW_{-6dB}, or $VSWR_{-10dB}$ and FBW_{-10dB}, but not $VSWR_{-6dB}$ and FBW_{-10dB}. Using the quality factor in lieu of bandwidth allows for easier

comparison between various ESAs, particularly as there are fundamental limitations on the *Q* that are dependent on the antenna's electrical size and radiation efficiency (see Chapter 1).

2.2. Fabrication Methods

This section provides an overview of common and incipient fabrication methods for the manufacture of antennas. Limitations of a conventional process (photolithography) are highlighted in the context of inherently 3D antenna structures; potential alternative fabrication methods are stated, with emphasis on AM methods.

2.2.1. Photolithography

Photolithography (optical lithography) is a popular process for the fabrication of integrated circuits and PCBs, including printed antennas [87]. A generic outline of the process is presented in Figure 2-11.

For low throughput fabrication, as with research, the first step in a typical photolithography process is typically to coat the entirety of the substrate's surface with metal (via thin film deposition processes such as vacuum deposition, or direct sputtering [88]; this may be followed by electroplating to increase the thickness of the metal). Often, this initial step is skipped in favour of purchasing metallized substrates, for instance copper clad FR4. The next step is proper alignment of the metallized substrate under a photomask; this may be either a positive or a negative mask, depending on the type of photoresist used. Photoresists are classed as either positive tone (soluble in a specialized developer solution once exposed to light) or negative tone (insoluble in specialized developer solution once exposed to light). Once the substrate material is coated with a suitable resist, it is exposed to light (depending on the tone of the resist, a photomask either allows or blocks light through to the area of interest). A specialized developer solution (again, dependent on the photoresist used) is then used to remove any excess resist that remains. The result is a substrate with defined metallic tracks and geometries as per the required application (e.g. see patch antenna model in Figure 2-1).

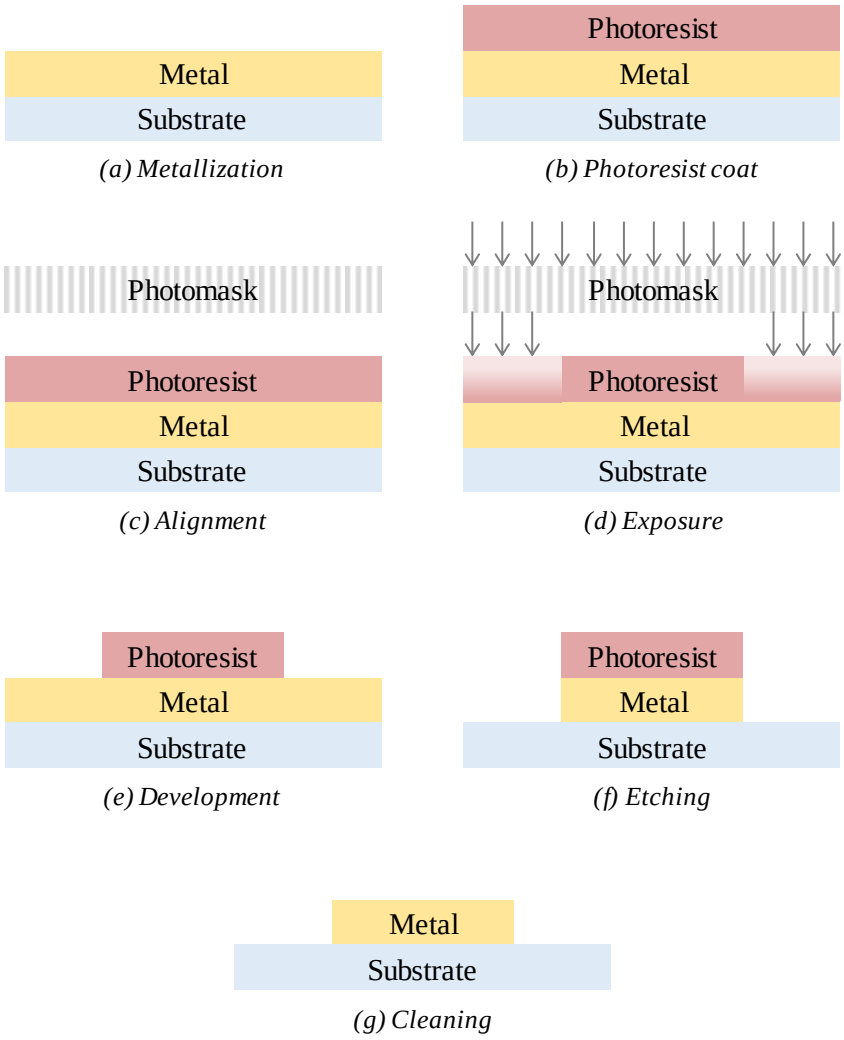

Figure 2-11. Illustration of generic photolithography process steps.

It is widely acknowledged that the key to a uniform (profile of) metal coating is good alignment between the substrate and the photomask. Often, these two need to be in (near) contact to minimize any diffraction of the light passing through; diffracted fields would result in uneven exposure and subsequently hinder the development of the photoresist. As such, a key limitation of traditional photolithography processes is their unsuitability to non-planar substrate topologies.

Several solutions have been proposed to overcome this limitation [23, 89-92]. One is the use of conformal photomasks, designed to mate as closely as possible with the desired non-planar substrate; this approach is very limited in the types of substrates that can be accommodated, often allowing for only the simplest non-planar topographies. An alternative is to directly write onto a substrate

material with conductive ink, or alternatively etch using a laser; these approaches are, however, limited to a low throughput due to the need to scan the entirety of the substrate surface in a serial manner. A popular alternative fabrication method, namely computer numerical control (CNC) machining, is similarly limited due to its approach of milling away excess metal from substrates. Whilst modern CNC mills may have multi-axis control, resulting in the capability of forming complex 3D parts, often the process results in a large amount of waste (when compared to additive technologies, discussed later).

Another alternative is the use of computer generated holographic (CGH) masks [23], which allow localized focusing of the optical wave fronts penetrating the mask. Figure 2-12 illustrates the behaviour of light which has been propagated through a conventional and a CGH photomask. Holography, in simple terms, is the process of storing/extracting 3D data in/from a 2D format, using the principle of interference of (coherent) optical wave fronts [93]. The combination of holography and photolithography, therefore, allows for the patterning of 3D substrates.

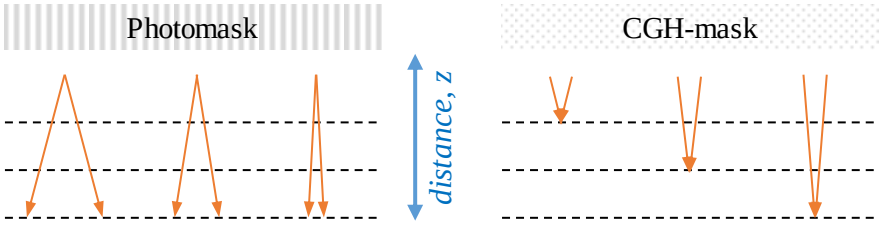

Figure 2-12. Illustration of the light propagated through a (*left*) conventional and (*right*) CGH photomask. As the distance away from the mask is increased, light passing through a traditional photomask diffracts, leading to a softening of the intensity at any particular desired location. CGH masks may be engineered such that there are multiple, distinct, locallized focal points across the projection area.

2.2.2. *Additive Manufacture*

Additive manufacture, also commonly known as 3D printing, is an umbrella term given to a range of processes where raw materials are joined up layer by layer to form objects [24, 94-96]; a distinction is made versus formative (desired object shape acquired through application of pressure to raw materials, for instance forging, bending, casting, compaction, etc.) and subtractive (desired object shape acquired by selective removal of material, for instance milling, drilling, etching, etc.) manufacturing processes [97].

The numerous technologies classified under AM may be grouped by the raw materials used (polymers and/or metals), the raw material delivery system (powder bed, wire feed, etc.), and the heat source (laser, electron beam), among others; a complete overview of the different technologies may be found in [24]. Through liaison with the Mercury Centre [98] in the University of Sheffield, powder bed fusion (PBF) processes were trialled to fabricate 3D antenna geometries. These are one of the earliest commercialized AM processes, and continue to be one of the most popular [24]. Compared to other AM techniques, its main advantages are low cost (due in part to its popularity and widespread adoption), and versatility (supports all types of raw materials); the main disadvantages (comparatively) are higher power consumption and lower build volumes.

Figure 2-13 gives a generic illustration of a PBF-AM printer. Pre-processing involves the conversion of a computer-aided design (CAD) model to a stereolithography (STL) file, which describes the meshed surface of the object or part. The STL file is subsequently loaded into an AM printer, where the specifics of build time, resolution, temperature may be adjusted. A rake or a roller is used to distribute powder from the cartridges onto the work area, creating a thin (typically 100 μm) layer of powder. The heat source is then guided to deliver energy to the surface of the powder bed, melting[§] and/or sintering the powder into the desired shape. A new layer of powder is subsequently deposited onto a lowered powder bed, melted, and the process repeated to realize the 3D solid object or part. Surrounding powder remains loose and is often reclaimed to be used towards a future build.

[§] Note that in practice, various fusion processes take place simultaneously, as detailed in [24].

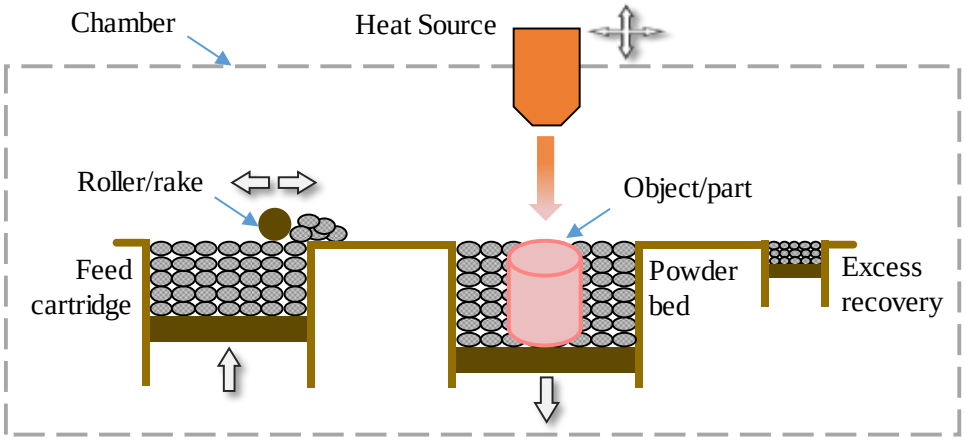

Figure 2-13. Illustration of generic PBF-AM printer.

There are two main sub-categories of PBF-AM: selective laser melting (SLM) and selective electron beam melting (SEBM), named for the type of heat source used. Lasers are typically rated between 100 to 400 W, and the electron beam up to 7 kW. The difference in heat source leads to some inherent differences in the printing process. In an SLM printer, the chamber is typically filled with inert gas in order to minimize oxidation and degradation of the powdered material. A pressurized vacuum environment is necessary in the SEBM printer, otherwise the bombarded electrons would interact with atoms in the gas and thus get deflected. The electron beam can also be moved a lot faster than the laser, leading to shorter build times. Energy delivered by the electron beam is, however, more diffuse than a laser, leading to a greater area affected by the heat. Consequently, the minimum feature size, resolution, and surface-finish of the SEBM process are typically worse off compared to SLM.

In both processes, the powder in the build platform is maintained at an elevated temperature, typically just below its melting point and/or glass transition temperature; the build platform itself may be heated with the help of resistive heaters. For SLM, this elevated temperature allows for lowering the power rating of the laser, and prevents faults that might arise due to non-uniform thermal expansion and contraction. In the SEBM process, the powder is further heated to slightly sinter the particles prior to bombardment from the electron beam. This is done primarily to increase conductivity throughout the powder, to allow the negatively charged electrons to swiftly affect the desired object region.

This eliminates the need for any sacrificial support structures under overhanging features, which are sometimes required in SLM printers.

Of the available printers, two were suitable for metallic printing. These were the laser based Renishaw AM250 [99] and electron beam based Arcam A2 [100]. Plastic support structures were outsourced and printed on machines supplied by EOS [101] and MakerBot [102].

CHAPTER 3

3. Miniaturization using Centrally Populated Digitated Structure

In this chapter, a novel contribution to small antenna design is introduced – the **centrally populated digitated structure**. The first section compares a traditional, rectangular IFA (RIFA) with a miniaturized circular IFA (CIFA), which forms the basis of the antenna profile used throughout this Thesis. This is followed by the analysis of Inverted-F and planar inverted-F antennas miniaturized with this technique.

3.1. From a Traditional Inverted-F to a Compact, Circular, Inverted-F Antenna

As previously discussed, practical designs of ESAs must incorporate ways to miniaturize an antenna (i.e. lower the resonance frequency for fixed overall dimensions), ensure that conductive and dielectric losses are minimized (reduce R_{loss}), and improve the impedance match at resonance (minimize X_A and increase R_{rad} to 50 Ω). The printed IFA was chosen for further investigation, primarily due to the ease of manufacture with traditional photolithography techniques, and in part due to its ubiquity in electronic devices. This section compares a typical, traditional IFA to a compact, circular profile IFA, which is subsequently miniaturized and optimized.

3.1.1. Traditional inverted-F antenna design

A traditional RIFA is designed for resonance at 2 GHz; the CAD model consists of copper (conductivity, σ = 5.8E+7 Sm^{-1}) metallization and lossy FR4 (ε_r = 4.3, and loss tangent, tanδ = 0.025) as the substrate. Note that copper and FR4 are modelled as 35 μm and 0.8 mm thick respectively throughout, unless otherwise stated. Figure 3-1 shows the front and back of the CAD model. The radius of the maximum circumscribing sphere, *a*, is 30 mm. A solder pad is the only metallization on the back of the antenna; a discrete port is used here to model the antenna feed. At the point of self-resonance, the antenna has a *ka* value of 1.26. Note that the total length of the radiating arm and the side length of the ground plane are approximately equal. The 2 GHz operating frequency was chosen for practical reasons; antennas operating at higher frequencies would be too small to easily fabricate or measure, whereas antennas operating at lower frequencies could not be measured for gain using the HF906 standard gain antenna (minimum operating frequency 1 GHz) available.

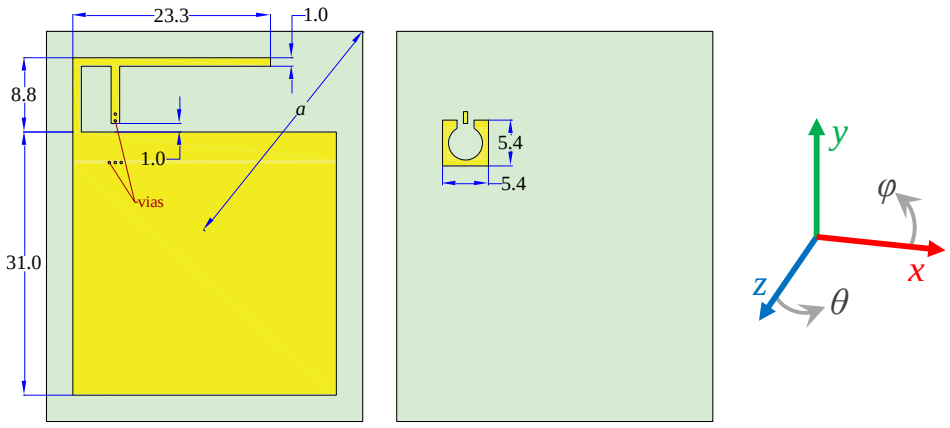

Figure 3-1. (*left*) Front and (*right*) back view of traditional RIFA designed for resonance at 2 GHz. All dimensions are given in mm. Via locations labelled with red dots.

3.1.2. Circular inverted-F antenna design

A compact, circular IFA (CIFA) is realized by truncating the long ground plane found in traditional designs, and by bending the radiating arm of the antenna in along a circular arc. The dimensions are chosen so as to achieve self-resonance

close to 2 GHz. Note that in order to achieve resonance near 2 GHz, the length of the curved radiating arm needs to be approximately equal to that of the radiating arm of the RIFA. Figure 3-2 shows the front and back of the CAD model; the dimension, *a*, also the radius of the antenna, is 12 mm. The simulated antenna is resonant at 2.15 GHz.

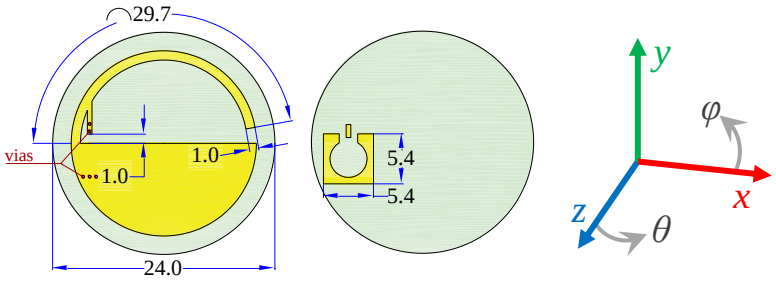

Figure 3-2. (*left*) Front and (*right*) back view of compact CIFA designed for resonance near 2 GHz. All dimensions are given in mm. Via locations labelled with red dots.

3.1.3. *Equivalent circuit*

Figure 3-3 shows the equivalent circuit model of the antennas discussed above. The capacitance, *C*, models the open circuit between the horizontal arm of the antenna and the ground plane; the inductance, *L*, models the loop created between the vertical length of the radiating arm and the short circuit at the feeding point. The real part of the antenna's impedance is modelled by the resistor, *R*. The overall dimensions of the antenna (specifically the length of the radiating arm) determine its resonant frequency; the location of the feed point can be tailored to alter *C* and *L* so as to achieve a purely resistive value of the input impedance.

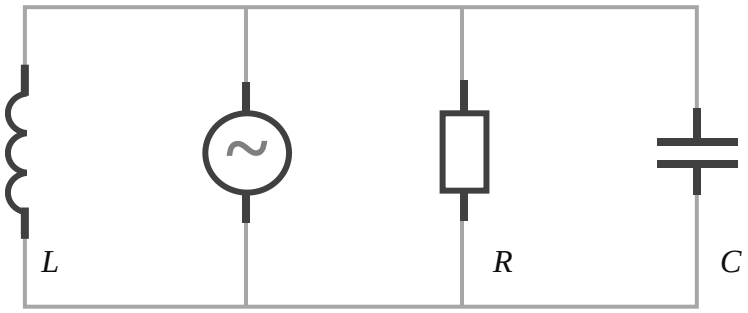

Figure 3-3. Equivalent circuit model for the RIFA and CIFA.

3.1.4. Performance comparison

The fabricated antennas are shown in Figure 3-4. The RIFA and CIFA were both measured to be resonant at 2.10 GHz. In order to examine the effects of the reduced ground plane and miniaturization, the measured realized gain patterns are presented in Figure 3-5 (RIFA, φ component), Figure 3-6 (RIFA, θ component), Figure 3-7 (CIFA, φ component), and Figure 3-8 (CIFA, θ component), as computed using the gain transfer method. Simulation results are also provided for comparison. It can be seen that the principal polarization of both antennas is in the vertical plane (φ component); measured gain for the φ component is on average slightly over 10 dB higher than for the θ component. Table 3-1 summarizes the average forward measured gain (±90°) for the two antennas.

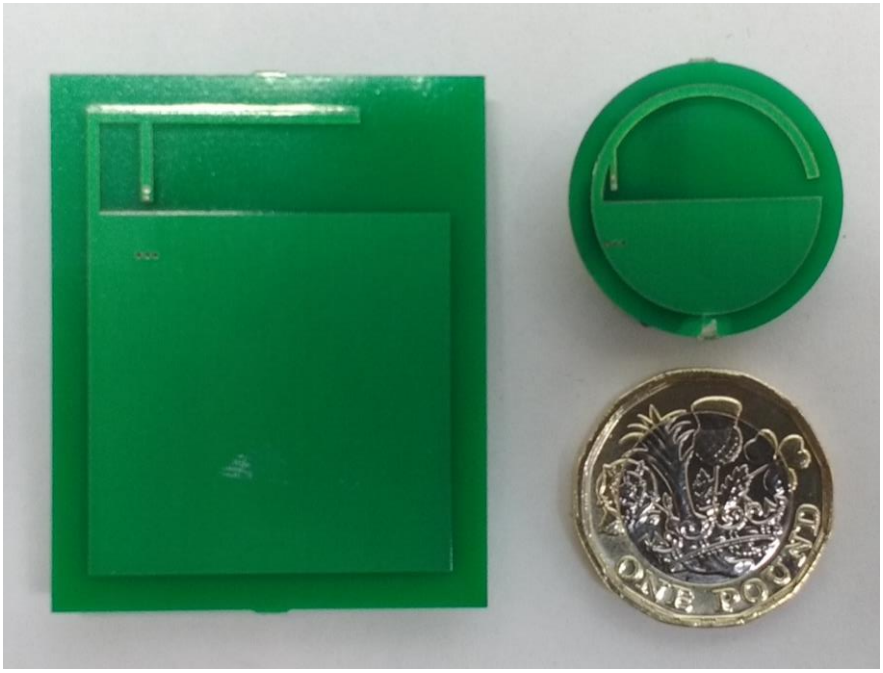

Figure 3-4. Photograph of the fabricated RIFA & CIFA.

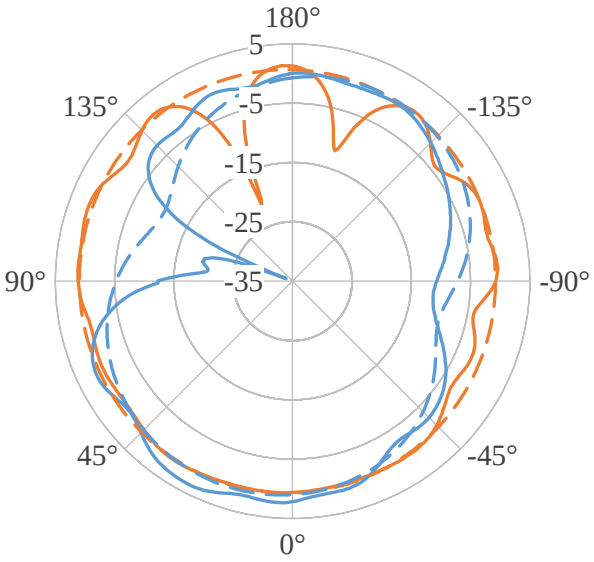

Figure 3-5. Realized gain (dBi) for the RIFA at 2.10 GHz; (——) measured, (– –) simulated; (orange) azimuth plane, (blue) elevation plane. φ component only.

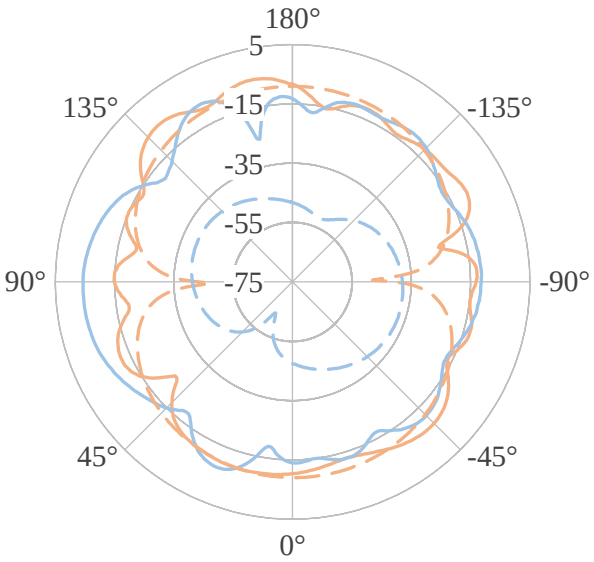

Figure 3-6. Realized gain (dBi) for the RIFA at 2.10 GHz; (——) measured, (– –) simulated; (light-orange) azimuth plane, (light-blue) elevation plane. θ component only.

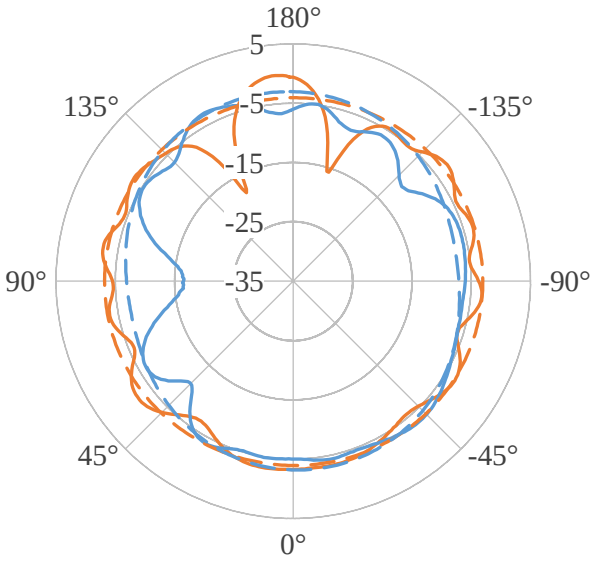

Figure 3-7. Realized gain (dBi) for the CIFA at 2.10 GHz; (——) measured, (– –) simulated; (orange) azimuth plane, (blue) elevation plane. φ component only.

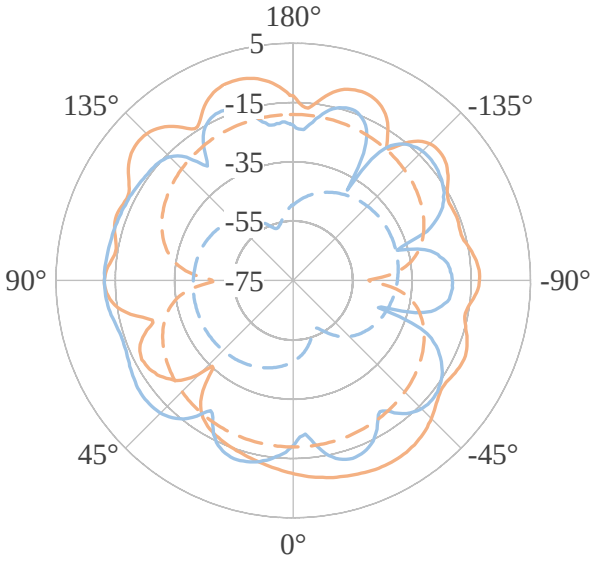

Figure 3-8. Realized gain (dBi) for the CIFA at 2.10 GHz; (——) measured, (– –) simulated; (light-orange) azimuth plane, (light-blue) elevation plane. θ component only.

Table 3-1. Summary of average forward measured gain (±90°) for the RIFA and CIFA. All values are presented in dBi.

	RIFA		CIFA	
	φ component	θ component	φ component	θ component
Measured azimuth plane	-0.30	-12.65	-4.17	-14.15
Simulated azimuth plane	0.38	-15.08	-3.49	-24.74
Measured elevation plane	-1.64	-12.12	-6.26	-16.58
Simulated elevation plane	-2.31	-43.97	-4.92	-45.18

The combined average forward measured gain (±90°) for the φ component is −0.97 dBi and −5.22 dBi for the RIFA and CIFA, respectively. In other words, there is a reduction of approximately 4 dBi in the average forward gain, which comes with a reduction in the respective *ka* values from 1.32 to 0.53 (using measured resonance at 2.10 GHz). For comparison, a recently published CPW-fed inverted-F antenna achieved a peak gain of 1.4 dBi at its centre frequency of 2.045 GHz, with a respective *ka* value of 1.67 [103].

This 4 dBi reduction in gain can alternatively be linked to a reduction in ground plane area from about $0.04\lambda^2$ to $0.01\lambda^2$. Whilst not strictly equivalent, a study on the effects of ground plane sizes of the closely related planar inverted-F antenna has demonstrated a steady decrease in gain (~ 4.7 dBi to ~ 1.2 dBi; a reduction of about 3.5 dBi) as the ground plane size was reduced from $2.8\lambda^2$ to $0.16\lambda^2$, with no further decrease as the size was reduced from $0.16\lambda^2$ to $0.04\lambda^2$ [104]. It should be noted that the precise effects of ground plane on the antenna performance are complex and are dependent, along with the ground plane size, on the relative placement of the antenna with respect to the ground plane [105].

To further investigate the performance of the antennas, the radiation efficiency is computed using the constant-loss-resistor Wheeler cap method. Results are

shown in Figure 3-9. Measurements were taken with the antennas parallel (straight connector) and perpendicular (right-angle connector) to the ground plane of the Wheeler cap. This was done to ensure precision in the measurements; a high discrepancy would indicate that either the antenna is not positioned centrally or the cap is too small and causing too much interference to the near field (a more detailed study on the accuracy and precision of radiation efficiency measurements can be found in Chapter 4). At their measured resonant frequency of 2.10 GHz, the RIFA has a maximum radiation efficiency of 88% and the CIFA of 49% (averaged); note that measurement precision is about ±10 percentage points. Hence, going by measured results, we see a drop of approximately 39 percentage points in the radiation efficiency as we move from a traditional IFA design to one that is more compact. For the sake of completeness, at their respective simulated resonant frequencies, the RIFA (2.00 GHz) had a simulated radiation efficiency of 92%, while for the CIFA (2.15 GHz) it was 60%.

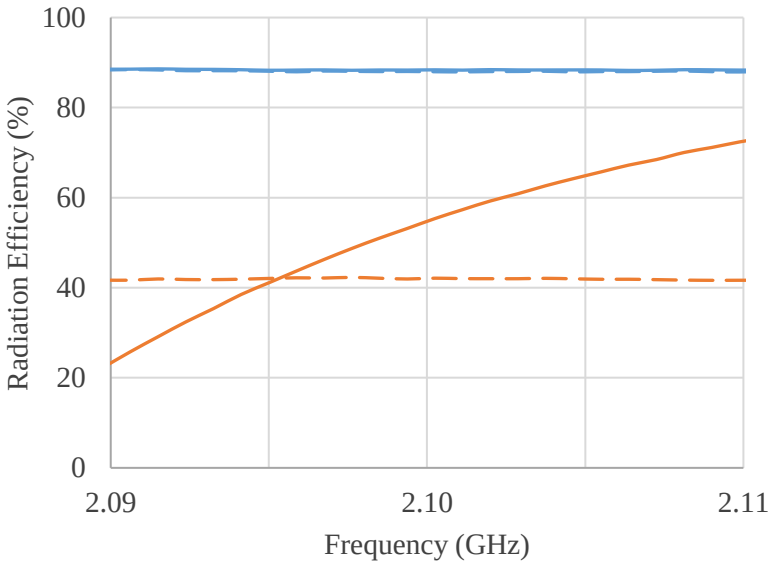

Figure 3-9. Measured radiation efficiency for (orange) CIFA, and (blue) RIFA; (——) straight connector (– –) right-angle connector. Plotted for ±10 MHz about resonance frequency.

3.2. 2.45 GHz Electrically Small Inverted-F Antenna

Based on the CIFA design presented above, the addition of a centrally populated digitated structure was proposed. This structure would raise the self-inductance and self-capacitance of the antenna, allowing for more precise impedance matching and the added benefit of further reducing the resonant frequency of the antenna.

3.2.1. Antenna Design – Mini-SMP Connector

An antenna based on this compact design, operating at a desired frequency of 2.4 GHz, was designed and optimized in CST MWS. The antenna was simulated with copper metallization on a 0.8 mm thick lossy FR4 substrate (ε_r = 4.3, tanδ = 0.025). For resonance at 2.4 GHz, the optimized design has a total diameter of 18 mm. Maintaining the same overall dimensions for a CIFA resulted in it resonating at 2.8 GHz. Figure 3-10 shows the front view of this circular, digitated IFA design (CDIFA$_{mSMP}$), along with the equivalent CIFA$_{mSMP}$ design having the same overall dimension. The antennas are fed from the bottom of the substrate, and the excitation of the radiating arm achieved using through-vias, as shown in Figure 3-10. The digits increase capacitance to the ground plane, as well as introducing several inductive loops to increase the antenna's self-inductance.

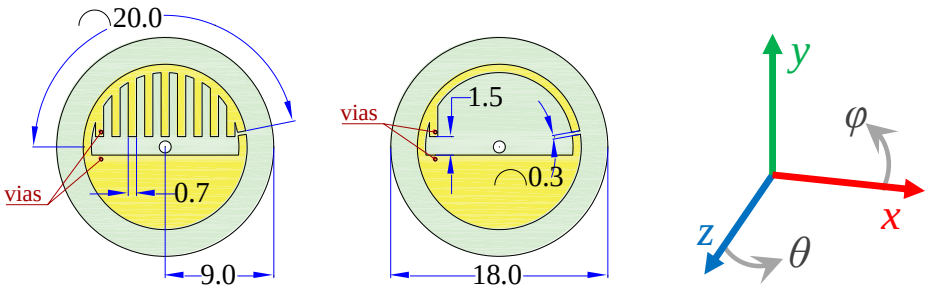

Figure 3-10. Front views of the (*left*) CDIFA$_{mSMP}$ and (*right*) equivalent CIFA$_{mSMP}$. All dimensions are given in mm. Via locations labelled with red dots.

The small physical size of the antenna necessitated the use of a mini-SMP (mSMP) connector; to allow for measurements, a custom mSMP–SMA adaptor was fashioned, as calibration kits for the VNA were only available with SMA type connections. A photograph of the fabricated $CDIFA_{mSMP}$ is shown in Figure 3-11. The adaptor shown is 4.5 cm long, and for simulations of the antenna with feed structure, is modelled as a coaxial cable of the same length.

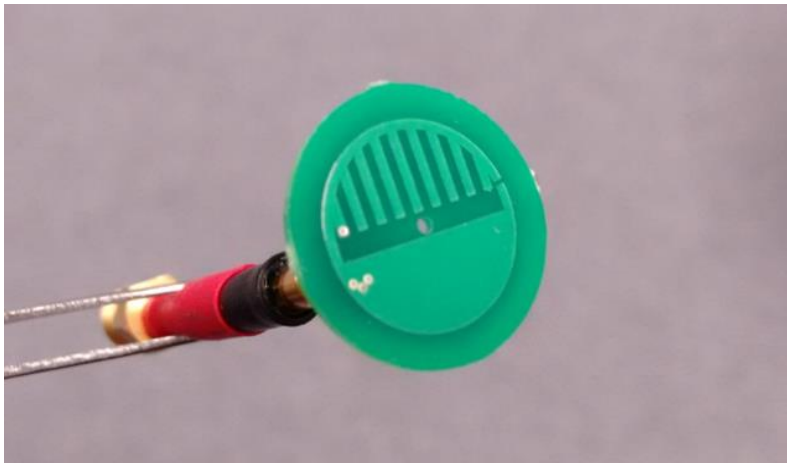

Figure 3-11. Photograph of the fabricated $CDIFA_{mSMP}$ mounted on a custom-made mSMP–SMA adaptor.

3.2.2. Results and Discussion – Mini-SMP Connector

Figure 3-12 compares the measured S_{11} of the $CDIFA_{mSMP}$ with simulated results. At the measured resonant frequency of 2.36 GHz, the measured impedance of the antenna is $49.1 - j1.6$ (Figure 3-13). The corresponding *ka* value for the antenna only is 0.44, and the FBW_{-3dB} equals 10%. Simulation results are provided for the antenna only model, as well as the model containing a length of coaxial cable. Of note is the additional loss incurred due to the feed cable, which has an effect on the magnitude of the return loss, widening the FBW_{-3dB}; these effects are well documented and something antenna designers need to be aware of when working with ESAs [11, 106]. For the sake of completeness, simulation results for the antenna-only model of $CIFA_{mSMP}$ are also included in Figure 3-12.

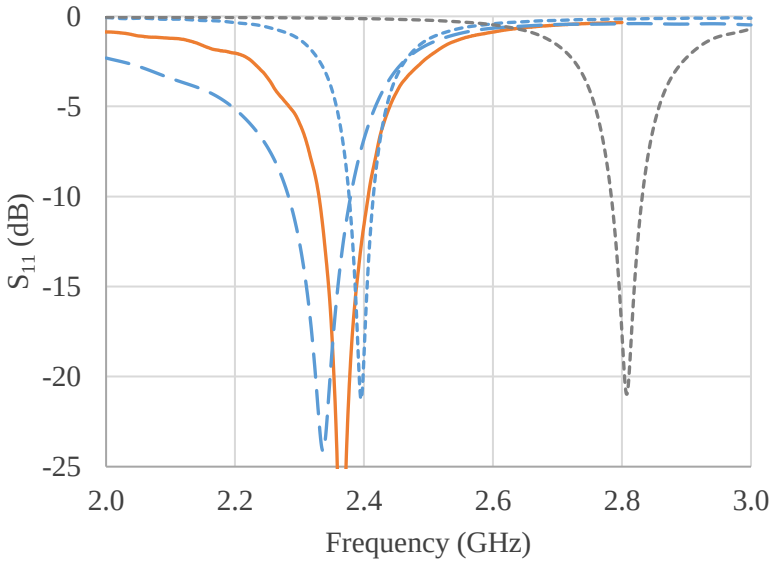

Figure 3-12. S_{11} results for the CDIFA$_{mSMP}$; (orange) measured, (blue) simulated; (– –) antenna with feed structure, (⋯) antenna-only simulation; (grey) CIFA$_{mSMP}$ antenna-only simulation.

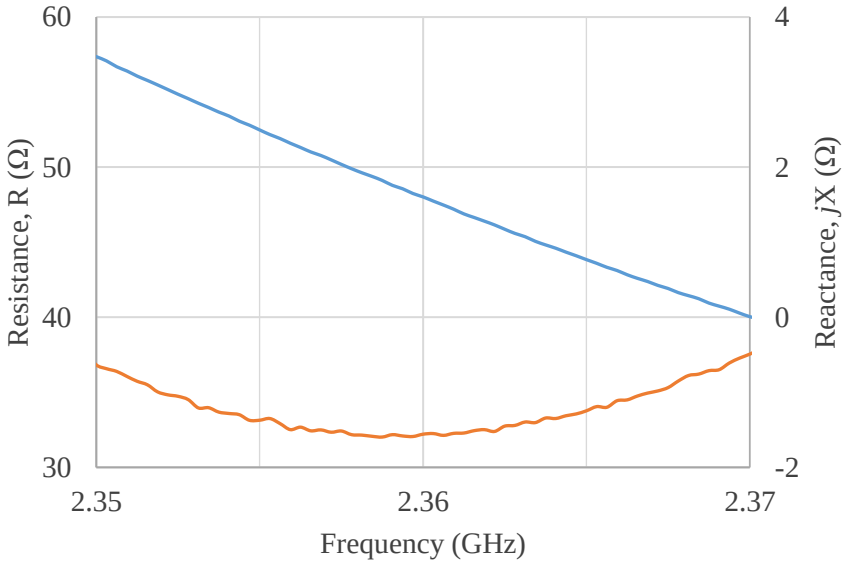

Figure 3-13. Measured input impedance of the CDIFA$_{mSMP}$; (orange) resistance, R, and (blue) reactance, jX. Plotted for ±10 MHz around the resonant frequency.

The radiation efficiency of the CDIFA$_{mSMP}$ was computed using the constant-loss-resistor Wheeler cap measurement method [86] (as described in Chapter 2), using an aluminium box of side length 10 cm; the results are plotted in Figure 3-14. Once again, simulation results are provided for the antenna only model, as well as the antenna with feed cable. At resonance, the measured radiation efficiency for the CDIFA$_{mSMP}$ is 70%, though it should be noted that there is a

~30 percentage point difference between simulations with and without the feed cable. Thus, the mSMP-SMA adaptor used here contributes significantly to the results obtained from efficiency measurements.

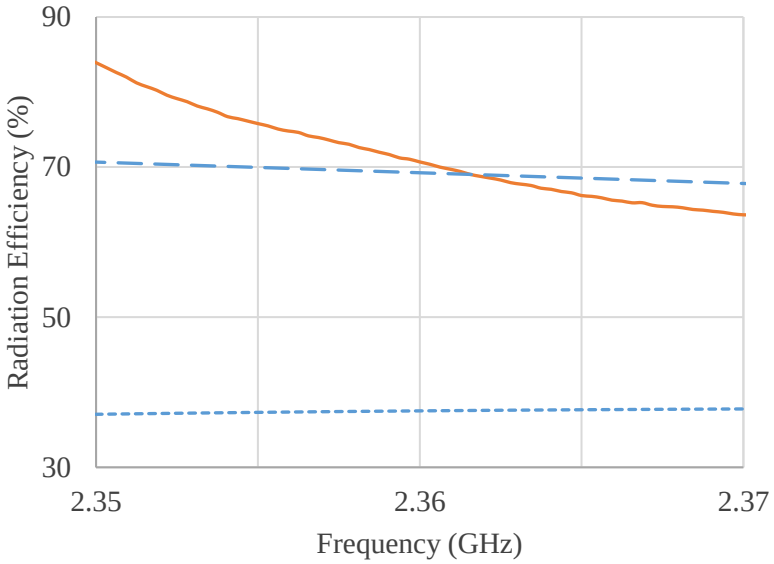

Figure 3-14. Radiation efficiency of the CDIFA$_{mSMP}$; (orange) measured, (blue) simulated; (– –) antenna with feed structure simulation, (⋯) antenna-only simulation. Plotted for ±10 MHz around resonance frequency.

The Q_{ratio}, as computed using Equation 1-4, is 2.1 for this antenna, using the *ka* value of 0.44 (antenna only). However, since the feed structure cannot be calibrated out of measurements and significantly alters the measured radiation efficiency of the antenna, a more accurate Q_{ratio} would incorporate the feed structure to get the overall radius, *a*, of an imaginary circumscribing sphere. Under this stipulation, the *ka* value of the antenna becomes 1.2, with a corresponding Q_{ratio} of 22.

Figure 3-15 shows the measured realized gain in decibels for this antenna, computed using the gain transfer method. Simulation results are provided for the antenna with feed structure (4.5 cm long coaxial cable). The small physical size of the antenna makes it difficult to measure the gain with precision; here, the partial gain from φ *and* θ components is combined to get the absolute total. It can be seen that for the azimuth plane, the measured and simulated gain values have a reasonable agreement; however, the same cannot be said for the elevation

plane. The measured average forward (±90°) realized gain of the CDIFA$_{mSMP}$ is −5.8 dBi; for simulated results, this value is −1.2 dBi.

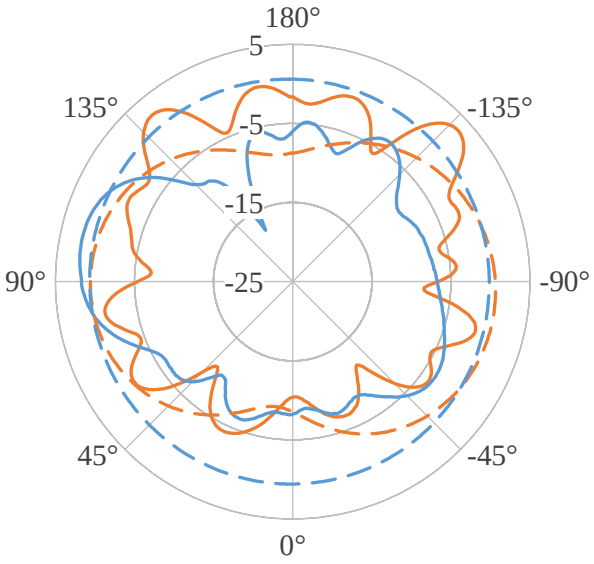

Figure 3-15. Realized gain (dBi) for the CDIFA$_{mSMP}$ at resonance; (——) measured, (– –) simulated (antenna with feed structure); (orange) azimuth plane, (blue) elevation plane. Combined absolute gain (φ and θ components).

3.2.3. *Antenna Design – SMP Connector*

To address the effects of the antenna feed structure on its Q_{ratio}, a second, identical[**] antenna was designed and fabricated, with a different connection terminus. As there were no pre-built adaptors available in the market with mSMP–SMA connections, and the small physical size of the antenna barred the use of a regular sized SMA connector, a compromise was reached with the use of SMP connectors, for which a Molex series 73386 SMP-SMA adaptor (length 16.5 mm) was available to purchase. It can be conjectured that calibration errors would be minimized since calibration can be performed up to the adaptor (which is shorter in length than the custom-made mSMP-SMA adaptor), and that the adaptor itself contributes less to any deviation in the antenna's performance. Consequently, only the solder pad on the reverse of the antenna is modelled where the effects of the feed structure are considered; the dimensions of this metallized structure are the same as those provided for the digitated structure in

[**] The front metallization of this antenna was identical to the previously discussed antenna; the only difference between the two is the size of the contact pad on the reverse of the substrate.

Figure 3-10; a photograph of the antenna and the SMP-SMA adaptor is shown in Figure 3-16.

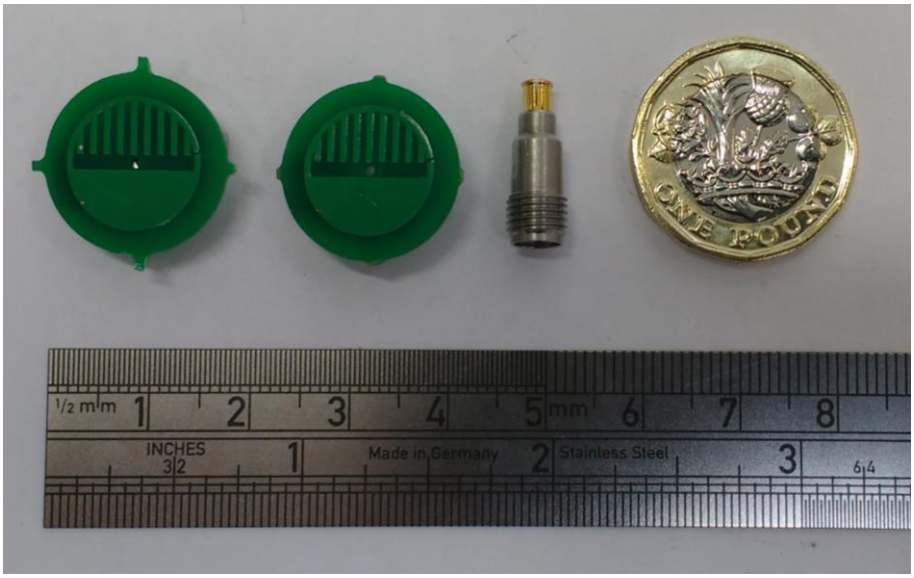

Figure 3-16. Photograph of two fabricated $CDIFA_{SMP}$ and Molex series 73386 SMP–SMA adaptor.

3.2.4. Results and Discussion – SMP Connector

The measured S_{11} for the $CDIFA_{SMP}$ is presented in Figure 3-17. Simulated results for the $CDIFA_{SMP}$ (including solder pad), as well as the previously presented simulation results for the $CDIFA_{mSMP}$ (i.e. antenna-only), are also included. The measured antenna, resonant at 2.33 GHz, has a frequency shift of 3% from the optimized design, and a FBW_{-3dB} of 15% (wider bandwidth as a result of increased losses). At this frequency, the CDIFA has a *ka* value of 0.44 considering only the antenna, and 0.59 if the Molex SMP-SMA adaptor is included to obtain the parameter *a*.

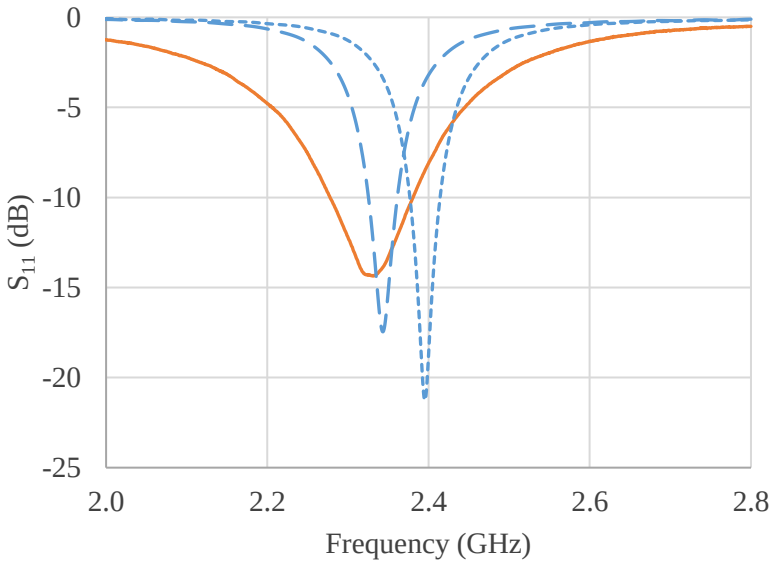

Figure 3-17. S_{11} results for the CDIFA$_{SMP}$; (orange) measured, (blue) simulated; (– –) antenna with SMP solder pad simulation, (⋯) antenna-only simulation.

The radiation efficiency of the CDIFA$_{SMP}$ was computed using the constant-loss-resistor Wheeler cap method, using a Wheeler cap box of side length 10 cm. The measured results are compared with simulations for the antenna with SMP solder pad in Figure 3-18; at resonance, the maximum measured radiation efficiency is 39%. In order to assess the effects of the orientation of the Wheeler cap with respect to the antenna, measurements were taken for two orientations of the Wheeler cap boxes (placed in parallel and diamond alignments, with respect to the ground plate below, see Figure 4-9); there was an average difference of 3 percentage points between the two readings. Furthermore, it can be seen that there is good agreement between measured and simulated results; as in fact there is between the two different simulation models.

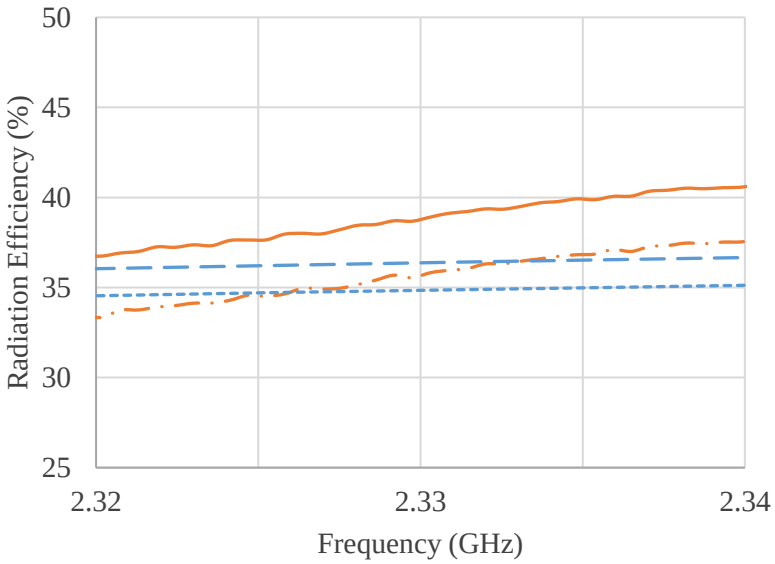

Figure 3-18. Radiation efficiency for the $CDIFA_{SMP}$; (orange) measured, (blue) simulated; (——) measurement with Wheeler cap box in parallel alignment, (– · –) measurement with Wheeler cap box in diamond alignment; (⋯) simulation for antenna with SMP solder pad, (– –) simulation for antenna-only. Plotted for ±10 MHz around resonance frequency.

Subsequently, using Equation 1-4, and substituting the *ka* value of 0.59 (SMP-SMA adaptor included), the Q_{ratio} for the CDIFA is computed to be 5.0 (excluding the adaptor yields a *ka* value of 0.44 with corresponding Q_{ratio} of 2.4).

Figure 3-19 shows the measured realized gain in decibels for this antenna, computed using the gain transfer method. The small physical size of the antenna made it difficult to measure the gain with precision; thus, the partial gain from φ and θ components is combined to get the absolute total (see Chapter 2). Simulation results provided here include the solder pad on the reverse of the antenna. The measured average forward gain of the $CDIFA_{SMP}$ is −8.2 dBi; for simulated results, this value is −5.0 dBi. Overall, there is slightly better agreement between measurements and simulations, as compared to the gain of the $CDIFA_{mSMP}$ provided in Figure 3-15.

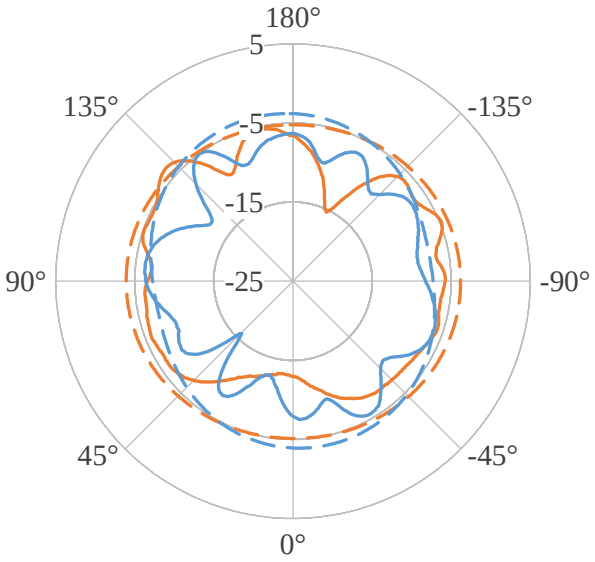

Figure 3-19. Realized gain (dBi) for the CDIFA$_{mSMP}$ at resonance; (——) measured, (– –) simulated (antenna with solder pad); (orange) azimuth plane, (blue) elevation plane. Combined absolute gain (φ *and* θ components).

3.2.5. *Comments*

An ESA, based on the compact CIFA introduced in the previous section, designed to resonate at 2.4 GHz, was modelled and optimized using CST MWS. To further reduce the electrical size of the compact antenna design, it was populated with a novel digit-like structure. This structure is demonstrated to increase the self-inductance and self-capacitance of the antenna, and allows for finer tuning to get impedance match close to 50 Ω. Due to the small physical size of the antenna, the use of an mSMP-SMA adaptor was necessitated, though this impeded the precise measurements of realized gain. At its measured resonance frequency of 2.36, the CDIFA$_{mSMP}$ has a *ka* value of 1.2 (including 4.5 cm custom-made adaptor), η_r of 70%, FBW_{-3dB} of 10%, and a corresponding Q_{ratio} of 22.

In order to avoid such a large feed structure, a similar antenna was fabricated using an SMP connector, for which a Molex series 73386 SMP-SMA adaptor was procured (length 16.5 mm). Measurements for the CDIFA$_{SMP}$ revealed a resonant frequency of 2.33 GHz, with a *ka* value of 0.59 (including adaptor), η_r of 39%, FBW_{-3dB} of 15%, and a corresponding Q_{ratio} of 5.

Gain pattern measurements were conducted for both the $CDIFA_{mSMP}$ and $CDIFA_{SMP}$, with neither exhibiting satisfactory agreement with respective simulations. The difference between simulations and measurements can be explained by a combination of the following: antenna not level with standard horn, antenna phase centre not coinciding with centre of rotation of mount, energy loss in soldered feed connectors, tolerance of substrate material properties (specifically losses), energy loss due to mSMP-SMA feed structure or SMP-SMA adaptor. Suggestions for improved measurement results are provided later as recommendations for future work.

3.3. 530 MHz Dual Resonance Electrically Small Planar Inverted-F Antenna

Bandwidth enhancement for ESAs was investigated with the use of two closely spaced resonances. Using a similar profile as the CDIFA, along with the addition of a ground plane on the reverse of the substrate, the antenna can be fed, as depicted in Figure 3-20, to support two current paths along the edges of the top metallization. Subsequently, resonances corresponding to the current paths may be engineered such that they fall close enough together to increase the effective bandwidth of the antenna. The resulting structure resembles a variant of the inverted-F antenna – the planar inverted-F antenna. The effects of a centrally populated digitated structure integrated within this new compact PIFA were investigated as a means to facilitate miniaturization.

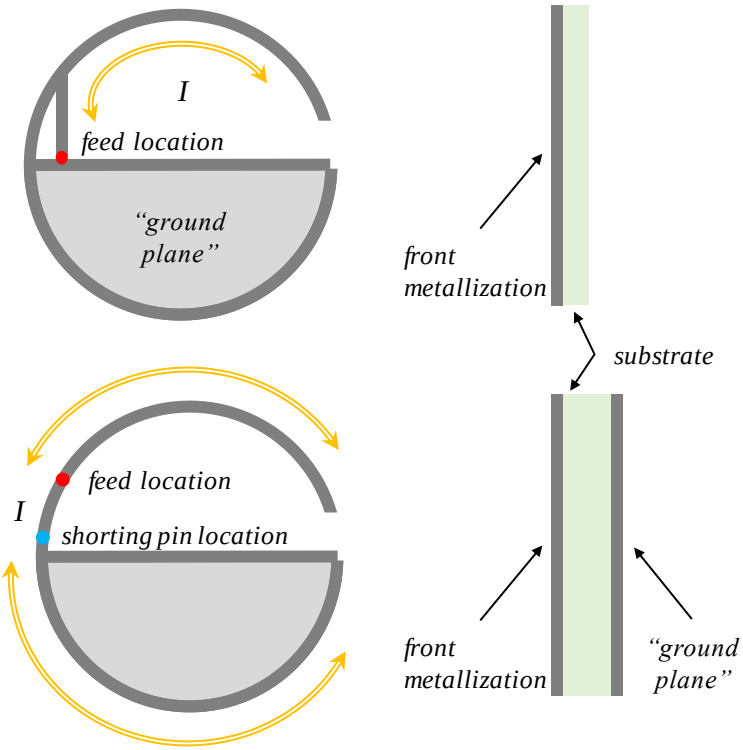

Figure 3-20. Illustration of the current paths on an (*top*) IFA and (*bottom*) PIFA. The ground plane acts to reflect the EM waves born of these currents, and create the so-called 'image antenna'.

3.3.1. Antenna Design

The circular, digitated, planar inverted-F antenna (CDPIFA) is derived from the CDIFA of the previous section. Fabrication considerations are the main reason for the different layout of the digits. Having shorter digits on either side of copper tracks allows for fewer support structures when building the antenna using AM (see Chapter 5). The layout is also prefered for holographic lithography where the negative space between metallizations can be projected using a computer generated holographic mask; the present structure was found to optimize faster and with a better contrast ratio when compared to the style of digits discussed previously.

Figure 3-21 shows the front view of this CDPIFA; the back is completely metallized and forms the ground plane of this type of antenna. For comparison, and to facilitate discussion of the optimized design, two variations of a simpler, circular PIFA design are also included (not to scale). These are termed $CPIFA_{1A}$

and CPIFA$_{2A}$, as they have one and two radiating arms respectively. For all antennas, the dimension *a*, also the radius, equals 25 mm. Figure 3-22 shows fabricated prototypes for the CDPIFA and the CPIFA$_{2A}$.

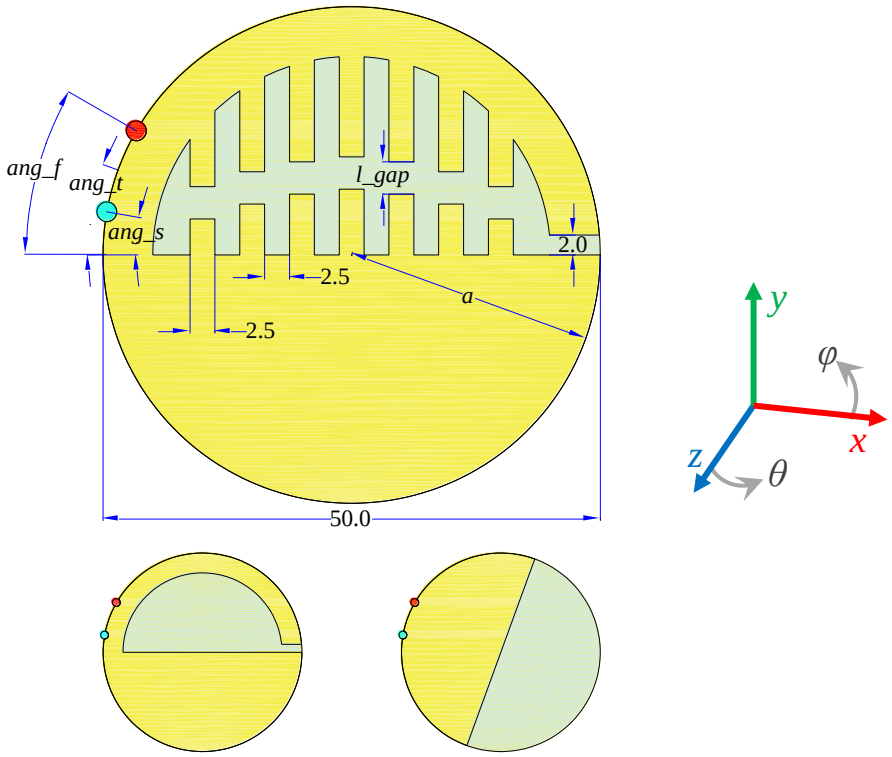

Figure 3-21. Front views of the (*top*) CDPIFA, (*bottom-left*) CPIFA$_{2A}$, and (*bottom-right*) CPIFA$_{1A}$. Red and Cyan dots designate position of feed point and shorting pin, respectively. Note that maximum overall dimension of all simulated and fabricated models is 50 mm.

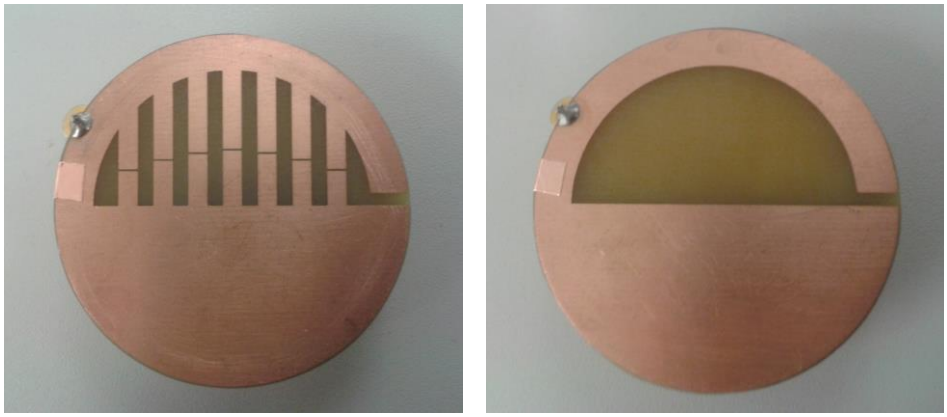

Figure 3-22. Photographs of the fabricated (*left*) CDPIFA and (*right*) CPIFA$_{2A}$.

3.3.2. Results and Discussion

Figure 3-23 shows the simulated S_{11} characteristics for the three antennas; where the parameters of the CDPIFA are as follows: *ang_f* = 30°, *ang_s* = 10°, *ang_t* = 20°, and *l_gap* = 0.50 mm. As illustrated, *ang_f* is the angle in degrees as measured from the line of azimuth of the antenna to the feed point, *ang_s* is a similar angle, but measured up to the shorting pin, *ang_t* is the angle measured up to the midway between the feed point and shorting point (when both are rotated in tandem with relative positions fixed), and finally *l_gap* is the distance in millimetres between the top and bottom digits. For simplicity, all other parameters of the digitated structure are kept constant.

Comparing the plots for $CPIFA_{1A}$ and $CPIFA_{2A}$, it is evident that dual resonance behaviour is established with the addition of a second radiating arm to the antenna. Moreover, the S_{11} plot for the CDPIFA exhibits two resonances close together around 540 MHz (with resonances evident at 530 MHz and 550 MHz). In an application where impedance matching is the primary marker for bandwidth, such a profile for return loss exhibits a much wider bandwidth than either of the two resonances of the $CPIFA_{2A}$. Furthermore, the resonances are themselves lower down the frequency scale due to the miniaturization effects manifested by the centrally populated digits.

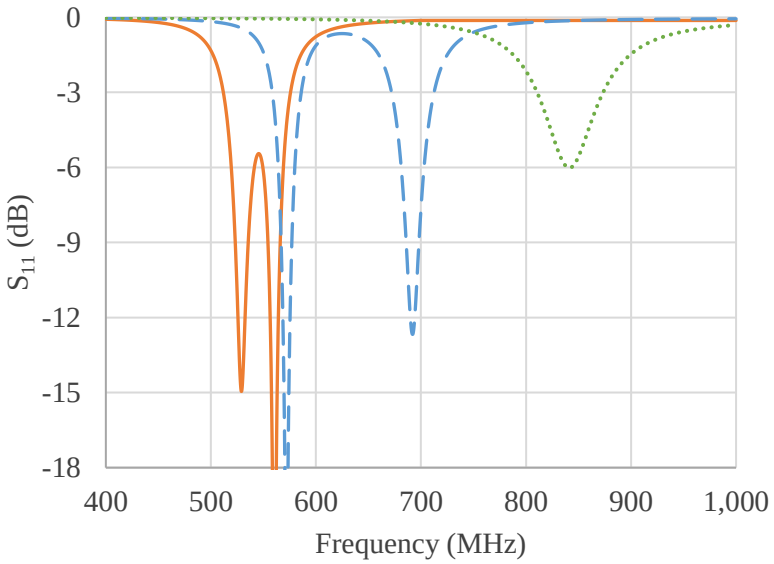

Figure 3-23. Simulated S_{11} for (orange) CDPIFA, (blue) $CPIFA_{2A}$, and (green) $CPIFA_{1A}$.

Here, a detailed review of the optimization process for the CDPIFA is presented, using the parameters highlighted in Figure 3-21, in order to examine the antenna's return loss behaviour. Parametric results for *ang_f*, *ang_s*, *ang_t*, and *l_gap* are provided in Figure 3-24, Figure 3-25, Figure 3-26, and Figure 3-27, respectively.

Varying the relative position of the shorting pin to the feed point – either by varying *ang_f* or *ang_s* results in changing the inductive loop formed in the PIFA. Varying the gap between the digits in *l_gap* results in changing the added capacitance. These parameters can therefore be altered to fine-tune the impedance match of the CDPIFA. Moreover, varying the parameter *ang_t* has the effect of changing the relative lengths of the available current paths, which in turn determines the frequency of resonance for the antenna. This parameter can therefore be tuned to bring the two resonances close together.

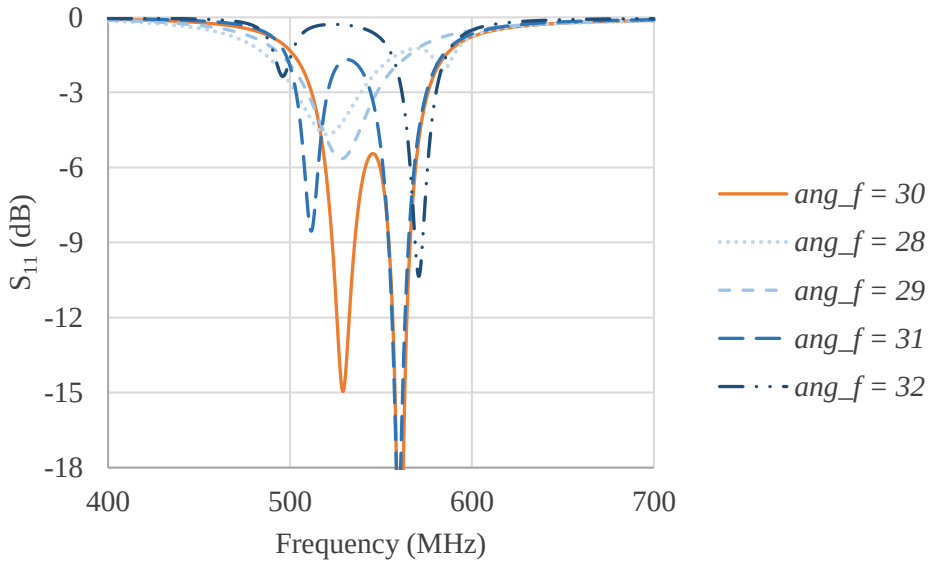

Figure 3-24. Simulated S_{11} for CDPIFA, parameterised *ang_f*. Legend shown to the right, units are degrees (°). Original parameter combination shown in orange.

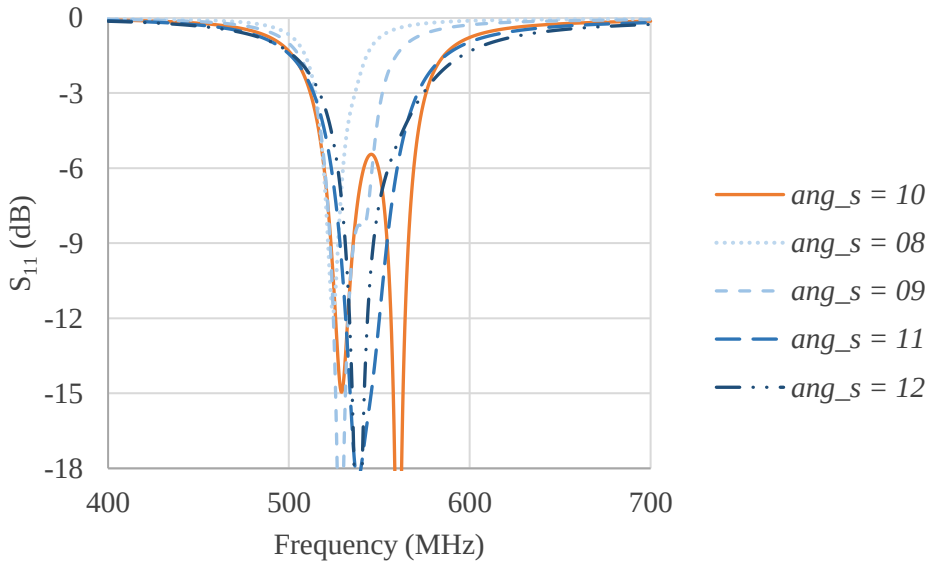

Figure 3-25. Simulated S_{11} for CDPIFA, parameterised *ang_s*. Legend shown to the right, units are degrees (°). Original parameter combination shown in orange.

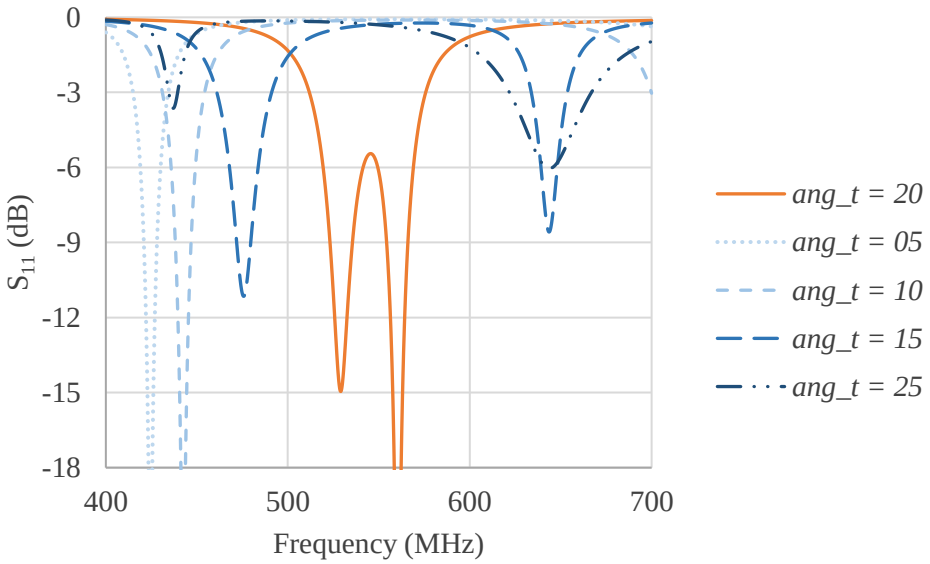

Figure 3-26. Simulated S_{11} for CDPIFA, parameterised *ang_t*. Legend shown to the right, units are degrees (°). Original parameter combination shown in orange.

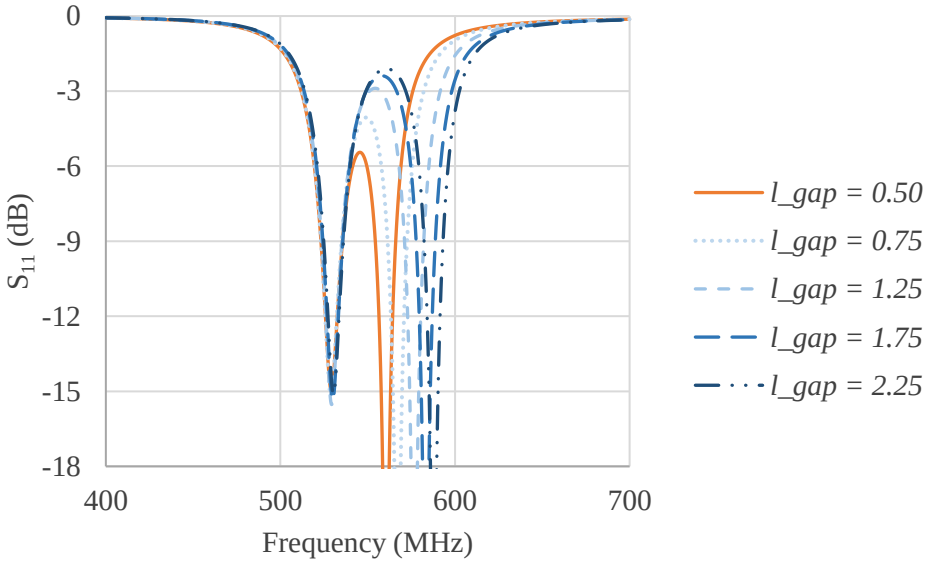

Figure 3-27. Simulated S_{11} for CDPIFA, parameterised *l_gap*. Legend shown to the right, units are mm. Original parameter combination shown in orange.

Figure 3-28 and Figure 3-29 compare the measured S_{11} characteristics of the fabricated prototypes shown in Figure 3-22 with simulations. Evidently, measured and simulated results are in good agreement. The slightly lower resonances observed for the measured results may be attributed to a slightly higher relative permittivity of substrate, and/or slight changes in the application

of the shorting pins and feed connectors in the prototypes versus the simulated models. Measurements show that the CDPIFA is resonant at 506 and 544 MHz, with a FBW_{-3dB} of 13%. For S_{11} below −3 dB, the antenna's *ka* value lies between 0.26 and 0.29.

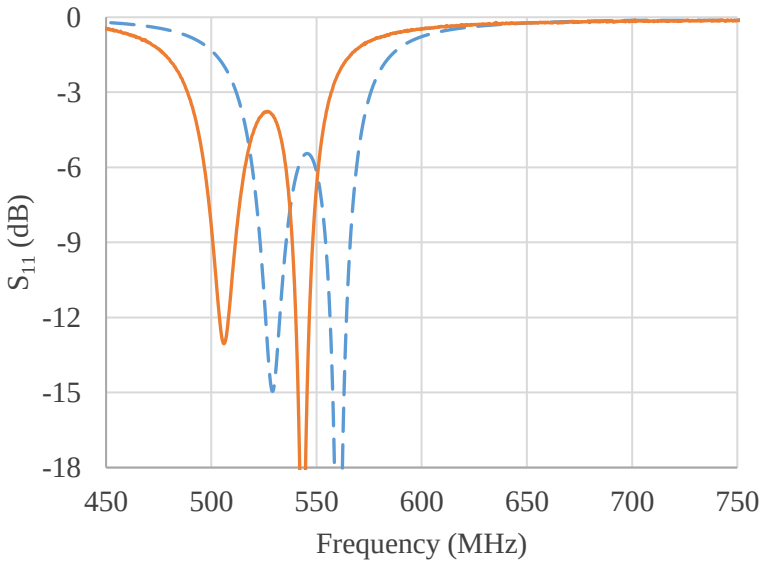

Figure 3-28. S_{11} results for CDPIFA; (orange) measured, (blue) simulated.

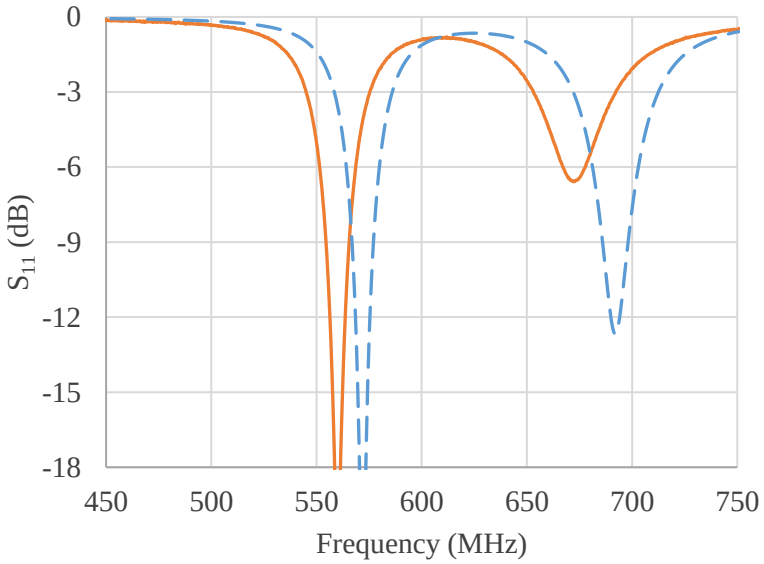

Figure 3-29. S_{11} results for $CPIFA_{2A}$; (orange) measured, (blue) simulated.

Measurements were taken in the anechoic chamber for the radiation patterns of these two antennas. Note that the available standard gain antenna, the HF906, does not operate at frequencies below 1 GHz; thus, a non-standard Yagi-Uda was used as the transmit antenna. As a result, peak normalized patterns are provided. The results are presented in Figure 3-30 and Figure 3-31 for the CDPIFA and $CPIFA_{2A}$, respectively. As expected from ESAs, the radiation patterns generally depict low directivity.

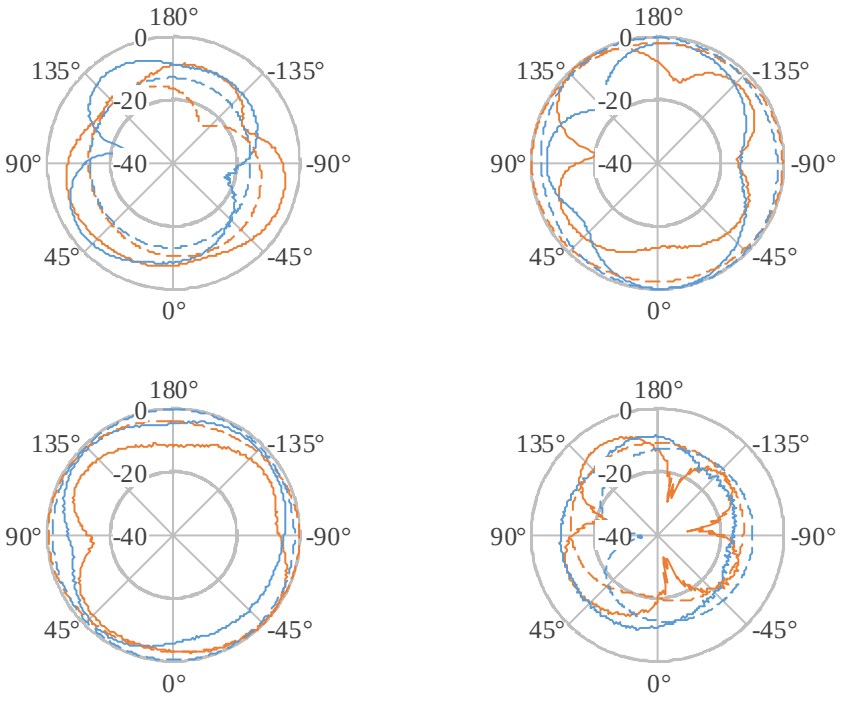

Figure 3-30. Peak normalized radiation pattern (dBi) for the CDPIFA; (top) 1st resonance, (bottom) 2nd resonance; (left) φ component, (right) θ component; (——) measured, (– –) simulated; (orange) azimuth plane, (blue) elevation plane.

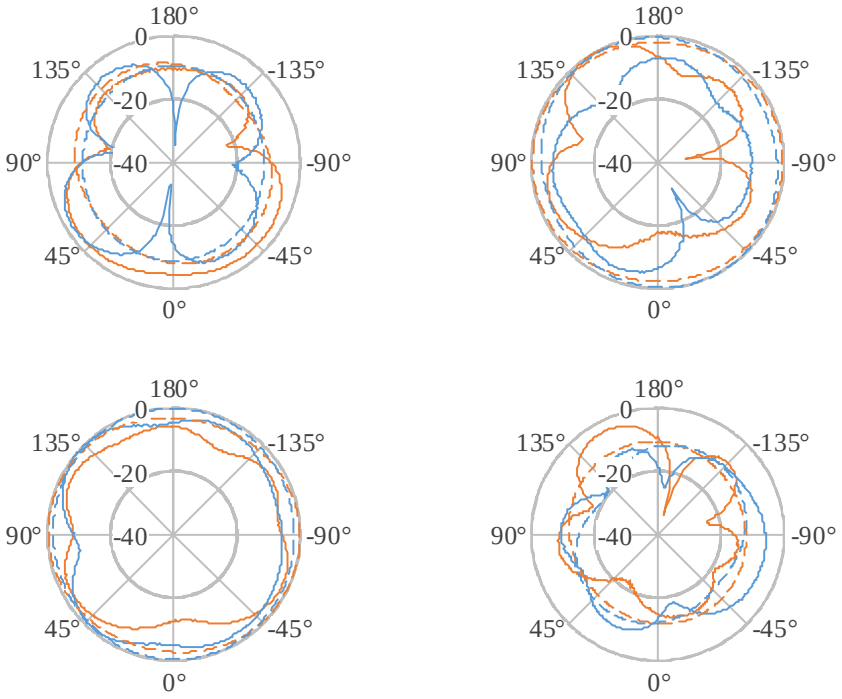

Figure 3-31. Peak normalized radiation pattern (dBi) for the CPIFA$_{2A}$; (top) 1st resonance, (bottom) 2nd resonance; (left) φ component, (right) θ component; (——) measured, (– –) simulated; (orange) azimuth plane, (blue) elevation plane.

It can be seen that for either antenna, the θ component is dominant in the first resonance, and the φ component is dominant in the second. This behaviour can be seen more clearly in Figure 3-32 and Figure 3-33 for the for the CDPIFA and CPIFA$_{2A}$, respectively, where the mean simulated gain is plotted as a function of frequency. The mean simulated gain for these antennas, with φ and θ components combined, is given in Table 3-2.

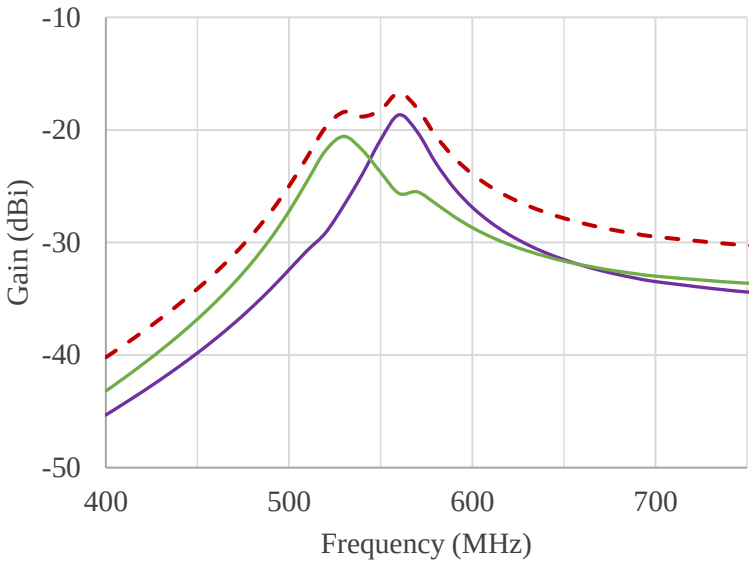

Figure 3-32. Mean* simulated gain for the CDPIFA as a function of frequency; (purple) φ component, (green) θ component, (red-dashed) combined total.

** mean gain computed from the absolute values over entire range of φ and θ.*

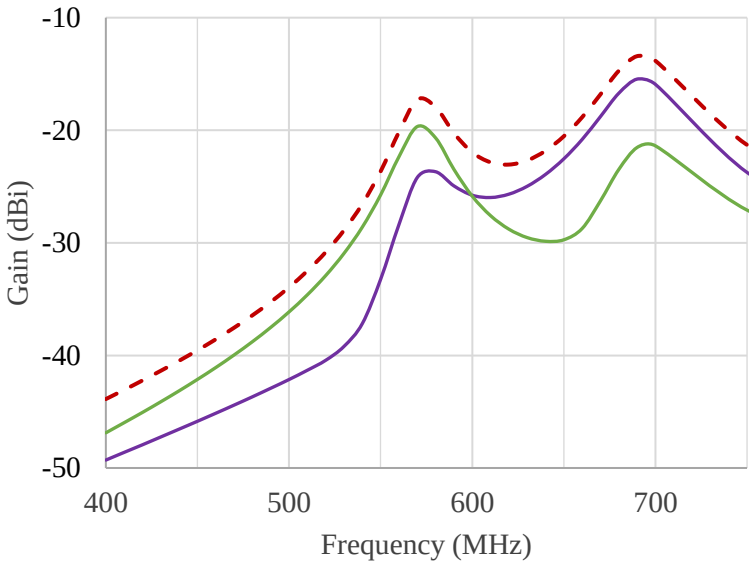

Figure 3-33. Mean* simulated gain for the $CPIFA_{2A}$ as a function of frequency; (purple) φ component, (green) θ component, (red-dashed) combined total.

** mean gain computed from the absolute values over entire range of φ and θ.*

Table 3-2. Comparison of simulated mean gain and radiation efficiency for the CDPIFA and $CPIFA_{2A}$.

	CDPIFA		$CPIFA_{2A}$	
	1st resonance	2nd resonance	1st resonance	2nd resonance
Simulated Resonance Frequency (MHz)	529	561	572	692
Measured Resonance Frequency (MHz)	506	544	560	674
Mean* simulated gain (dBi)	-18.4	-16.8	-17.4	-13.5
Simulated Radiation efficiency (%)	1.6	2.4	2.1	5.3

** mean gain computed from the absolute values over entire range of φ and θ.*

3.3.3. Comments

The CDPIFA presented and analysed here may be termed an *orthogonal-mode, dual-resonance* antenna, i.e. two modes of resonance which are orthogonally polarized. Thus, it can be utilised to transmit/receive two separate signals at either resonance, or the same signal with polarization-insensitivity (for example in applications where circular polarization is tolerated or even purposely utilized). Improvements to the bandwidth (as determined from the return loss) are possible by optimizing the structure such that the two resonances operate close together, which is an advantage over the IFA counterparts. A high miniaturization factor is achieved, with *ka* value between 0.26 and 0.29 over the antennas FBW_{-3dB} of 13%. However, the CDPIFA is a very inefficient antenna, greatly susceptible to losses in the substrate. This would limit practical application to only low-bitrate applications, for example, a signalling system on 'smart' streetlamps, or IoT enabled devices which have a low on-off time ratio. Whilst substrate losses can be reduced with the use of more expensive, low-loss substrates than FR4, this would also deteriorate the match of the antenna at impedance; further optimization of the antenna design is needed to raise the radiation resistance at its terminals. Note that the parameter Q_{ratio} is not directly

applicable to antennas exhibiting two resonances close together, as there is not yet a consensus within the antenna community regarding whether the relationships between *Q* and bandwidth hold for such behaviour [19].

3.4. Summary

This chapter introduced the novel, centrally populated digitated structure, applied to inverted-F and planar inverted-F antennas. This added structure may be intuitively likened to additional self-inductance and self-capacitance, a claim which is explored in greater detail in the following chapter.

First, a traditional, rectangular, IFA was compared to a compact, circular IFA. Results show that a reduction in *ka* of 1.32 to 0.53 is achievable at the expense of realized gain (which drops from 0.97 dBi to −5.22 dBi). A drop in the radiation efficiency is also observed, with measured values of 88% and 49% for the RIFA and CIFA, respectively.

Next, the digitated structure was introduced, and the resulting antenna is termed $CDIFA_{SMP}$. Designed for resonance at 2.4 GHz (measured resonance at 2.33 GHz), the antenna has a *ka* value of 0.44 (considering only the antenna), or 0.59 (taking into account the length of the SMP-SMA adaptor used for measurements). At this frequency, the radiating metallization has a maximum dimension of 13.6 mm (approximately a tenth of the operational wavelength). The small physical size of the antenna hampered precise gain and pattern measurements, though a reasonable similarity between simulations and measurements can be observed. An alternative metric, in the form of radiation efficiency was subsequently computed using the constant-loss-resistor Wheeler cap method, and found to be 39%. Using the measured FBW_{-3dB} of 15%, and substituting these values into Equation 1-4, the Q_{ratio} of this antenna is calculated to be 5.0.

Finally, a planar derivative of the same design, and optimized for dual-resonance behaviour is presented, termed the CDPIFA. A parameter study is reported, focusing on optimizing the resonance frequency of two distinct bands

of operation, with one each belonging to a horizontally and vertically polarized mode. This CDPIFA is shown to be extremely electrically small, with the lowest *ka* value at 0.26. However, in its current configuration, the antenna is highly lossy, and thereby only suited to a limited range of applications.

(This page intentionally left blank.)

CHAPTER 4

4. Detailed Analysis of Centrally Populated Digitated Structure

In this chapter, an abstraction of the digitated structure is presented. As described earlier, the digitated structure adds inductance and capacitance to the antenna. To offer a more intuitive explanation for this behaviour, it can be hypothesized that a single vertical and horizontal digit each can replace our more complex digitated structure, at the expense of less precise control over the input impedance.

4.1. The Simplified Digitated Structure

4.1.1. Circular Digitated Inverted-F Antenna Design

Figure 4-1 shows the front and back of the CAD model of the compact CIFA with an integrated abstracted digitated structure, termed here the circular, digitated, inverted-F antenna LC ($CDIFA_{LC}$); the LC term in subscript is inspired from the symbols for inductance and capacitance. As previously reported, this additional digitated structure adds inductance and capacitance to the antenna, which allows for frequency tuning, keeping the overall dimensions of the antenna constant. For this circular, planar antenna, the dimension *a* is also the radius, and equals 12 mm.

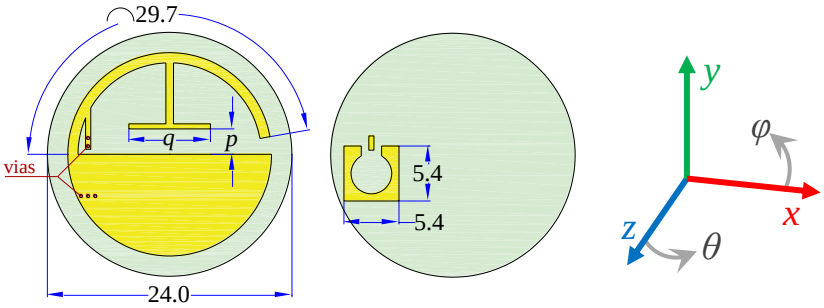

Figure 4-1. (*left*) Front and (*right*) back view of compact CDIFA$_{LC}$, showing the dimensions p and q which fully describe the simplified digitated structure. All dimensions are given in mm. Via locations labelled with red dots.

Note that the overall dimensions of this antenna are kept identical to the CIFA from Chapter 3 to allow for direct comparison; in fact, the principle of miniaturization expanded upon here may be applied at any frequency, within reason (i.e. substrate effects might vary too much at very high frequencies), as shown later in this chapter.

4.1.2. Equivalent Circuit

Figure 4-2 shows the equivalent circuit model of the CDIFA$_{LC}$. An additional series inductor, L_V, and a parallel capacitor, C_H, are added to the circuit shown in Figure 3-3 to model the effects of the digitated structure. This implies that additional capacitance and inductance can be introduced without altering the overall dimensions of the antenna, or even the relative lengths of the radiating arm and inductive loop shortening the arm to the ground plane. The remainder of this chapter details the effects on the antenna's performance of effectively varying these L_V and C_H components.

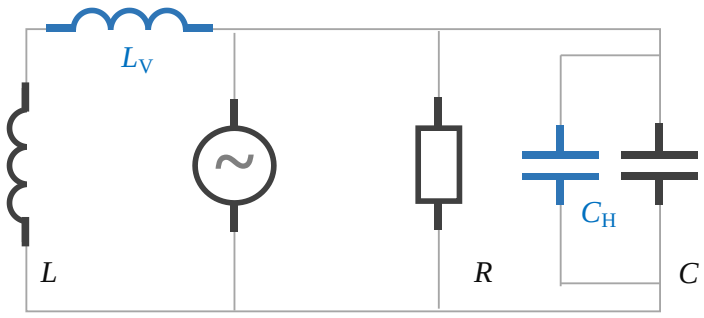

Figure 4-2. Equivalent circuit model for the CDIFA$_{LC}$. Addition of digitated structure increases the self-inductance and self-capacitance of the antenna.

4.2. Simulated Parametric Study

A parametric study was conducted using CST MWS, varying *p* and *q*, as labelled in Figure 4-1. For this study, the dimension *p* was varied between 0.25 and 2.25 mm at uniform intervals of 0.25 mm, and the dimension *q* was varied between 3 and 15 mm at uniform intervals of 2 mm. For these dimensions, the total range of frequencies covered is 1.2 to 2.0 GHz. Data from simulations was subsequently interpolated (using quadratic polynomial interpolation in MATLAB) to create a denser mesh.

Figure 4-3 shows a contour plot of the simulated resonance frequency overlaid on a 7 by 9 grid corresponding to the values of *p* and *q*. To a first-degree approximation, a smaller value of *p* corresponds to increased total inductance and capacitance (and hence a lower resonant frequency), whereas a larger value of *q* corresponds to increased capacitance (and thus a lower resonant frequency). Note that changes to *p* and *q*, by altering the current paths in the half-loops formed, also impact the self-inductance of the antenna. Results shown in Figure 4-3 agree well with the stated first-degree approximation.

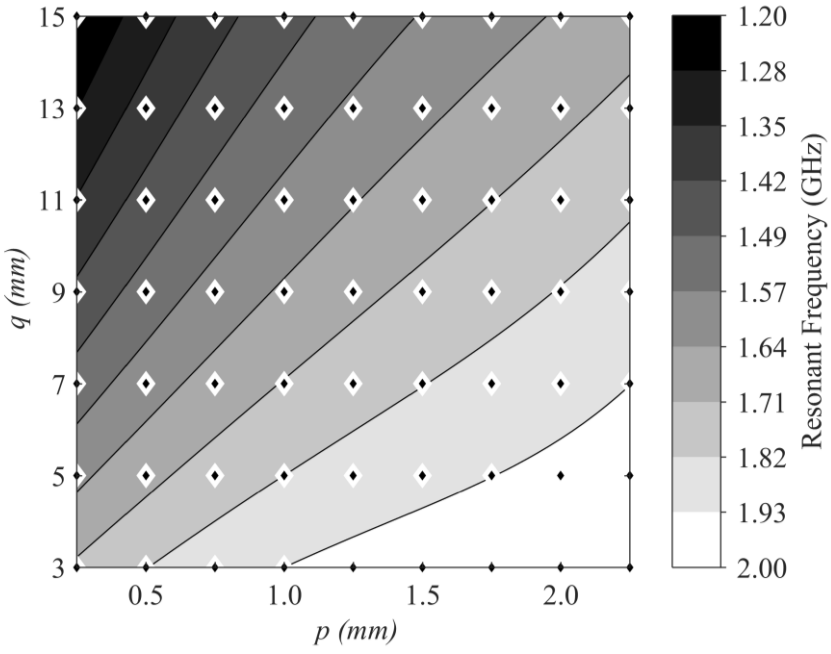

Figure 4-3. Simulated resonance frequency of CDIFA for varying dimensions of *p* and *q* in mm.

Figure 4-4, Figure 4-5, and Figure 4-6 show similar plots for the simulated *ka* values, radiation efficiency, and realized gain, respectively.

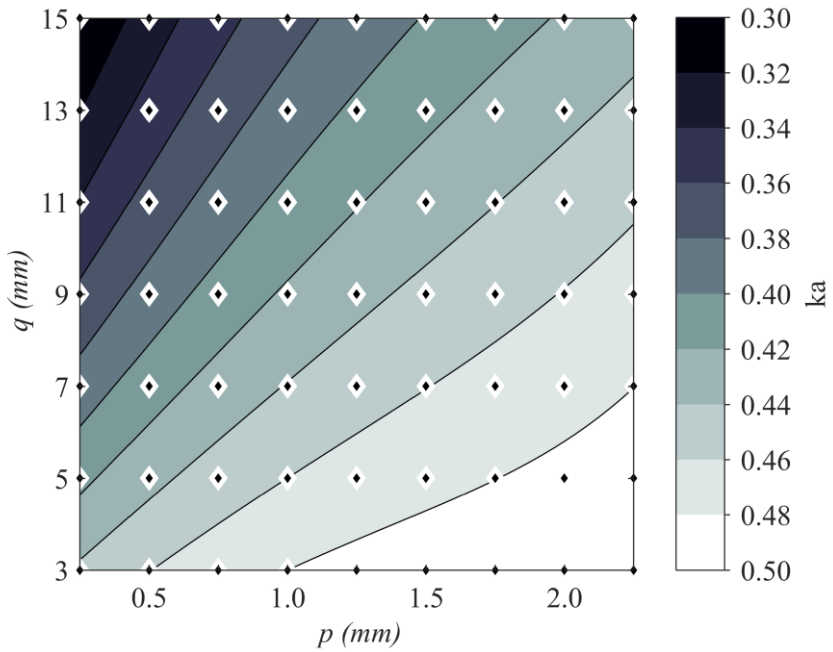

Figure 4-4. Simulated *ka* of CDIFA for varying dimensions of *p* and *q* in mm.

Since the overall dimension, and thus the dimension *a*, are constant, only the wavenumber *k* is affected by change in resonance frequency. This is reflected in the contours for *ka* being near-identical to those of resonant frequency. Figure 4-4 and Figure 4-5 reaffirm a key trade-off in ESA design, that *ka* is proportional to efficiency, so that a lower *ka* results in a lower radiation efficiency.

Note that for the parameter combination of p = 2.25 mm and q = 3 mm, the *ka* of the antenna is 0.50, radiation efficiency 58.0%, and mean gain −3.90 dBi, at a resonance frequency of 2.0 GHz. The lowest *ka* is achieved when p = 0.25 mm and q = 15 mm, and is 0.30 with the corresponding radiation efficiency 7.0%, and mean gain −12.90 dBi, at a resonance frequency of 1.2 GHz.

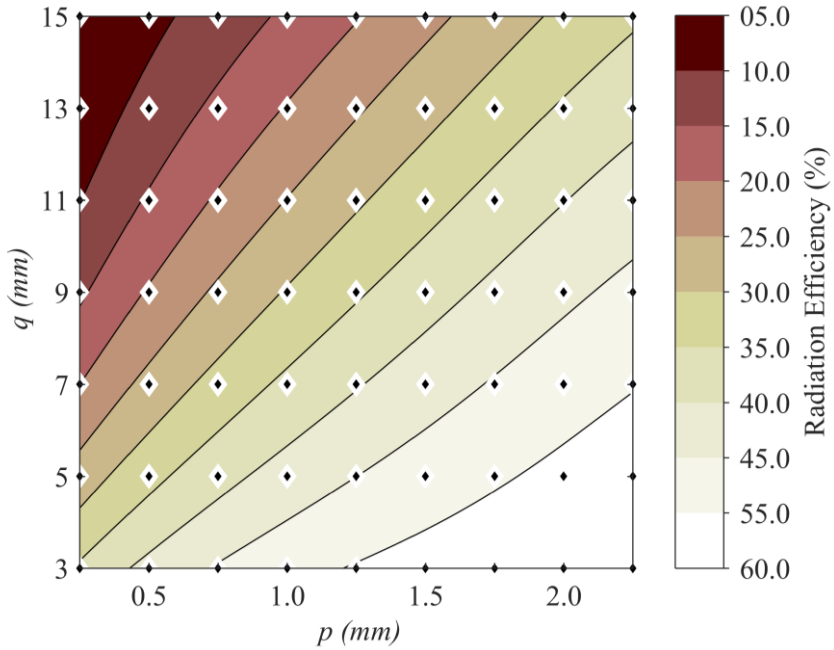

Figure 4-5. Simulated radiation efficiency of CDIFA for varying dimensions of *p* and *q* in mm.

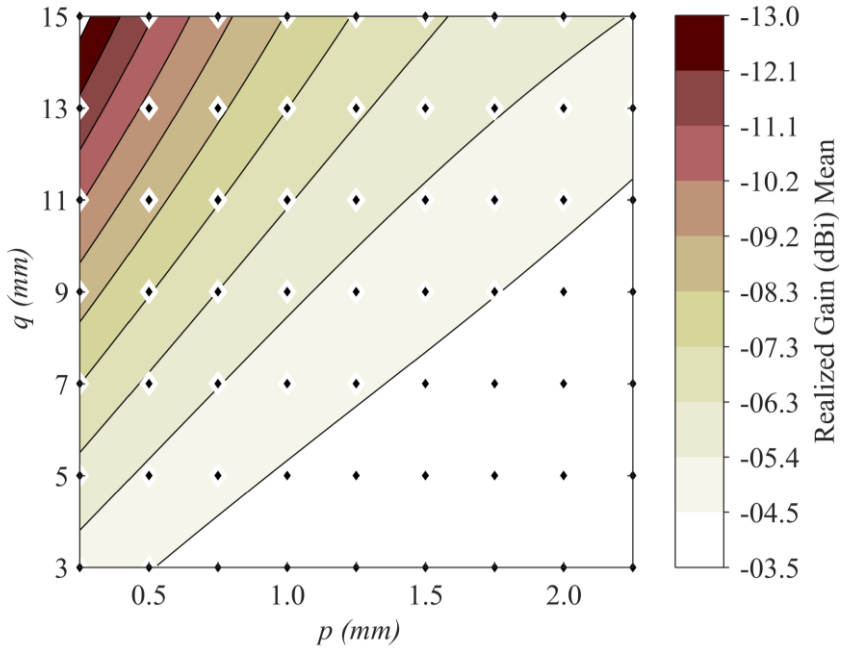

Figure 4-6. Simulated mean* realized gain of CDIFA for varying dimensions of *p* and *q* in mm.

** mean gain computed from the absolute values over entire range of φ and θ.*

These results show clearly the relationship between the dimensions of the centrally populated digits and the effects on antenna resonance due to the added

inductance and capacitance (as described at the top of this section), as well as the key trade-offs involved (i.e. miniaturization versus efficiency) The ensuing ‘design matrix’ allows the antenna designer to quickly estimate an ESA based on which of miniaturization or efficiency is more important for the desired design targets, as is demonstrated towards the end of this chapter.

4.3. Comparison with Measurements

In order to verify the simulation results presented, nine variations of the $CDIFA_{LC}$ were fabricated on an FR4 substrate. A photograph of these antennas is shown in Figure 4-7.

Figure 4-7. Photograph of the various fabricated $CDIFA_{LC}$ (*top; left to right*) $CDIFA_{L1C1}$, $CDIFA_{L1C2}$, $CDIFA_{L1C3}$; (*middle; left to right*) $CDIFA_{L2C1}$, $CDIFA_{L2C2}$, $CDIFA_{L2C3}$; (*bottom; left to right*) $CDIFA_{L3C1}$, $CDIFA_{L3C2}$, $CDIFA_{L3C3}$.

Measurements were taken for S_{11}, efficiency and realized gain. SMP-SMA adaptors were fashioned with ferrite sleeves covering semi-rigid coaxial cable. It was determined from measurements that the ferrite core covering helped eliminate leakage current on the surface of the semi-rigid cable, as seen from the convergence of simulations and measurements provided later in this section.

4.3.1. S_{11} and Fractional Bandwidth

Table 4-1 lists the parameter combinations used for the various $CDIFA_{LC}$, and compares their measured and simulated resonance frequencies. The FBW_{-3dB} for the antennas is given in Figure 4-8.

Table 4-1. Parameter combinations and resonant frequencies of the fabricated $CDIFA_{LC}$.

AUT	*p* (mm)	*q* (mm)	Resonant frequency (GHz) Simulated	Resonant frequency (GHz) Measured
$CDIFA_{L1C1}$	2.25	3.0	2.00	1.94
$CDIFA_{L1C2}$	2.25	9.0	1.93	1.88
$CDIFA_{L1C3}$	2.25	15.0	1.78	1.72
$CDIFA_{L2C1}$	1.25	3.0	1.88	1.81
$CDIFA_{L2C2}$	1.25	9.0	1.74	1.68
$CDIFA_{L2C3}$	1.25	15.0	1.45	1.39
$CDIFA_{L3C1}$	0.25	3.0	1.73	1.66
$CDIFA_{L3C2}$	0.25	9.0	1.54	1.49
$CDIFA_{L3C3}$	0.25	15.0	1.20	1.16

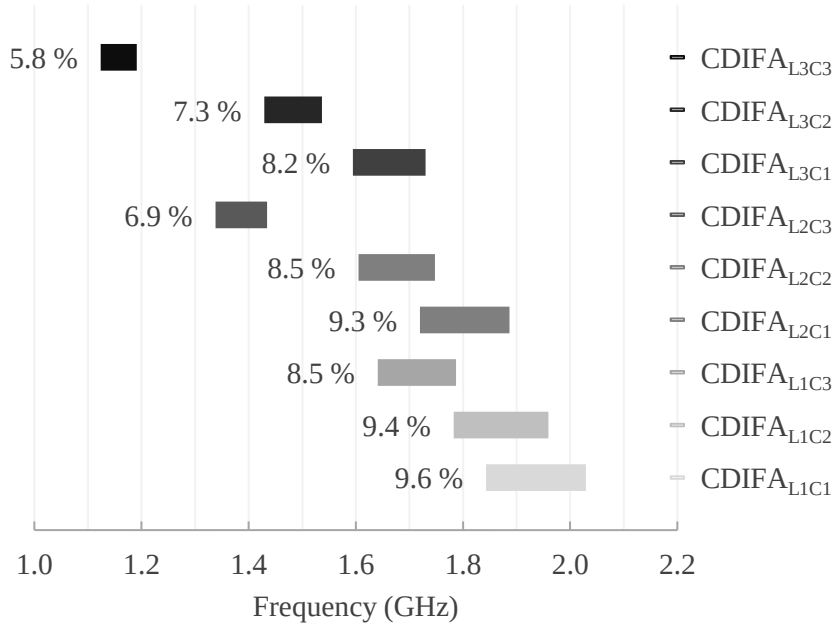

Figure 4-8. Range of frequencies where measured $S_{11} \leq -3$ dB for the various CDIFA$_{LC}$ as listed in Table 4-1. Corresponding FBW_{-3dB} is marked as percentage.

As with simulations, it is observed that an increase in the length of either the vertical or the horizontal digit results in a lower resonant frequency. On average, there is a 3.5% frequency shift in the measured resonant frequency compared to simulated results. As the frequency is consistently shifted down, it is likely an effect of the material properties of the substrate deviating, within tolerance, from the quoted value, $\varepsilon_r = 4.3$. Finally, it can be observed that the FBW_{-3dB} is reduced as the resonance frequency is lowered, implying an increased Q.

4.3.2. Radiation Efficiency Computation using Wheeler Cap

Radiation efficiency was computed using the constant-loss-resistor Wheeler cap method. Different sized Wheeler caps were used depending on the resonant frequency of the AUT, since it is a requirement of the calculation method that the inner walls of the cap are at-least a diameter (or side length) of λ/π at the frequency of interest. Measurements were taken for two orientations of the Wheeler cap boxes (placed in diamond and parallel alignments, with respect to the ground plate below). Figure 4-9 shows two different Wheeler cap boxes in these alignments.

Figure 4-9. Photographs of Wheeler cap measurement setup, (*left*) side length 10 cm in diamond alignment, (*right*) side length 5 cm in parallel alignment.

Efficiency measurements were repeated under various test setups to determine the precision of the computed results; results are presented here for the $CDIFA_{L1C1}$. Figure 4-10 displays the various adaptors used.

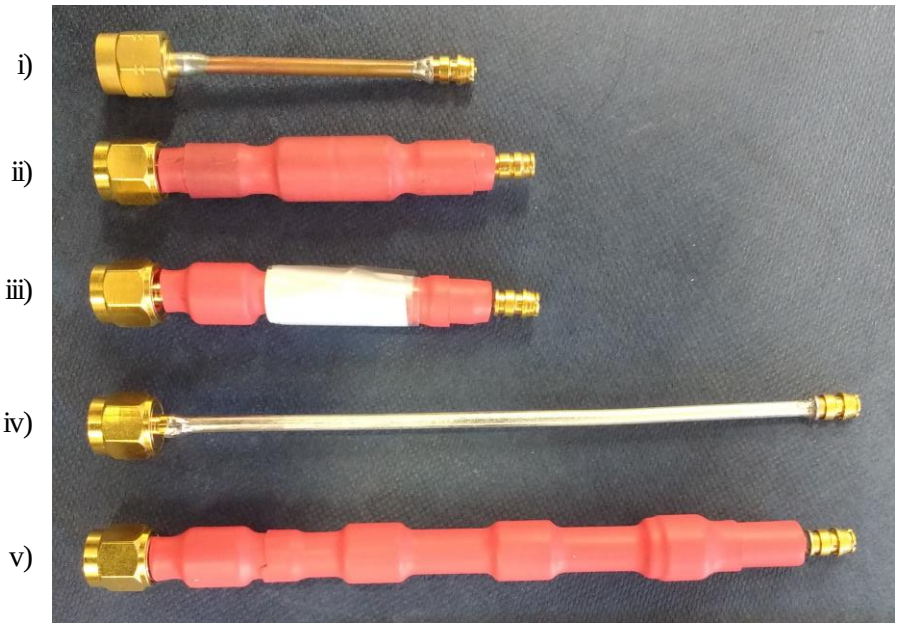

Figure 4-10. Different adaptors used to feed antennas for efficiency measurements: i) 4 cm bare, ii) 4 cm covered, iii) 4 cm covered, iv) 8 cm bare, v) 8 cm covered.

First, the $CDIFA_{L1C1}$ was placed using a straight terminated SMP-SMA adaptor of length 4 cm (tolerance ±0.4 cm), with the semi-rigid coaxial cable covered in ferrite sleeves. Measurements were taken for the antenna placed in a 5 cm side

length box placed in two different alignments (diamond and parallel). The antenna was resonant at 1.94 GHz; results are presented in Figure 4-11. It can be seen that the orientation of the Wheeler cap box has negligible effect on the computed radiation efficiency, indicating that the cap is able to adequately reflect the radiated fields originating from the antenna. A maximum error of 2 percentage points was obtained using similar measurements conducted for the other antennas.

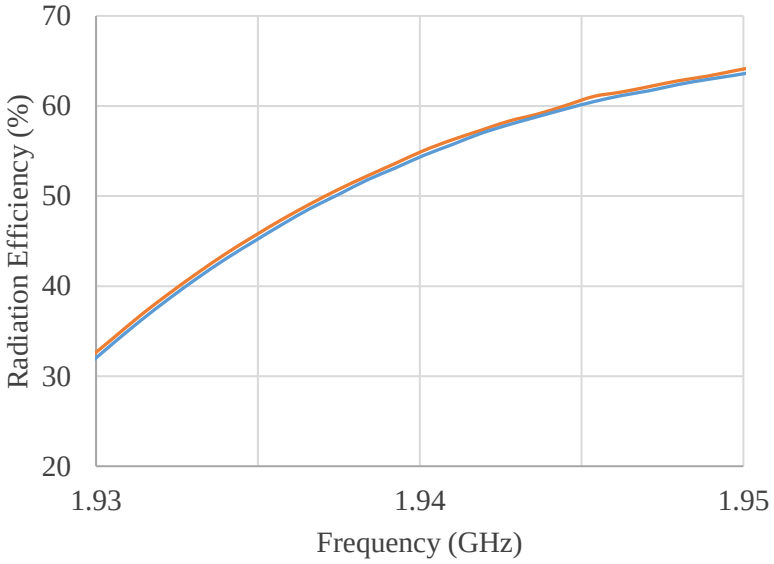

Figure 4-11. Measured radiation efficiency for the $CDIFA_{L1C1}$, using 4 cm adaptor; (orange) box parallel aligned, (blue) box diamond aligned. Plotted for ±10 MHz around resonance frequency.

Next, measurements for the $CDIFA_{L1C1}$ were repeated, placing the Wheeler cap box in parallel alignment with the ground plate, using three different SMP-SMA adaptors – all with ferrite sleeves covering the length of the coaxial cable. Two short adaptors of cable length 4 cm and one long adaptor of cable length 8 cm are used. A box of side length 5 cm was used for the two shorter adaptors, whilst a box of side length 10 cm was required to accommodate the larger adaptor. For all three adaptors, the antenna was resonant at 1.94 GHz; results are presented in Figure 4-12. The computed radiation efficiency at resonance is 56%, 54%, and 47%, respectively (maximum difference 9 percentage points); similar measurements were repeated for other antennas with the maximum error standing at 10 percentage points.

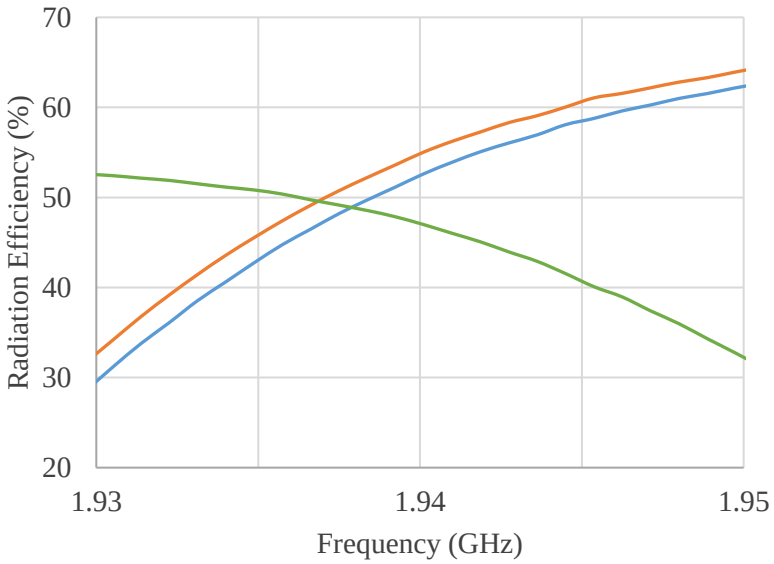

Figure 4-12. Measured radiation efficiency for the CDIFA$_{L1C1}$; (orange) 4 cm adaptor, (blue) other 4 cm adaptor, (green) 8 cm adaptor. Plotted for ±10 MHz around resonance frequency.

Next, measurements for the CDIFA$_{L1C1}$ were repeated using a 4 cm and 8 cm adaptor, both without the ferrite sleeve covering. The resonance frequency of the antenna was 1.97 GHz and 1.92 GHz, respectively; results are presented in Figure 4-13, along with the results computed using a 4 cm ferrite covered adaptor for comparison. The computed value of radiation efficiency is 88% and 82% for the 4 cm and 8 cm bare adaptors, respectively.

Figure 4-14 shows the simulated radiation efficiency and corresponding resonance frequency for the CDIFA$_{L1C1}$ using a bare coaxial cable to model the adaptors without ferrite sleeves; the variation in efficiency and resonant frequency over cable length is obvious. It can be seen that for a cable length of 4 cm, radiation efficiency is 84% (at corresponding resonance frequency of 1.95 GHz), and for a cable length of 8 cm, radiation efficiency is 70% (at corresponding resonance frequency of 2.00 GHz). Moreover, using a coaxial cable of length 0.2 cm, the simulated radiation efficiency is 51%, at a corresponding resonance frequency of 2 GHz – this result is much closer to computed efficiency values computed with SMP-SMA adaptors where the coaxial cable is covered with ferrite sleeves, and indeed close to simulated results where only the solder pad is modelled on the reverse of the antenna.

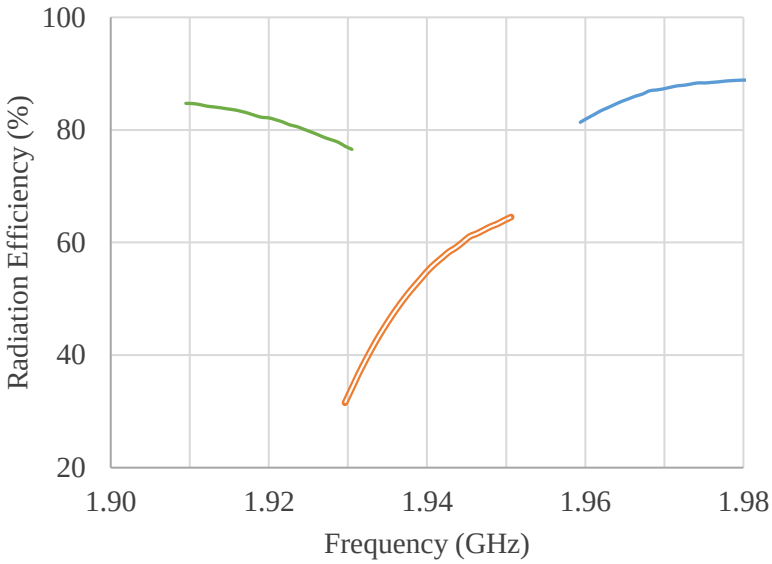

Figure 4-13. Measured radiation efficiency for the CDIFA$_{L1C1}$; (blue) 4 cm adaptor without ferrite sleeves, (green) 8 cm adaptor without ferrite sleeves; (orange) (===) 4 cm adaptor with ferrite sleeves. Plotted for ±10 MHz around resonance frequency.

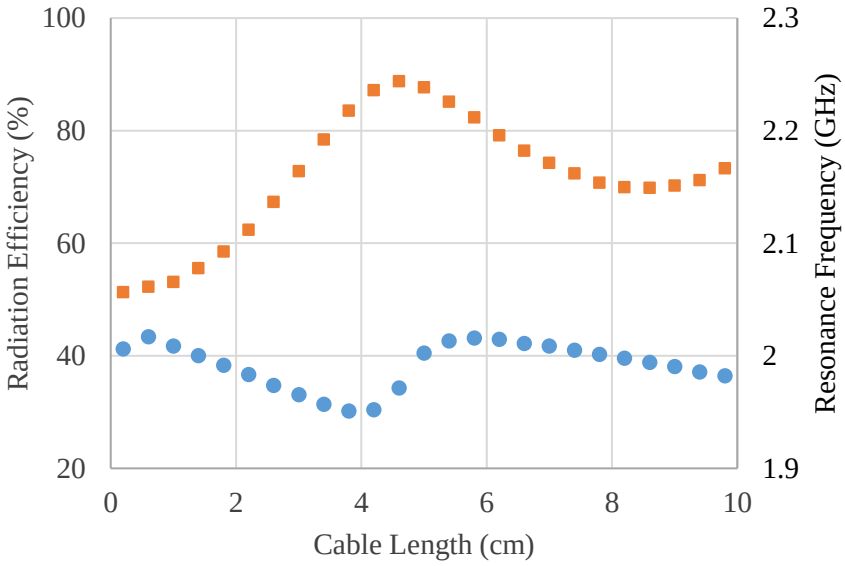

Figure 4-14. (orange-square) Simulated radiation efficiency, and (blue-circle) simulated resonance frequency for the CDIFA$_{L1C1}$, for varying lengths of coaxial cable (cm); simulation is carried out using bare coaxial cable only to model the adaptor – no ferrite sleeves are modelled.

Finally, measurements for the CDIFA$_{L1C1}$ were repeated using a 4 cm SMP-SMA adaptor (with coaxial cable covered in ferrite sleeves), where the SMP connector had a right-angle termination. This would establish measurement

precision dependent on the orientation of the AUT. The antenna was resonant at 1.94 GHz; radiation efficiency results are presented in Figure 4-15, along with those for the 4 cm straight SMP-SMA adaptor. It can be seen that radiation efficiency computed using the right-angle terminated adaptor is 54% (deviation of 2 percentage points from straight terminated adaptor). Similar measurements for other antennas revealed a maximum error of 6 percentage points between the efficiency values computed for straight and right-angle terminated adaptors.

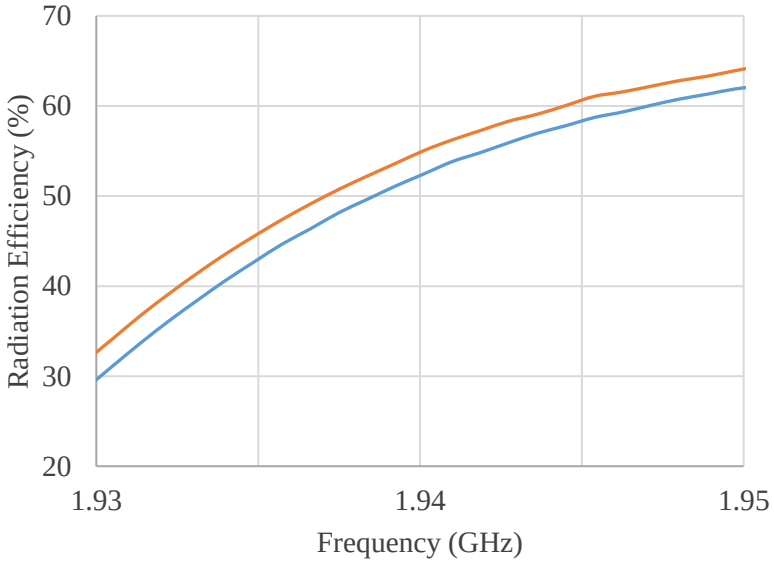

Figure 4-15. Measured radiation efficiency for the $CDIFA_{L1C1}$; (orange) 4 cm straight terminated adaptor, (blue) 4 cm right-angle terminated adaptor. Plotted for ±10 MHz around resonance frequency.

With a characterization of the precision for these efficiency measurements, results were computed for the nine $CDIFA_{LC}$, using the 4 cm straight terminated SMP-SMA adaptor (with semi-rigid coaxial cable covered in ferrite sleeves), and with the Wheeler cap placed parallel to the ground plate. Results are listed in Table 4-2. These results, together with the FBW_{-3dB} results from Figure 4-8, were substituted into Equation 1-4 to obtain the Q_{ratio} of the antennas. Table 4-3 lists the Q_{ratio} for each antenna, together with its Q and the corresponding lower limit. The Q_{ratio} for the antennas discussed here ranges from 3.5 to 11.2; as with the discussion of simulation results above, the bandwidth and efficiency of the antennas is reduced along with a reduction in their ka values.

Table 4-2. Radiation efficiency, η_r (%) of various AUTs at resonance.

AUT	Simulated η_r	Measured η_r
$CDIFA_{L1C1}$	58	56
$CDIFA_{L1C2}$	53	53
$CDIFA_{L1C3}$	40	34
$CDIFA_{L2C1}$	50	49
$CDIFA_{L2C2}$	38	38
$CDIFA_{L2C3}$	16	15
$CDIFA_{L3C1}$	37	35
$CDIFA_{L3C2}$	22	21
$CDIFA_{L3C3}$	07	07

Table 4-3. Q, Q_{lb} and Q_{ratio} of various AUTs at resonance.

AUT	Q	$Q_{lb\text{-}Chu}$	Q_{ratio}
$CDIFA_{L1C1}$	20.8	6.0	3.5
$CDIFA_{L1C2}$	21.2	6.1	3.5
$CDIFA_{L1C3}$	23.5	5.0	4.7
$CDIFA_{L2C1}$	21.6	6.3	3.4
$CDIFA_{L2C2}$	23.6	5.9	4.0
$CDIFA_{L2C3}$	28.9	3.9	7.3
$CDIFA_{L3C1}$	24.6	5.7	4.3
$CDIFA_{L3C2}$	27.6	4.6	6.1
$CDIFA_{L3C3}$	34.4	3.1	11.2

4.3.3. Realized Gain and Radiation Patterns

Lastly, results from gain measurements are presented for three selected antennas, namely the, $CDIFA_{L1C1}$ (Figure 4-17: φ component; Figure 4-18: θ

component), $CDIFA_{L2C2}$ (Figure 4-19: φ component; Figure 4-20: θ component), and $CDIFA_{L3C3}$ (Figure 4-21: φ component; Figure 4-22: θ component). The measurements were carried out in an anechoic chamber using NSI 800F-10 measurement setup with an Agilent E5071B network analyzer; Figure 4-16 shows an AUT mounted in the chamber. The gain was computed using the gain transfer method with a Rhode & Schwartz HF906 horn antenna as the reference.

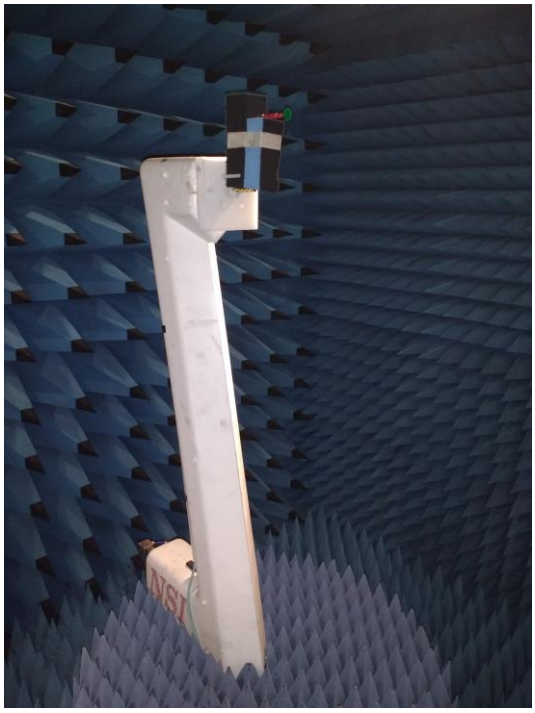

Figure 4-16. Photograph of AUT mounted on NSI 800F-10 Z-arm inside anechoic chamber.

Measured and simulated results show good agreement, especially in the φ component; however, measured results for the θ component are consistently higher than simulated predictions. This is in part due to the sensitivity of the measurement setup, and in part due to the amplified effects of artefacts in the measurement of these physically and electrically small antennas. Note in particular the undulating pattern for the $CDIFA_{L3C3}$, where external effects are felt the strongest due to a very small *ka* value of 0.29. Polarization is typically not an important consideration for ESAs, due mainly to the nature of applications they are commonly found in, though detailed polarization measurements can be identified as an area of continued research.

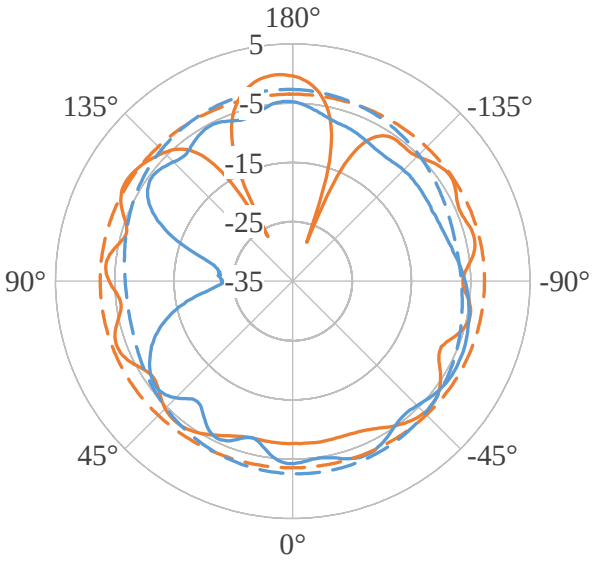

Figure 4-17. Realized gain (dBi) for the $CDIFA_{L1C1}$ at 1.94 GHz; (——) measured, (– –) simulated; (orange) azimuth plane, (blue) elevation plane. φ component only.

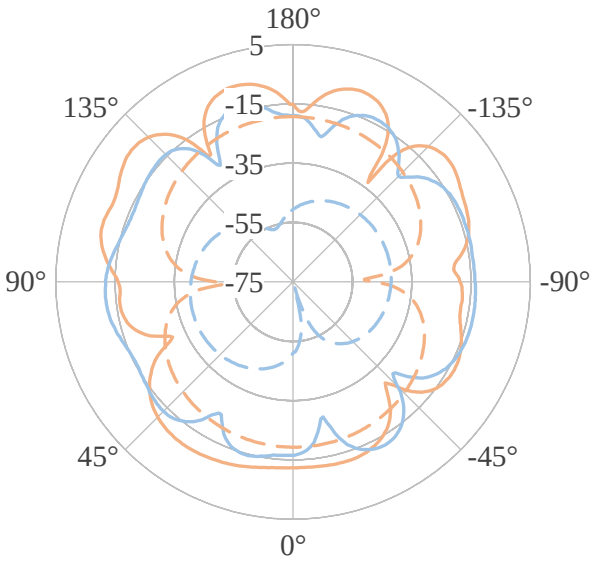

Figure 4-18. Realized gain (dBi) for the $CDIFA_{L1C1}$ at 1.94 GHz; (——) measured, (– –) simulated; (light-orange) azimuth plane, (light-blue) elevation plane. θ component only.

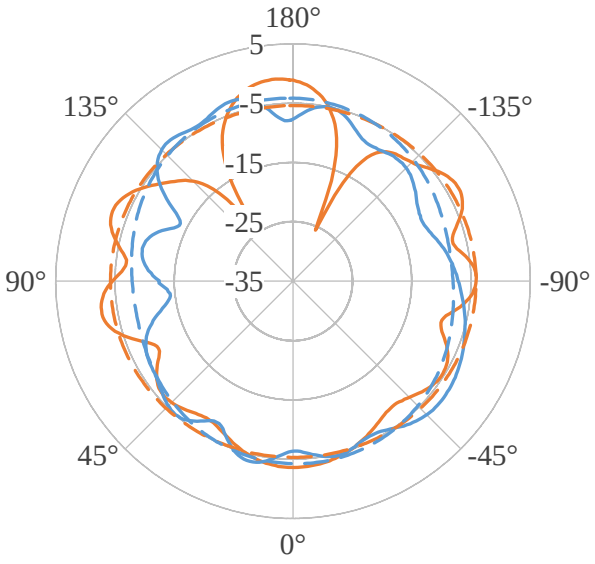

Figure 4-19. Realized gain (dBi) for the $CDIFA_{L2C2}$ at 1.68 GHz; (——) measured, (– –) simulated; (orange) azimuth plane, (blue) elevation plane. φ component only.

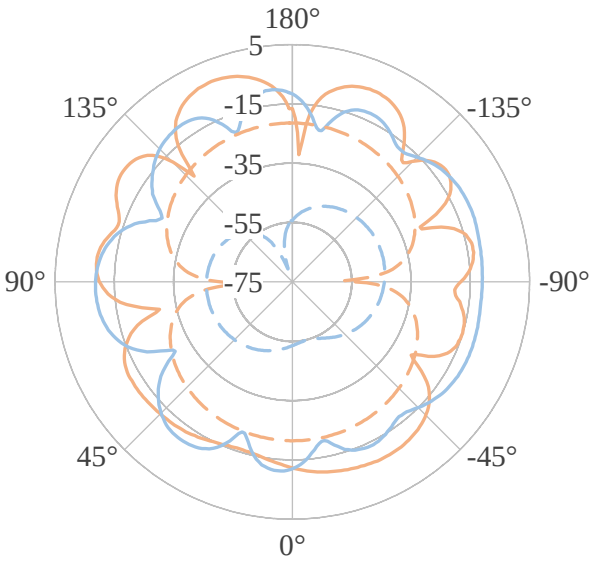

Figure 4-20. Realized gain (dBi) for the $CDIFA_{L2C2}$ at 1.68 GHz; (——) measured, (– –) simulated; (light-orange) azimuth plane, (light-blue) elevation plane. θ component only.

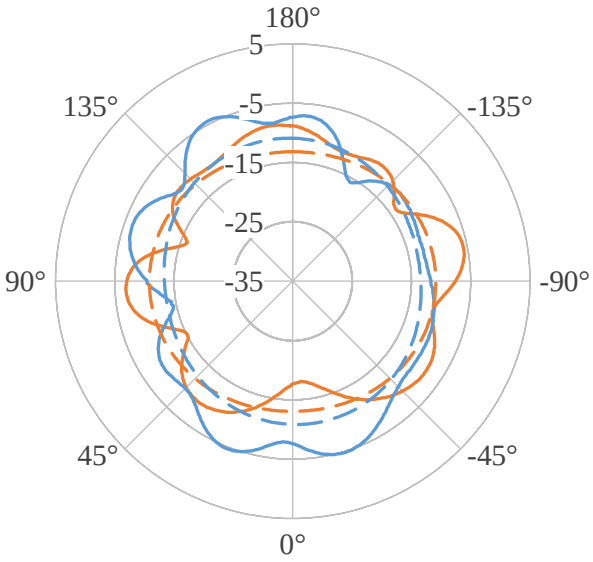

Figure 4-21. Realized gain (dBi) for the $CDIFA_{L3C3}$ at 1.16 GHz; (——) measured, (– –) simulated; (orange) azimuth plane, (blue) elevation plane. φ component only.

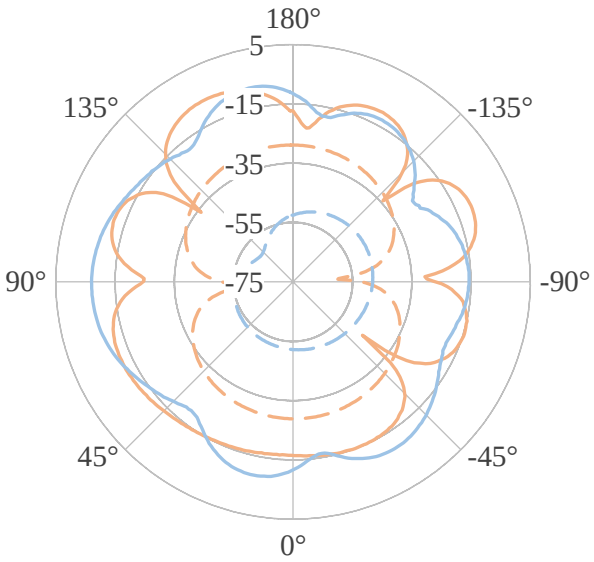

Figure 4-22. Realized gain (dBi) for the $CDIFA_{L3C3}$ at 1.16 GHz; (——) measured, (– –) simulated; (light-orange) azimuth plane, (light-blue) elevation plane. θ component only.

From the gain patterns, it can be seen that the primary polarization lies in the φ component; the combined average forward measured gain (±90°) for the φ component is −6.32 dBi, −5.99 dBi, and −10.08 dBi for the $CDIFA_{L1C1}$, $CDIFA_{L2C2}$, and $CDIFA_{L3C3}$, respectively. (Note that there is a more pronounced

dip in measured gain in the elevation plane for the $CDIFA_{L1C1}$ around 90° relative to the $CDIFA_{L2C2}$, which is likely due to increased measurement artefacts; hence the lower combined average value). Table 4-4 summarizes the average forward measured gain (±90°) for these antennas, for each of φ and θ components.

Table 4-4. Summary of average forward measured gain (±90°) for the $CDIFA_{L1C1}$, $CDIFA_{L2C2}$, and $CDIFA_{L3C3}$. All values are presented in dBi.

	$CDIFA_{L1C1}$		$CDIFA_{L2C2}$		$CDIFA_{L3C3}$	
	φ	θ	φ	θ	φ	θ
Measured azimuth plane	-5.79	-13.06	-5.91	-14.17	-11.45	-16.59
Simulated azimuth plane	-3.00	-25.25	-4.70	-27.47	-11.87	-34.66
Measured elevation plane	-6.85	-14.09	-6.07	-13.94	-8.70	-13.14
Simulated elevation plane	-4.48	-46.14	-5.93	-49.05	-12.03	-51.93

4.4. Antenna Synthesis Examples

Having established the corroboration of simulation results with measurements, the results of the parametric study can be utilized to obtain a good first estimate for ESAs based on the centrally populated digit design principle, without the need for time and resource intensive computational modelling. Depending on which of miniaturization or efficiency is the primary goal, the contour plots in Figure 4-4 (ka vs p and q) and Figure 4-5 (η_r vs p and q) can be used to pick out the necessary dimensions of the central digits, without altering the proportions of any other parameters in the antenna geometry. The contour plot shown in Figure 4-3 can subsequently be used to obtain a suitable scaling factor for the synthesized antenna model.

To illustrate this design guideline, ESAs based on the geometry of the $CDIFA_{LC}$ are synthesized for operation at 433 MHz (extreme miniaturization), 2.4 GHz (maximum efficiency), and 5.9 GHz (at least 40% efficiency). Simulated results for S_{11} and radiation efficiency are provided in Figure 4-23.

To synthesize an ESA operating at 433 MHz, and with the lowest *ka*, we pick out the values of 0.25 mm and 15 mm for *p* and *q* respectively, using Figure 4-4, as these dimensions correspond to the highest degree of miniaturization. Then, using Figure 4-3, we can see that this antenna would resonate around 1.2 GHz. Thus, for operation at 433 MHz, the entire antenna is scaled by a factor of 2.8.

To synthesize an ESA operating at 2.4 GHz, and with the highest radiation efficiency, we pick out the values of 2.25 mm and 3 mm for *p* and *q* respectively, using Figure 4-5, as these dimensions correspond to the highest efficiency. Then, using Figure 4-3, we can see that this antenna would resonate around 2.0 GHz. Thus, for operation at 2.4 GHz, the entire antenna is scaled by a factor of 0.83.

A number of possible combinations of *p* and *q* may be employed to synthesize an ESA operating at 5.9 GHz with radiation efficiency at least 40%. Assuming that miniaturization is a secondary aim, we pick out the values of 1.5 mm and 9 mm for *p* and *q* respectively, using Figure 4-5, which correspond to approximately 40% efficiency. Again, using Figure 4-3, we can see that the resonance frequency of the antenna is approximately 1.8 GHz. Thus, for operation at 5.9 GHz, the entire antenna is scaled by a factor of 0.30.

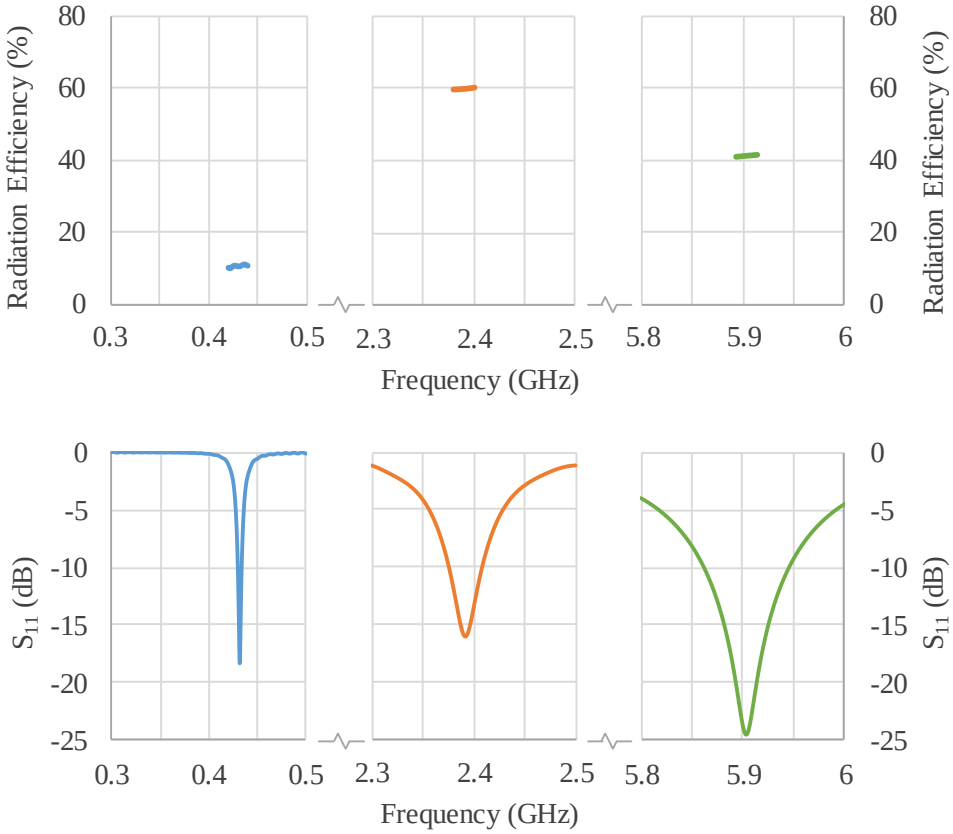

Figure 4-23. Simulated (*top*) radiation efficiency and (*bottom*) S_{11} for the (blue) $CDIFA_{433MHz}$, (orange) $CDIFA_{2.4GHz}$, and (green) $CDIFA_{5.9GHz}$.

4.5. Comparison with selected ESAs from Literature

Figure 4-24 shows a scatter plot of Q_{ratio} versus *ka* for the $CDIFA_{SMP}$ (presented in Chapter 3), and nine variants of the $CDIFA_{LC}$ (presented in Chapter 4), along with selected antennas from the literature review. (For a similar plot with data points for antennas from the literature review labelled with their respective reference numbers, see Figure 1-3.) In these terms, it can be seen that the single resonance antennas presented in this Thesis are comparable to various other published antennas (which include planar as well as 3D variants). There is a general trend of increasing Q_{ratio} as *ka* diminishes, which highlights the difficulty in sustaining comparable performance in ESAs as their electrical size is reduced. In the figure presented, the only antenna to buck this trend with measured results is the perfectly spherical 3D wire-grid antenna by Kim [65].

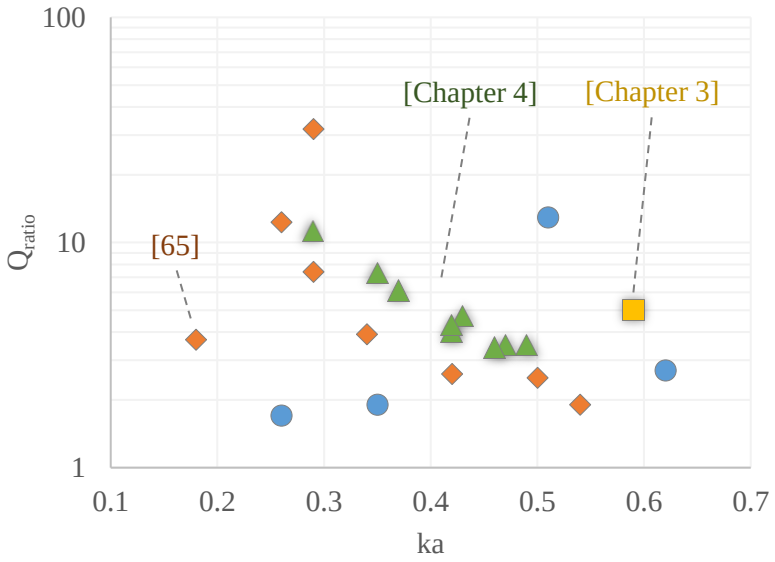

Figure 4-24. Q_{ratio} vs *ka* value scatter plot for $CDIFA_{SMP}$ (yellow-square) and $CDIFA_{LC}$ (green-triangle), with selected antennas from literature review for comparison (c.f. Figure 1-3).

From the previous discourse, it is clearly established that measured results for radiation efficiency line up well with simulation results where only the back panel is modelled, implying that the SMP-SMA adaptor cables do not need to be incorporated when computing the *ka* and subsequently the Q_{ratio} for these antennas. However, it should be noted that the measured results present an exaggerated FBW, as compared to simulations (computed values show that simulated FBW_{-3dB} ranges between 50 – 60 % of the measured values, as seen in Figure 4-25). A likely cause for this increased measured bandwidth is that while the modified adaptors supress leakage current and thus wayward radiation, they add some loss to the antenna.

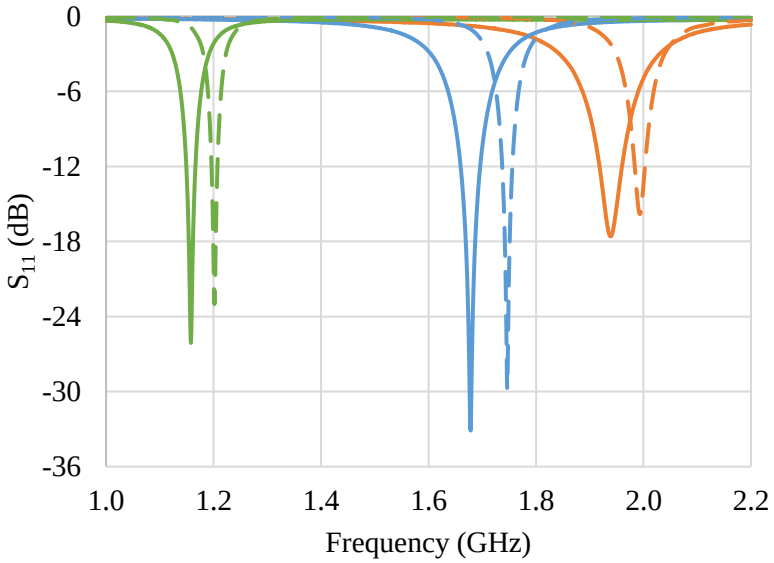

Figure 4-25. (——) Measured and (– –) simulated S_{11} results for the $CDIFA_{L1C1}$ (orange), $CDIFA_{L2C2}$ (blue), $CDIFA_{L3C3}$ (green).

Computations taking into account this narrower bandwidth would thus result in a more accurate depiction of the antenna's *Q*. Subsequently, Q_{ratio} values are computed using the simulation results for bandwidth and efficiency, and plotted in Figure 4-26. As expected, *ka* values are approximately the same as before, with an increase in the computed Q_{ratio}. Note that the data point for the $CDIFA_{SMP}$ (Chapter 3) incorporates the overall dimension of the antenna (including the commercially available adaptor used) as well as the increased bandwidth.

As recommended in the future work section in Chapter 6, the data presented here may be refined with opto-electric measurement equipment so that only the antenna itself is the device under test. Additionally, similar antennas may be designed at a lower resonance frequency to facilitate the use of regular SMA connectors, such that the calibrated frame of reference for VNA measurements is moved closer to the actual antenna structure.

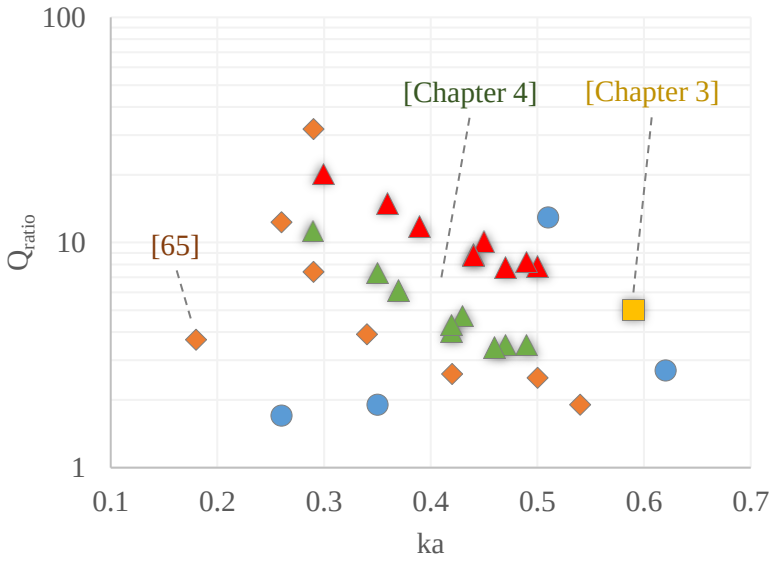

Figure 4-26. Q_{ratio} vs ka value scatter plot for $CDIFA_{LC}$ computed using (green-triangle) measured and (red-triangle) simulated FBW_{-3dB} and η_r, with selected antennas from literature review for comparison (c.f. Figure 1-3).

4.6. Summary

This chapter reviewed in detail a new design approach to the optimization of electrically small antennas. The novel, centrally populated digitated structure introduced in the previous chapter is abstracted to a simpler structure consisting of a single vertical and horizontal digit, modelled as an additional series inductor and parallel capacitor added to the equivalent circuit of a traditional IFA.

A thorough parametric study of the resultant $CDIFA_{LC}$ confirms that the key optimization parameters can be distilled to the lengths of the two digits, which act as added self-capacitance and self-inductance. The results of the parameter study produced a 'design matrix', which allows the antenna designer to swiftly decide on the geometrical proportions depending on which of miniaturization or efficiency is the desired goal at a particular frequency of operation. Thus, a good first estimate for the digitated IFA can be obtained without the need for complex computational simulations.

As pointed out earlier, further efficiency and bandwidth gains can be made using volumetric designs [11, 19, 20]. However, the low profile of planar antennas

translates to high versatility, with narrowband ESAs (such as those discussed in this chapter) employed in low data rate applications – from the ever-popular ‘smart’ consumer electronics to telemetry uses in industries such as telecommunications, defence, and healthcare.

Measurement accuracy for the results presented in this section was improved over previous sections with the use of custom made SMP-SMA adaptors that comprise a semi-rigid coaxial interconnect surrounded with ferrite loops to suppress leakage currents. To further alienate the unwanted effects of current-carrying conductors in the vicinity of the antennas, optical interconnects may be used (explained in Chapter 6). Finally, a natural continuation of the research presented thus far, which has focused on antenna design, would be to extend the design methodology to other types of antennas, such as loops, slots, etc.

(This page intentionally left blank.)

CHAPTER 5

5. Investigation of Fabrication Techniques

This chapter discusses three types of antennas which were fabricated in-house as part of an investigation into the prototyping and measurement of inherently 3D antenna designs. For a background on the fabrication processes discussed here, see Chapter 2.

The first antenna presented is a planar meanderline antenna, fabricated using photolithography on a glass substrate. The exercise was conducted primarily as a pre-cursor to holographic photolithography, which was later supplanted with a greater focus on AM fabrication processes. This was due, in part, to unforeseen limitations in equipment and personnel during the course of the research, but primarily due to the opportunity of pioneering measured results for metallic 3D printed antennas using AM. As such, the next antenna presented is a dome antenna, based on the design proposed in [72], modified for dual-band behaviour, and fabricated by 'damascening' [107] conductive ink onto a 3D printed substrate. The substrate is a hemisphere printed out of ABS plastic, with indented grooves in place of a conductive radiating structure; these grooves were later filled in with conductive silver paint.

The practical experience gained from these two early ventures was carried forward into the design, fabrication, and measurement of the planar antennas presented in preceding chapters as well as the metallic 3D printed antennas presented in the last section of this chapter. These were fabricated using SEBM PBF-AM, which is one of the few AM technologies able to directly print metals [24, 94-96]. Spherical, part-spherical, and flat variants of the same conductor

profile were fabricated to corroborate simulation predictions; measured results for matching, radiation efficiency, and gain are presented. The metallic conductors are printed from a titanium alloy, and rested on top of a hollow plastic substrate printed out of nylon with very thin walls, acting primarily as support for the metallized structure.

5.1. Meanderline Antenna

As previously mentioned, introducing bends to the radiating arm of a monopole to achieve a meanderline geometry is useful in reducing the overall electrical size of the antenna. For the printed monopole variation as discussed here, the absence of a large ground plane is advantageous in integrated applications where the availability of space is limited.

5.1.1. Antenna Optimization

A compact, planar meanderline antenna (MLA) was designed on a 1.2 mm thick glass substrate (ε_r = 4.8, tanδ = 0.0054) for resonance at 2.45 GHz, with largest dimension equal to 0.31λ. (The antenna design is based on an MLA on an FR4 dielectric substrate [108].) Glass was chosen as the substrate material since it can be subjected to processes such as vacuum deposition and withstand chemical etchants, and may be blown into spherical shapes for experimentation with holographic photolithography. Figure 5-1 shows the front schematic of the antenna. The radiating element consists of seven half-turns expanding outwards, progressing along the *y*-axis, and is fed by a tapered microstrip line; a partial ground plane covers the reverse of the substrate.

Table 5-1 lists the optimized parameter values for resonance at 2.45 GHz. The total track length of the radiating section is 69 mm, fitted inside an area of size 9.6 mm by 36 mm. A gentle taper is used to better match the impedance of the feed line to that of the radiating section. Considering the total size of the antenna, the parameter *a* equals 23 mm; at its simulated resonance frequency of 2.43 GHz, its *ka* value is 1.2. The antenna is thus on the border of being categorized as an ESA.

Table 5-1. Parameter list for optimized MLA.

Parameter	Code	Value (mm)
Width of substrate	-	25.4
Height of substrate	-	38.1
Height of ground plane	h_{ground}	25.0
Length of taper	l_{taper}	21.0
Width of taper at termination	w_{taper}	0.50
Width of radiator track	w_{track}	1.00
Separation between turns	s_{track}	0.80
Increment per half turn of loop	i_{loop}	0.25
Total width of loop	w_{loop}	9.50
Length of final section	-	4.00

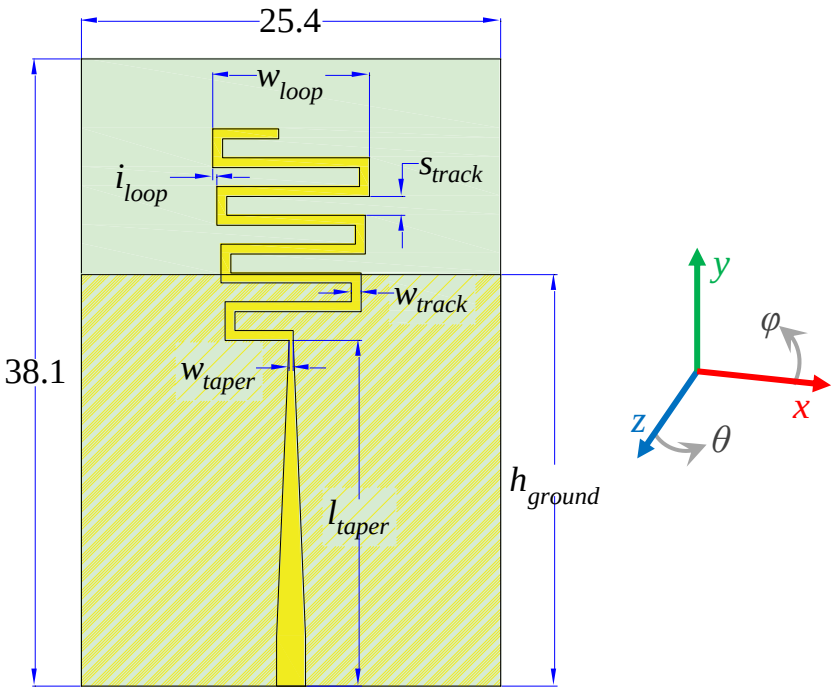

Figure 5-1. Front view of MLA model, (yellow) metal, (teal) substrate; ground plane extents are shown with a patterned fill.

A parametric study on the labelled parameters was undertaken to determine the effects on antenna performance. Key parameters which affect the resonance frequency of the antenna are h_{ground}, s_{track}, i_{loop}, and w_{loop}; parametric results for varying values are provided in Figure 5-2, Figure 5-3, Figure 5-4, and Figure

5-5, respectively. The performance characteristics of the MLA are a function of the antenna's current distribution as well as the induced current distribution on the finite ground plane; thus the size of the ground plane can be varied to achieve the best possible match at the desired frequency. Other parameters which affect the resonance frequency vary the overall length of the conductor. The width of the taper at the feed point and where it meets the radiating structure can be appropriately adjusted to achieve the best impedance match. The width of the tracks in the radiating section, keeping all other parameters constant, does not have a significant effect on the resonance frequency, but affects the input impedance of the radiating structure.

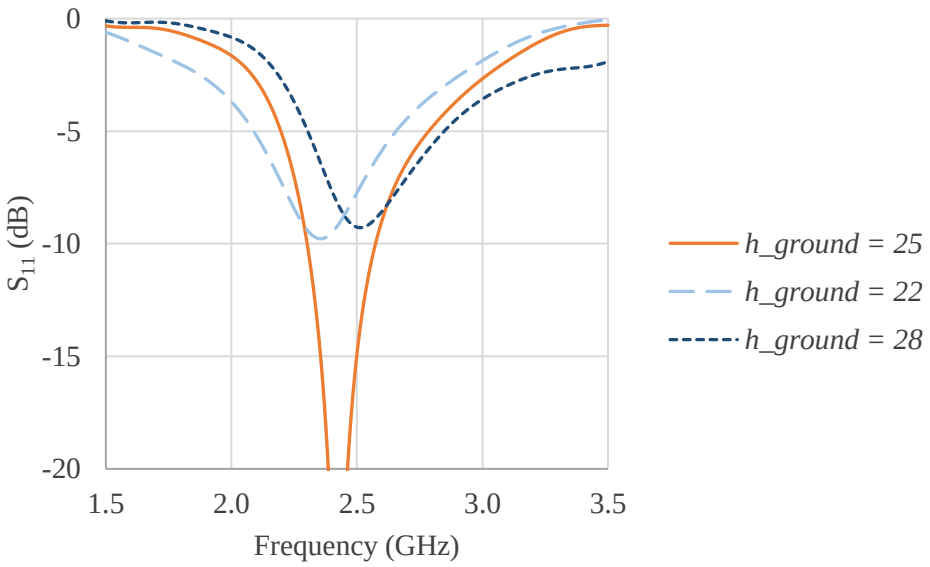

Figure 5-2. Simulated S_{11} for MLA, parameterised h_{ground}. Legend shown to the right, units are mm. Original parameter combination shown in orange.

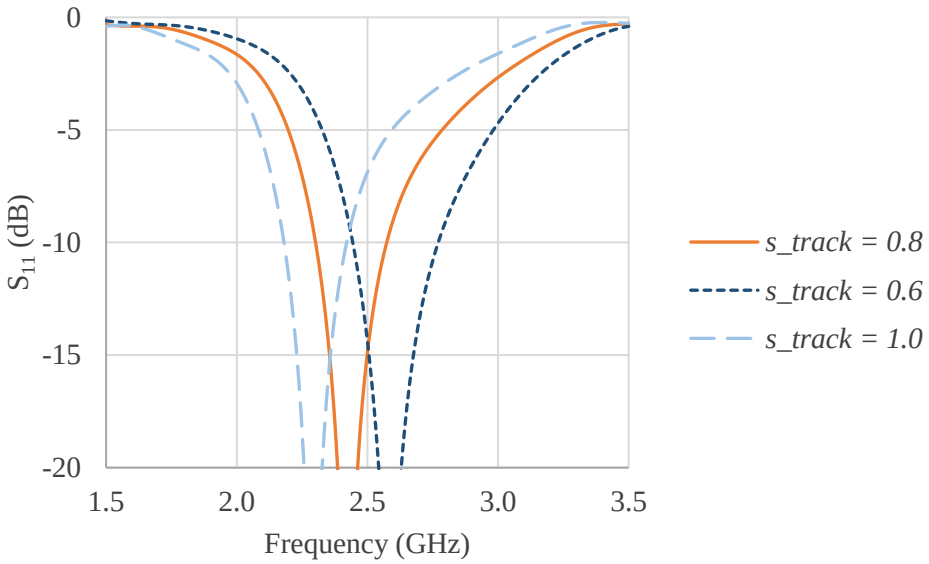

Figure 5-3. Simulated S_{11} for MLA, parameterised s_{track}. Legend shown to the right, units are mm. Original parameter combination shown in orange.

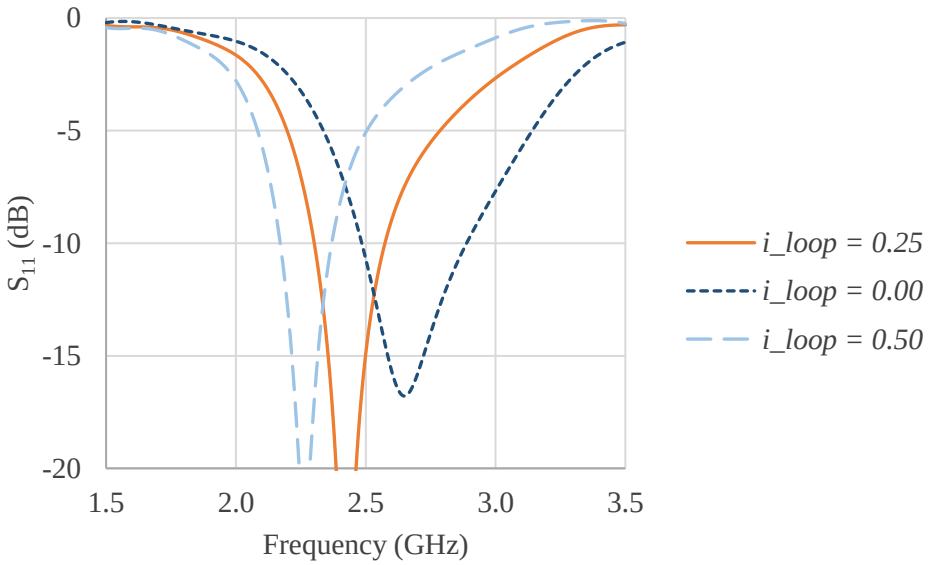

Figure 5-4. Simulated S_{11} for MLA, parameterised i_{loop}. Legend shown to the right, units are mm. Original parameter combination shown in orange.

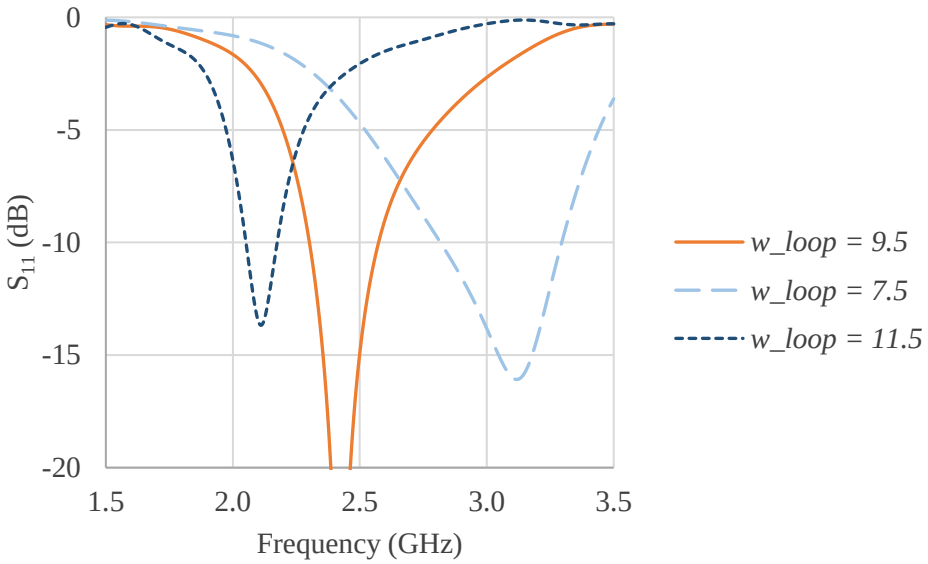

Figure 5-5. Simulated S_{11} for MLA, parameterised w_{loop}. Legend shown to the right, units are mm. Original parameter combination shown in orange.

5.1.2. Fabrication

The optimized MLA design was fabricated in-house using the photolithographic fabrication process. For this initial antenna fabrication, a simple negative mask was used instead of a CGH, as the substrate is planar. A 2 µm coating of Fuji Photo Film Co. Ltd BPRS200 photoresist was subsequently applied and treated via exposure to ultraviolet light passed through a negative mask displayed on an acetate film. After developing the resist, a seed layer (approximately 200 nm thick in total) of titanium followed by gold was deposited using thermal evaporation. Subsequently, after etching away excess photoresist (and metal) using solvents, a copper layer approximately 3-5 µm thick was electroplated onto this seed metal layer; note that skin depth of copper at 2.4 GHz is 1.3 µm. The ground plane was fashioned using adhesive copper tape on the reverse of the substrate. Despite accounting for diffraction effects, actual patterned track widths were approximately 35% thinner than intended; this was due to low intensity of light projected at the edges of the defined tracks. Figure 5-6 shows a photograph of the antenna mounted on a standard SMA connector.

Figure 5-6. Photograph of the manufactured MLA, mounted on an SMA connector (solder not yet applied).

5.1.3. Results and Discussion

Figure 5-7 compares the measured S_{11} characteristics of the fabricated antenna with simulated results for optimized parameters, and for all track widths reduced by 35%. The reduction of the track widths also results in an increase in the separation between horizontal sections, and therefore meaningfully alters the antenna performance. Faults in the tracks, especially in the feed line taper are evident (see Figure 5-6), and are due to improper adhesion of metal on glass; this is likely due to human errors during the fabrication process, for instance the introduction of dust on the substrate. Another potential source of error is a sub-optimal soldered connection between the SMA connector and the antenna. As a result, the S_{11} response of the measured MLA is seen to have an abnormal level of perturbations. At its resonance frequency of 2.2 GHz, the antenna has a *ka* value of 1.1; corresponding FBW_{-3dB} and FBW_{-6dB} values are 27% and 13%, respectively. Note that for the measured S_{11} response shown in Figure 5-7, the half-power cut-off is not a reliable measure of fractional bandwidth, whereas the quarter-power cut-off (FBW_{-6dB}) is more in line with simulation (also approximately 13%).

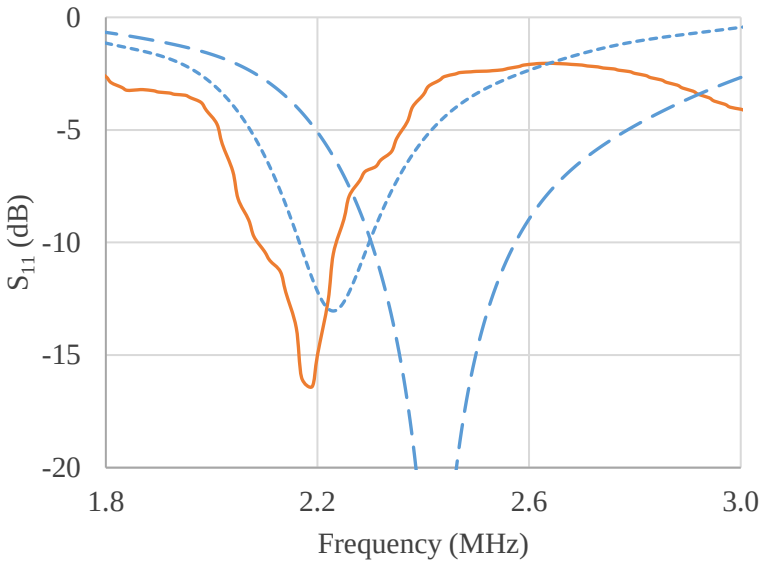

Figure 5-7. S_{11} results for the MLA; (orange) measured, (blue) simulated; (– –) simulation with optimized parameters, (⋯) simulation with all track widths reduced by 35%.

Figure 5-8 shows the measured realized gain in decibels for this antenna, computed using the gain transfer method. Measured results are only available for the dominant φ component; simulated results are presented for both φ (co-polar) and θ (cross-polar) components, and show a difference of more than 20 dB between the two. Measured results for the azimuth plane agree very well with simulations; in the elevation plane, measured gain is lopsided which is likely due to the phase centre of the antenna not aligning perfectly with the centre of rotation of the antenna mount. The average forward gain (±90°) for the φ component of the MLA is −0.1 dBi (simulation), and −1.8 dBi (measurement).

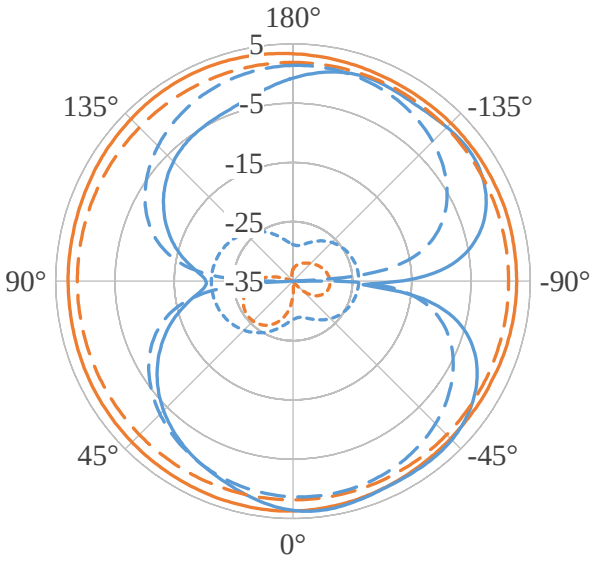

Figure 5-8. Realized gain (dBi) for the MLA at 2.2 GHz; (——) measured φ component, (– –) simulated φ component, (⋯) simulated θ component; (orange) azimuth plane, (blue) elevation plane.

5.1.4. *Comments*

A compact (ka = 1.2) planar meanderline monopole antenna, based on the design presented in [108], was fabricated in-house using the standard photolithography technique. The meanderline structure allows for miniaturization by extending the overall track length, as well as adding self-impedance to the radiating structure; a tapered microstrip line is used to feed this radiating structure and match it to a 50 Ω feed. A parameter study on the simulated model is provided to offer insight into the optimization of the antenna design.

Light intensity at track edges was lower than expected, resulting in thinner track widths than intended from the optimized simulation model and leading to a shift in the resonance frequency of the antenna. Moreover, due to some imperfections in the tracks and solder build up near the feed connector, the return loss curve for the antenna shows more perturbations than expected from simulation. There is good agreement between the measured and simulated gain of the antenna, with the radiation pattern resembling that of a dipole antenna.

5.2. Modified Dome Antenna

Based on a previously published antenna design [72, 109], a rapid prototype of a meanderline hemispherical dome antenna (MHDA) was fabricated on 3D printed plastic (ABS) and damascened with conductive silver paste to overlay metal tracks. The work is a precursor to the following section where the digitated antenna designs discussed earlier are voluminously expanded and fabricated using 3D printing techniques.

Figure 5-9 shows the CST MWS models of two such antennas. As before, the elevation plane is the geometrical x-y plane, while the azimuth plane is the geometrical z-x plane. Both consist of conformal meanderlines on a hemispherical ABS substrate ($\varepsilon_r \approx 3$, $\tan\delta = 0.009$) of radius 40 mm. The antennas are placed on a square FR4 substrate ($\varepsilon_r = 4.3$, $\tan\delta = 0.025$) of area 16 cm^2, with a coaxial feed inserted in the centre for excitation. The $MHDA_A$ consists of eight identical arms (each with a total length of 425 mm) for even current distribution on the surface of the sphere, and fed by microstrip feed lines for improved impedance matching. Designed for closely spaced dual-resonance behaviour, the $MHDA_B$ consists of two sets of four arms each; the longer arms have a length of 520 mm (and are fed by meandering microstrips), whilst the shorter arms have a length of 260 mm (and are fed by straight microstrips).

Note that the different geometries were put in place to investigate the effects of a relative phase delay between the two sets of meanderlines. However, this line of inquiry was placed out of the scope of the project due to an increased focus on planar antenna design and the fabrication of the digitated inverted-F based antennas, as these offered an increased potential for novel research.

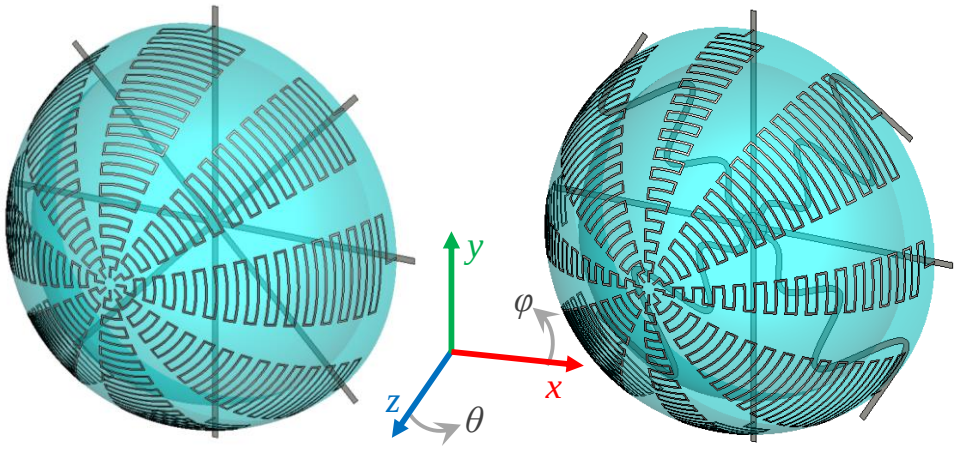

Figure 5-9. CST MWS 3D model of (*left*) $MHDA_A$ and (*right*) $MHDA_B$; grey tracks are metallizations (PEC).

Figure 5-10 shows a photograph of the $MHDA_A$ mounted in an anechoic chamber for testing. It can be seen that there are some defects present in the metal tracks; this is due the presence of unavoidable print defects from the MakerBot printer used. Moreover, there are splotches of silver epoxy where the meanderlines meet the microstrip feed lines; this was caused by the epoxy melting when solder was applied. Return loss characteristics for the two fabricated antennas are presented along with simulated results in Figure 5-11 and Figure 5-12.

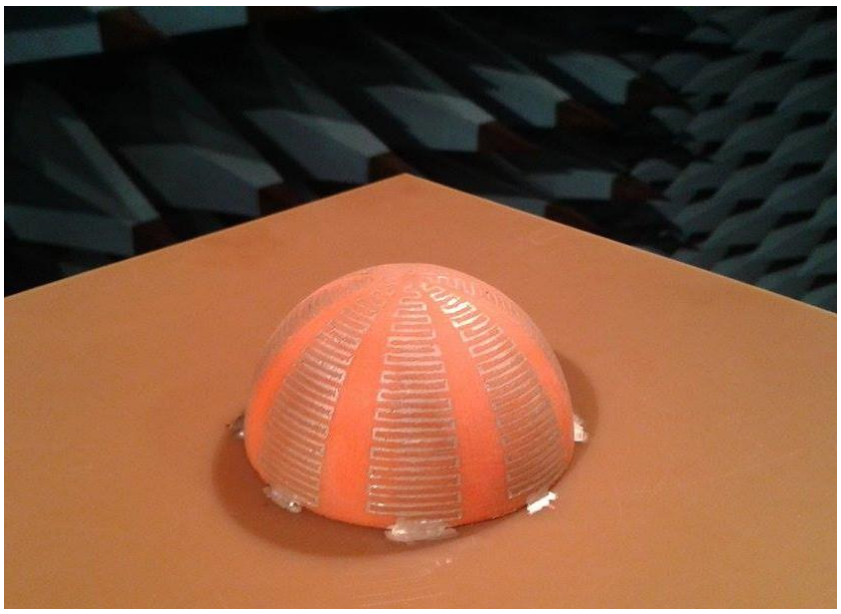

Figure 5-10. Photograph of 3D dome antenna, $MHDA_A$, mounted in ancheoic chamber for radiation pattern measurements.

Measured results for the $MHDA_A$ show that the antenna is resonant at the expected frequency, but that the match is much worse than predicted from simulations. This is primarily due to the sub-optimal connection between the microstrip feed lines and the radiating arms. Similarly, for the $MHDA_B$, it can be seen that whilst the antenna has two distinct measured resonances, the actual resonance values do not line up well with simulations. The two resonances from the long and short arms, which were lined up close together to increase bandwidth at the low frequency point are seen to separate in measurements, implying that fabricated tracks are not continuous (i.e. shorter current paths); similar defects along the meanderlines can be seen for the antenna shown in Figure 5-10. The marked deviation of measured results from simulation predictions confirmed expectations of poor performance from these antennas due to various setbacks in the fabrication process, in particular the metal tracks and connections.

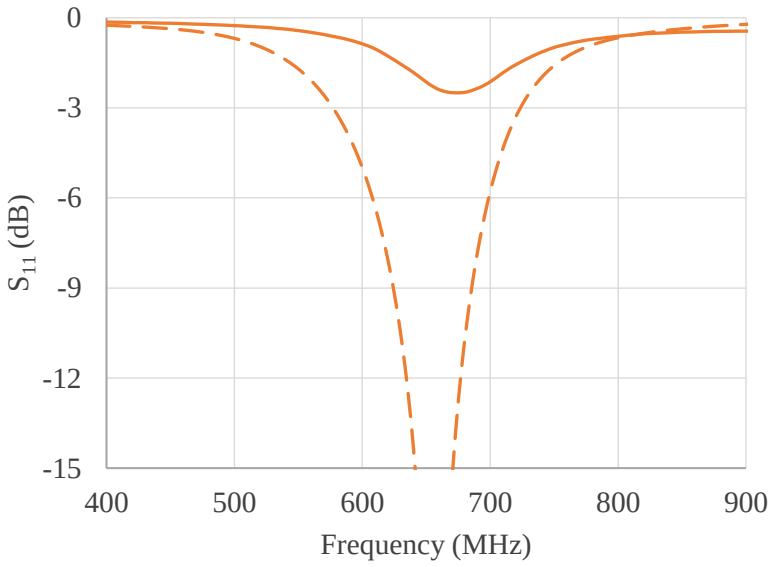

Figure 5-11. S_{11} for (orange) $MHDA_A$; (——) measured and (– –) simulated.

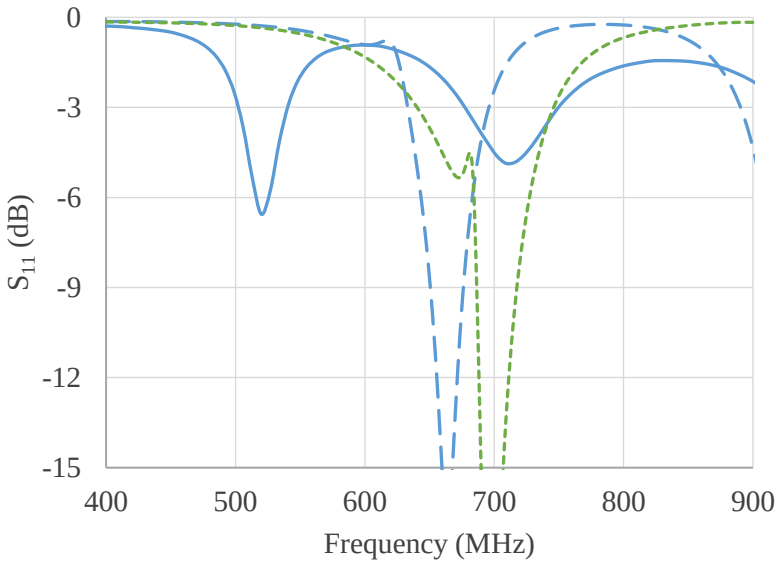

Figure 5-12. S_{11} for (blue) $MHDA_B$; (——) measured and (– –) simulated. Simulated curve for (green) $MHDA_B$ with straight microstrips is also included.

The radiation pattern of the fabricated antennas was measured using a non-standard Yagi-Uda as the transmit antenna. Therefore, only the peak normalized radiation patterns are provided.

The $MHDA_A$ was measured at its resonance frequency of 670 MHz, and is shown compared to the pattern at its simulated resonance frequency of 655 MHz in Figure 5-13. The main polarization is along the θ component. Measurements and simulations line up well in the azimuth plane, except for a dip around ±110° present in simulation but absent from measurements; the measured pattern in the elevation plane is consistently larger than the simulation counterpart. This deviation is most likely a result of misalignment: the results are in line with the antenna being placed lower than its phase centre.

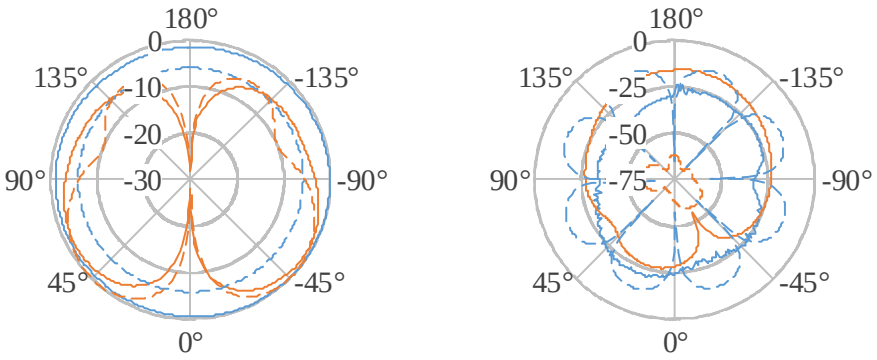

Figure 5-13. Peak normalized radiation pattern (dBi) for the $MHDA_A$; (left) θ component, (right) φ component; (——) measured, (– –) simulated; (orange) azimuth plane, (blue) elevation plane. Cross-polar at least 15 dB below co-polar.

The $MHDA_B$ was measured twice at its resonances of 520 MHz and 710 MHz, which are both compared with the pattern at the deeper resonance point at 665 MHz (in reality, two resonances close together), in Figure 5-14 and Figure 5-15, respectively. The resulting plots exhibit the same trends as those reviewed for Figure 5-13: main polarization is along the θ component, measurements are slightly more symmetric compared to simulations in the azimuth plane, and measurements are steadily higher than simulations in the elevation plane due to the antenna being placed lower than its phase centre.

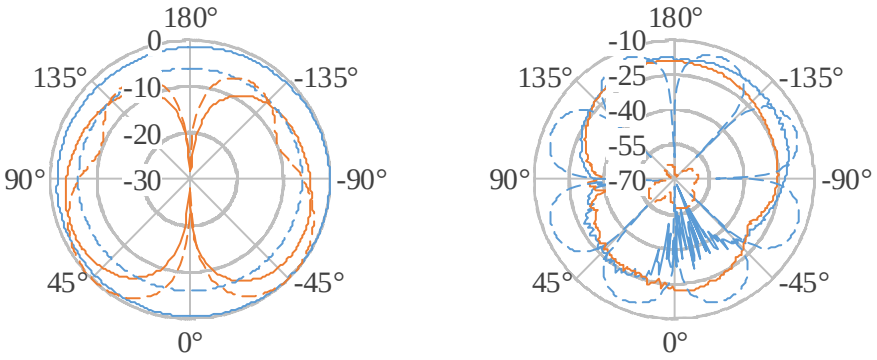

Figure 5-14. Peak normalized radiation pattern (dBi) for the $MHDA_B$, measured at 520 MHz; (left) θ component, (right) φ component; (——) measured, (– –) simulated; (orange) azimuth plane, (blue) elevation plane. Cross-polar at least 15 dB below co-polar.

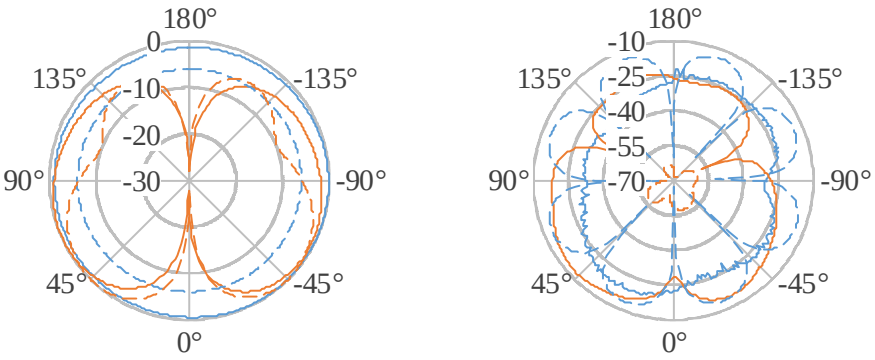

Figure 5-15. Peak normalized radiation pattern (dBi) for the $MHDA_B$, measured at 710 MHz; (left) θ component, (right) φ component; (——) measured, (– –) simulated; (orange) azimuth plane, (blue) elevation plane. Cross-polar at least 10 dB below co-polar.

Though the fabricated antennas did not perform as desired, due to a number of issues in the fabrication process, the endeavour provided useful insight into the skills and tools required to extract and process CAD models into 3D printable files, and the subsequent pre-processing and post-processing involved in the printing process. The practical skills gained were carried forward into the fabrication and measurement of voluminous variants of the CDPIFA introduced in Chapter 3.

5.3. Additive Manufactured Planar Inverted-F Antennas

Based on the CDPIFA covered in Chapter 3, inherently 3D antennas were modelled and subsequently fabricated using powder bed fusion additive manufacture, PBF-AM. This section counts towards a practical validation of small antenna theory, which states that the performance of such an antenna (in terms of bandwidth and efficiency) can be improved by occupying more of the Chu sphere around the largest dimension of the antenna [11, 19, 20].

Simulated results for radiation efficiency are presented for the PIFA as it is voluminously extended into the 3rd dimension. The results are validated with three PBF-AM fabricated antennas: flat, part-spherical (~66% fill-factor), and

full-spherical (~100% fill-factor). Radiation pattern measurements are also provided for the full-spherical variation, and resemble those of the various small antennas discussed thus far. Finally, we compare the effectiveness of the two different heat sources for the fabrication of complex geometries (as necessitated by the centrally populated digitated structure), and assess the viability of PBF-AM, in its current state, as a possible fabrication method for inherently 3D antennas.

Due to the novelty of PBF-AM applied to RF applications, it was not possible to obtain accurate or reliable EM properties for the constituent raw materials, i.e. the powdered forms of metal and plastic used. Whilst the mechanical properties (and changes therein during the printing process) of the various raw materials used in AM have been extensively studied due to the proliferation of 3D printed parts in structural and mechanical applications, EM properties are not as well known. Indeed, one the key challenges identified in any review of AM technology is the need for better understanding of material properties [110-113].

Therefore, in the absence of such information from manufacturers, and without reliable research databases on such material properties, their EM properties were approximated in CST MWS using materials closely resembling these and already included in the software's material library. The antennas are modelled with a hollow substrate with ε_r of 1.2, arrived at through iterative simulations, and tanδ of 0.06 (comparable to FR4), and a metal based on the properties of copper, but with reduced conductivity (σ = 5.8E5 Sm^{-1}).

5.3.1. Voluminous Expansion of PIFAs

Figure 5-16 shows cross-sectional CAD model views of three PIFAs, increasingly occupying the full volume of an imaginary sphere; in each case, the width of the antennas is 30 mm. Simulated results for the resonance frequency and efficiency as a function of the parameter *h* (as described in Figure 5-16) are provided in Figure 5-17 and Figure 5-18, respectively.

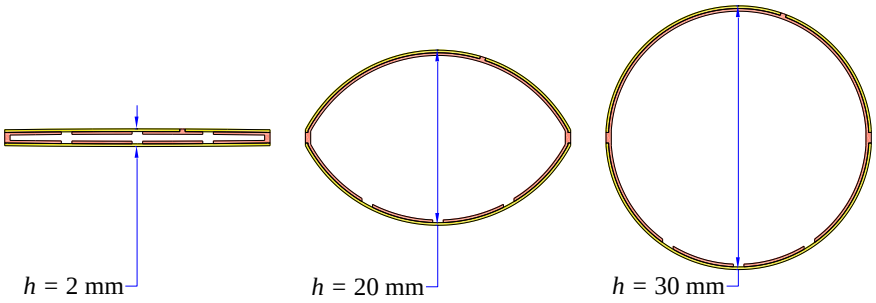

Figure 5-16. Cross-sectional view of CAD models simulated in CST MWS, for progressively greater voluminous expansion.

As with the CDPIFA, simulations reveal that the antennas exhibit two closely spaced resonances. It can be seen from Figure 5-17 that the 2nd resonance varies more as a function of the voluminous expansion, *h*, as compared to the 1st resonance, with the general trend that the respective frequencies at resonance reduce as *h* increases, since the currents have a longer effective length on a more curved surface. The corresponding radiation efficiency at resonance also exhibits a general trend, where the efficiency increases as *h* is increased and the antenna occupies more and more of the Chu sphere. Over the two resonances, the mean radiation efficiency of the flat antenna is 9.5%; for the full-spherical antenna, this is increased to 53%.

Establishing an overall trend for this particular antenna geometry, at the dimensions specified, a unit (1 mm) change in height *h* results in an increase in radiation efficiency of 1.6 percentage points. Thus, where viable (subject to availability of space), the antenna can be made more efficient in order to reduce power consumption. The resonance frequencies can be subsequently tuned depending on the required application as per the design guidelines provided in the parametric study in Chapter 3.

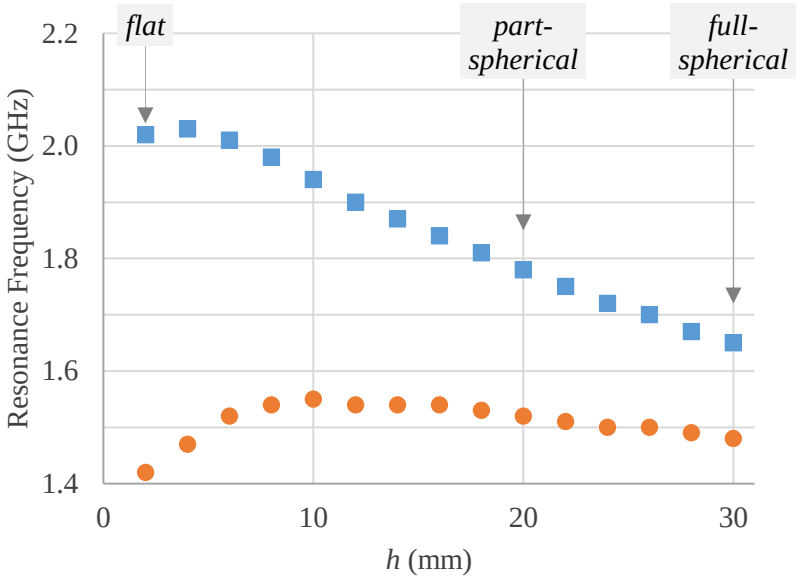

Figure 5-17. Simulated resonance frequency of (orange) 1st and (blue) 2nd resonances as a function of *h*. Fabricated antennas are annotated.

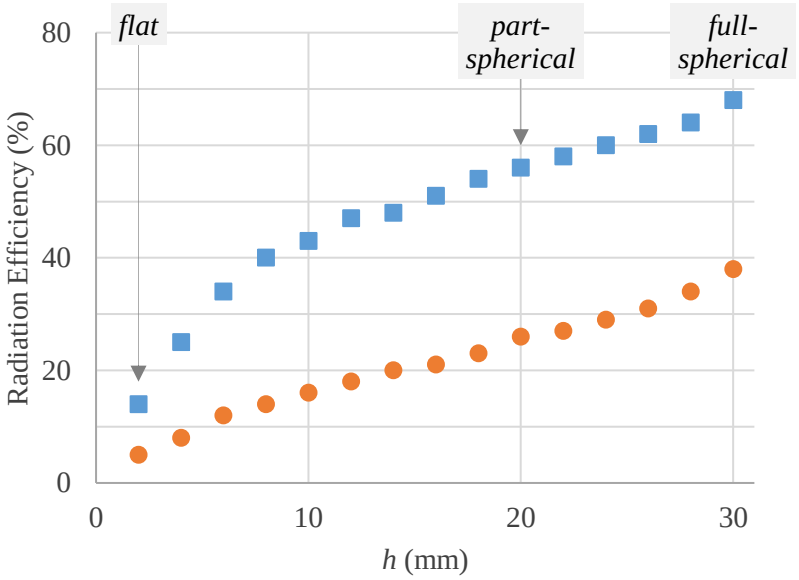

Figure 5-18. Simulated radiation efficiency of (orange) 1st and (blue) 2nd resonances as a function of *h*. Fabricated antennas are annotated.

5.3.2. Fabrication

PBF-AM processes comprise the layered, sequential build-up of 3D parts or structures. This is achieved by decomposing the 3D part into a stack of 2D cross-sectional layers. A thin layer of powder (ranging from ~10 to ~100 µm) is

deposited onto a printing bed and a suitable heat source subsequently used to melt the cross-sectional layers, one at a time [24]. Two predominant technologies are SLM and SEBM, with laser and electron beam as the respective heat sources. In general, slower build times allow for a more robust structure and a more homogeneous deposition of material throughout the thickness of the structure; faster build times are (potentially) approachable as the machine operators gain more confidence in the process timelines required for optimal build quality.

The SLM process was trialed first, on a Renishaw AM250 printer [99], as it typically provides higher resolution than SEBM and can yield parts with a smoother surface finish. A key disadvantage, however, is that SLM is much less capable of manufacturing overhanging features such as the centrally populated digits on these antennas. Usually, this limitation is overcome with the use of sacrificial support structures, analogous to the use of scaffolding in building construction. Whilst these support structures were intentionally melted in such a fashion as to reduce their structural integrity, the force needed to remove these damaged the digits beyond an acceptable degree. Some of the clipped support structures also left small stubs between two digits which presented an issue in terms of regulating the current paths on the antenna. A photograph of an antenna part fabricated with SLM is shown in Figure 5-19, where the partly-removed support structures can be clearly seen. The support structures which are on the outside of the surface can easily be buffed away; however, removal of those behind the digits resulted in distortion of the structure.

With the issue of the support structures proving too problematic, the SEBM process was used instead, on an Arcam A2 printer [100]. The process is better suited to the current antenna geometry as the metal powder is pre-sintered before further processing by the SEBM heat source, removing the need for support structures. A photograph of an antenna part fabricated with SEBM is shown in Figure 5-20. Evidently, the surface finish and resolution are much worse than the laser processed counterpart. This is due to the use of coarser powder layers with the SEBM process (40-105 μm compared to 15-45 μm for the laser

process), and the comparatively larger area affected at any one time by the electron beam compared to a heating laser.

Figure 5-19. Photograph of antenna part (material: titanium alloy) fabricated using SLM PBF-AM.

Figure 5-20. Photograph of antenna part (material: titanium alloy) fabricated using SEBM PBF-AM.

The antenna radiator and ground plane were fabricated separately using a Titanium alloy, Ti-6Al-4V ($\sigma \approx 10^5$ Sm^{-1}). Hollow plastic substrates fabricated from the plastic nylon12 were used to provide support. Copper tape was then used to short the top metallization to the ground plane, and to provide contact

pads for soldering SMA connectors. Photographs of two fabricated prototypes are shown in Figure 5-21.

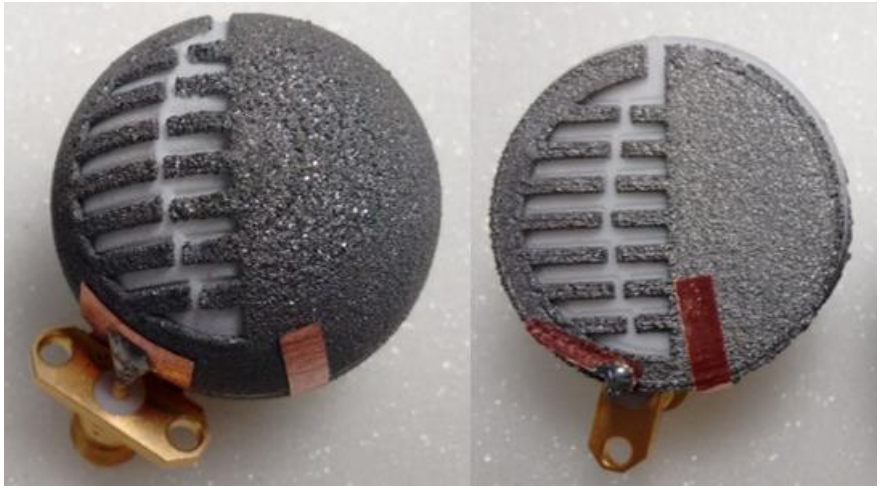

Figure 5-21. Photograph of two SEBM PBF-AM fabricated antenna prototypes, shown assembled; (*left*) full-spherical, (*right*) flat.

In total, for this project, four iterations of fabrication were performed; each iteration sought to improve build quality, specifically the surface finish. The build process for the four SEBM fabricated antennas presented in this chapter is described as follows:

- The Arcam A2 printer was run under a vacuum of about 0.0001 mbar; a slight amount of helium was inserted into the chamber to help dissipate the charge induced into the powder bed by the electron beam
- All parts were built on a stainless-steel plate, which was heated to 730 °C by the electron beam before any powder was deposited
- For each layer of powder deposited (50 µm thick), the beam was first defocused and scanned across the layer at a high speed (30 ms^{-1}) with 2.3 kW power, for around 15 seconds, to sinter the powder
- Each part area was subsequently melted using a focused beam with a back and forth raster pattern at a speed of around 0.35 ms^{-1} with 300 W power

- Thereafter, successive powder layers were deposited and the previous sintering and melting steps repeated until the antenna parts were fully realized

Eighteen antenna parts (radiator and ground plane separate, i.e. total of nine antennas) were printed, with a total printing time of 2 hours and 24 minutes. The entire printing process, including post-processing, was completed within 4 hours. Of the total nine antennas, three each were flat, part-spherical, and full-spherical. Some parts were damaged or lost in postprocessing, where pressurized air was used to separate the final melted parts from sintered powder blocks, due to inexperience; some others were rendered unusable at the assembly stage due to the application of excessive mechanical force.

5.3.3. Results and Discussion

As pointed out earlier, due to the uncertainties in material properties, measurements were carried out for return loss and efficiency, and the results used in a feedback loop to more accurately reflect the construction of the simulation models in CST MWS. As such, it is not possible at this stage to compare these AM fabricated antennas to antennas fabricated using conventional techniques.

Return loss measurements for the antennas were performed using a VNA. The radiation efficiency was subsequently computed with measurements taken with the antennas enclosed in a Wheeler cap box, using the constant-loss-resistor method (see Chapter 2, [86]). Due to low measurement precision, only the efficiencies for the second resonance were computed, since the absolute figures are higher and therefore negative/invalid results unlikely. Two sets of measurements provided for the full-spherical antenna serve to illustrate measurement precision.

Figure 5-22, Figure 5-23, Figure 5-24, and Figure 5-25 compare the measured and simulated S_{11} parameter for the flat, part-spherical and two full-spherical prototypes, respectively. Simulated efficiency at resonance and measured efficiency for 20 MHz bandwidth about the resonance frequency are also

displayed. As for the agreement between measurements and simulations, it can be said that only a general trend is visible, with a considerable and noticeable departure in the exact values for resonance frequencies, bandwidths, and efficiencies. These differences may be attributed to the host of difficulties discussed above in the manufacture and accurate simulation of the antennas. Nevertheless, with the quality of samples currently available and the state of knowledge about material properties, an adequate first impression is evident in the trends observed in simulations and measurements: namely the lowering of the second resonance frequency as the parameter *h* is increased, and a subsequent increase in the radiation efficiency.

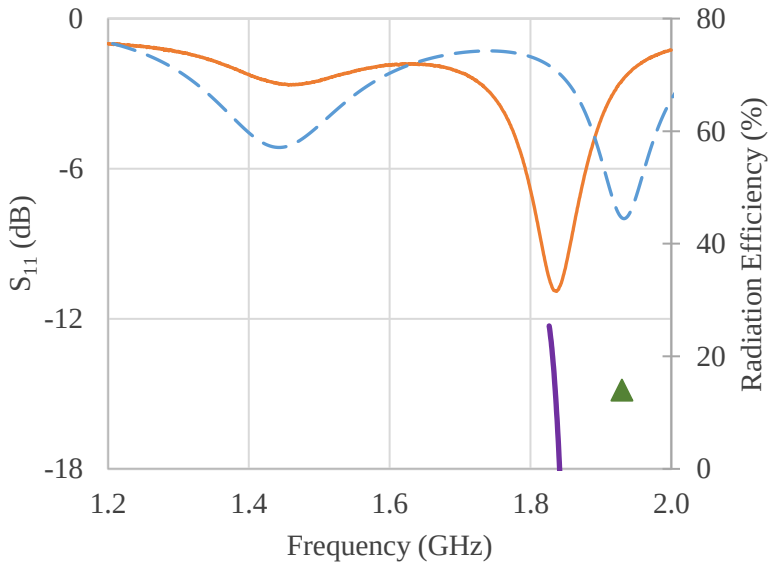

Figure 5-22. S_{11} results for PBF-AM flat CDPIFA; (orange) measured, (blue) simulated. Radiation efficiency at respective resonance frequencies, for the 2nd resonance; (purple) measured, (green) simulated.

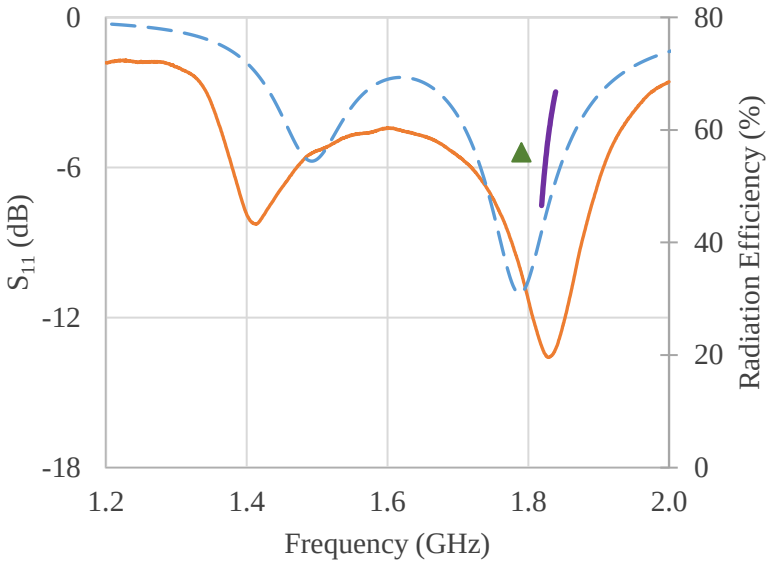

Figure 5-23. S_{11} results for PBF-AM part-spherical CDPIFA; (orange) measured, (blue) simulated. Radiation efficiency at respective resonance frequencies, for the 2nd resonance; (purple) measured, (green) simulated.

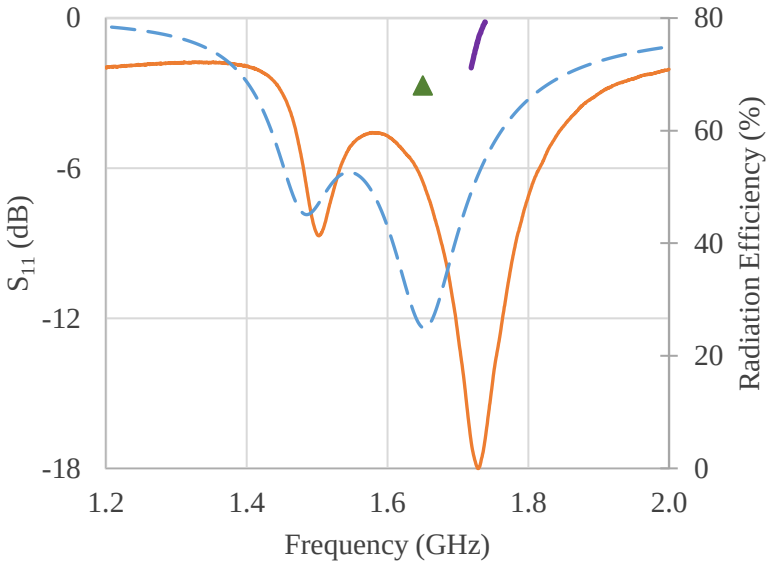

Figure 5-24. S_{11} results for PBF-AM full-spherical CDPIFA, sample A; (orange) measured, (blue) simulated. Radiation efficiency at respective resonance frequencies, for the 2nd resonance; (purple) measured, (green) simulated.

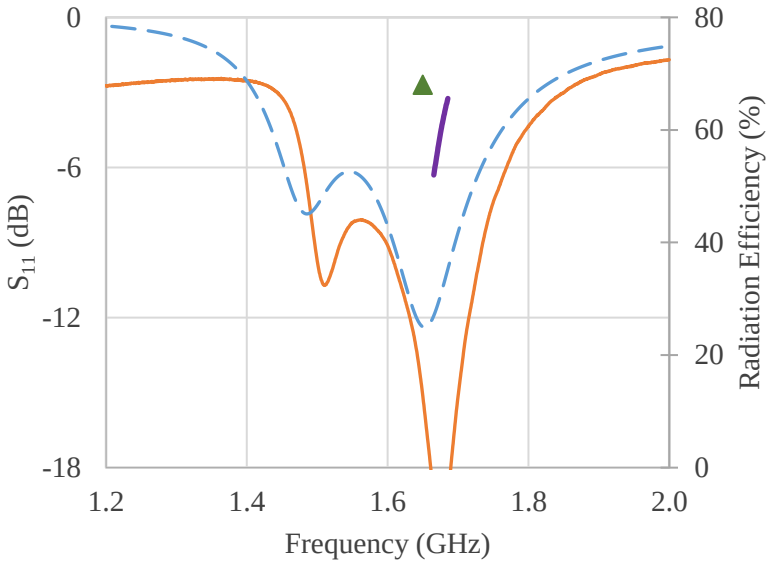

Figure 5-25. S_{11} results for PBF-AM full-spherical CDPIFA, sample B; (orange) measured, (blue) simulated. Radiation efficiency at respective resonance frequencies, for the 2nd resonance; (purple) measured, (green) simulated.

Key results for the 2nd resonance of each antenna are summarized in Table 5-2. Note that the parameter Q_{ratio} is not directly applicable to antennas exhibiting two resonances close together, as there is not yet a consensus in the antenna community for whether the relationships between Q and bandwidth hold for such behaviour [19].

Table 5-2. Simulated and measured resonant frequency and radiation efficiency at 2nd resonance for PBF-AM fabricated CDPIFAs.

	Flat	*Part-spherical*	*Full-spherical (sample A)*	*Full-spherical (sample B)*
Simulated frequency (GHz)	1.93	1.79	1.65	-
Measured frequency (GHz)	1.84	1.83	1.73	1.68
Simulated efficiency (%)	14	56	68	-
Measured efficiency (%)	11	59	76	60

Lastly, the realized gain for the fully-spherical CDPIFA was measured in an anechoic chamber, as described in Chapter 2. Due to the particular feed location for this antenna, partial power gains were measured with respect to vertical and horizontal polarizations, and the gain transfer method (see Chapter 2) used subsequently to compute the total realized gain. Figure 5-26 and Figure 5-27 plot the results for azimuth and elevation planes respectively, measured at 1.7 GHz. As observed with previous ESA gain measurements, there is a large degree of undulation in the radiation patterns; in particular, there are some artefacts due to the setup (antenna holder) in the azimuth plane towards the rear of the antenna. There is, however, good agreement between the two measured patterns, with a total average difference of 1.7 dB.

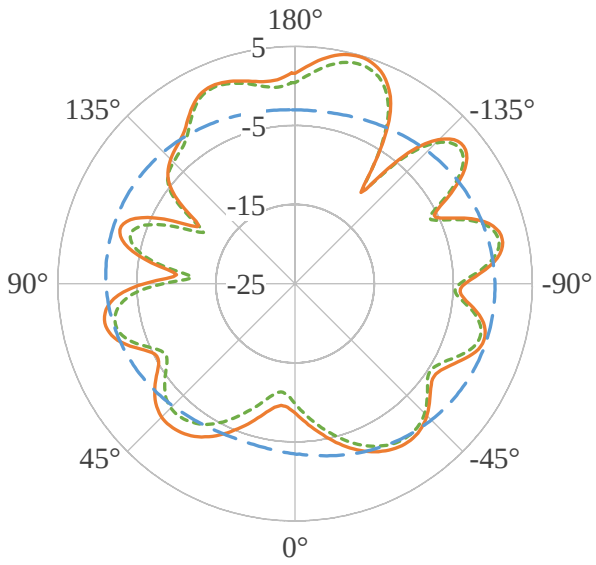

Figure 5-26. Realized gain (dBi) for the full-spherical ESA at 1.7 GHz; (orange) measured – sample A, (green) measured – sample B, (blue) simulated; azimuth plane. Combined absolute gain (φ *and* θ components).

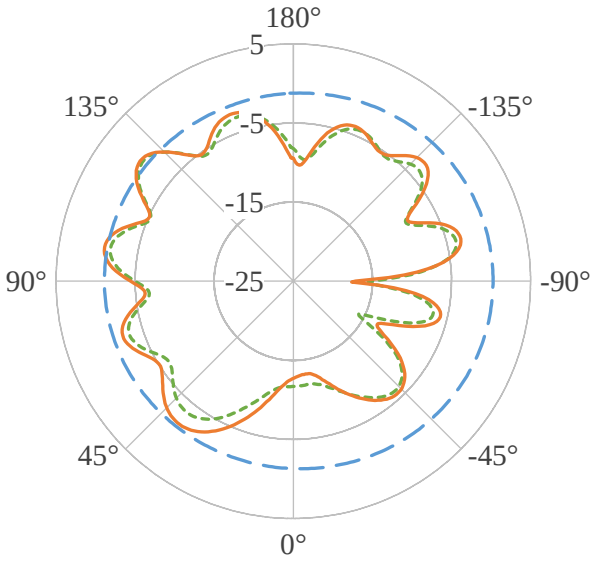

Figure 5-27. Realized gain (dBi) for the full-spherical ESA at 1.7 GHz. (orange) measured – sample A, (green) measured – sample B, (blue) simulated; elevation plane. Combined absolute gain (φ *and* θ components).

5.3.4. *Comments*

A novel application of the PBF-AM technique to the fabrication of three-dimensional antenna designs is reported. Limitations included a lack of information regarding the EM properties of raw materials (and how these evolve as the powdered raw material is sintered into solid geometries), as well as the necessitated application of copper tape as contact pads for SMA connectors.

Despite these limitations, general trends observed during simulations, i.e. the behaviour of the resonance frequency and the antenna's radiation efficiency as a function of voluminous expansion, are corroborated with measurements. Two samples of a fully three-dimensional, spherical antenna have a measured radiation efficiency of 76% and 60% (average 68%); contrasted to the efficiency for a flat counterpart, which is computed as 11%, there is an increase of 57 percentage points. Further research is required to improve confidence in the absolute values obtained.

The obvious drawback with voluminous expansion is the increase in the antenna's profile (height), which might limit its practical application. This can

be partly addressed by a variation in antenna design where the rear metallization (ground plane) is kept flat as the top radiator is voluminously expanded. Such a structure, with a flat ground plane, would be better suited to the majority of applications where traditional, planar antennas are currently installed since the antenna can simply be placed on top of an existing metallized surface. However, due in part to less accurate reproductions of currents on the surface of the new hemispherical antennas, a sacrifice in the radiation efficiency is to be expected.

Figure 5-28 and Figure 5-29 plot the simulated resonance frequency and efficiency as a function of the parameter *h* for these hemispherical variations (note that for diameter 30 mm, maximum value of *h* for full-hemisphere is 16 mm instead of 30 mm for full-sphere). The trends in resonance frequency and radiation efficiency follow those previously established in Figure 5-17 and Figure 5-18. Over the two resonances, the mean radiation efficiency of the flat antenna is 9.5%; for the full-hemispherical antenna, this is increased to 40.5%.

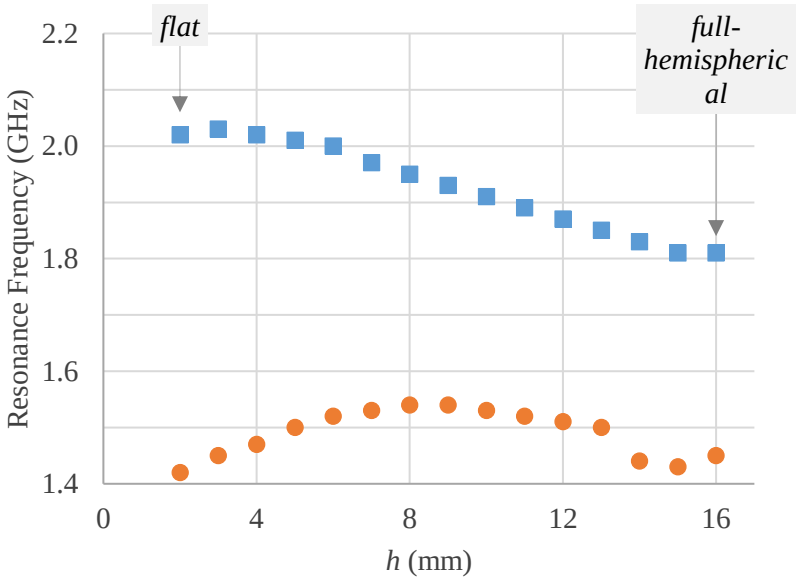

Figure 5-28. Simulated resonance frequency of (orange) 1st and (blue) 2nd resonances as a function of *h*. Extremes are annotated.

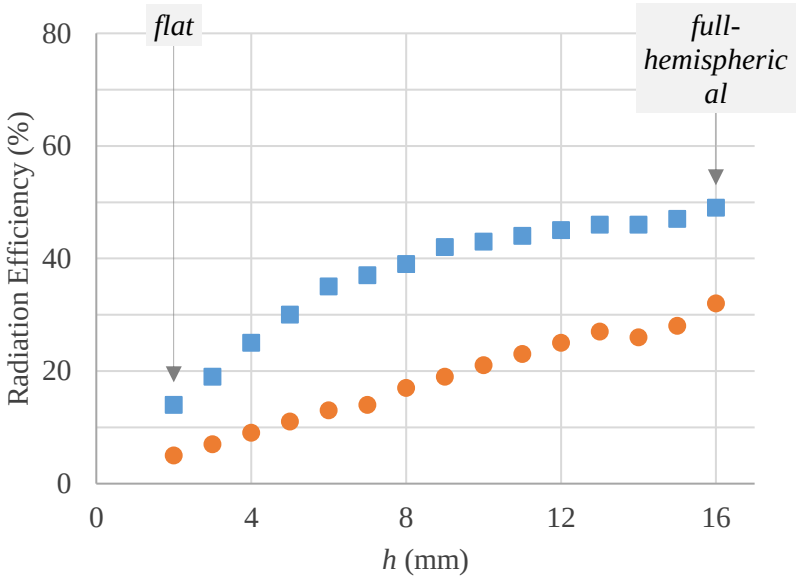

Figure 5-29. Simulated radiation efficiency of (orange) 1st and (blue) 2nd resonances as a function of *h*. Extremes are annotated.

Establishing an overall trend for this particular antenna geometry, at the dimensions specified, a unit (1 mm) change in height *h* results in an increase in radiation efficiency of 2.2 percentage points. Thus, whilst the maximum (averaged over first two resonances) efficiency available for a full-hemispherical geometry, at 40.5%, is over 10 percentage points lower than the maximum achievable for a full-spherical geometry, the gain in efficiency per unit of height increased is improved.

Finally, there is room yet for improvement in the surface finish achieved using SEBM. Figure 5-30 shows a photograph of an unused antenna part fabricated with an Arcam A2 printer after iterative optimization of the build process. A noticeable improvement can be seen over the components used in measurements (c.f. Figure 5-20); however, at the time of writing, these improvements could not be carried onto 3D counterparts. Lastly, the use of copper powder as the raw material, which is the subject of current research at the Sheffield Mercury Centre, would further improve the robustness and packaging of fabricated antennas.

Figure 5-30. Photograph of unused antenna part fabricated using SEBM PBF-AM, illustrating the improvement to surface finish through process optimization (c.f. Figure 5-20).

5.4. Summary

This chapter provided three varieties of ESAs fabricated in-house using photolithography and additive printing. The primary motivations were to obtain an understanding of these processes, and to assess the readiness of emergent techniques for rapid prototyping and mass manufacture of non-traditional antenna geometries.

The first antenna is a planar MLA, where the front metallization is achieved using a standard lithography process. This exercise was planned as a precursor to the patterning of non-planar substrates with the use of holographic photolithography; this line of research could not be concluded due to unplanned limitations with support personnel and equipment, and was supplanted with a greater focus on AM fabrication techniques. Track widths on the fabricated antenna were thinner than desired, resulting from variance in light intensity across the profile of the tracks. This highlights a key challenge in non-contact lithography: small imprecisions in misalignment can lead to considerable

changes in final patterned tracks. In a similar vein, such ‘misalignments’ would be unavoidable for the case of non-planar substrates, where light projected through standard photolithographic masks diffracts as it exits the mask. This is a limitation directly overcome by holographic photolithography where specialist masks are engineered in such a way that emergent light beams can be locally focused as per the topography of the substrate. Still, the process is unable to accommodate inherently 3D structures without the use of complex optics to illuminate areas of a substrate which would lie under a shadow when illuminated directly from above.

Next, the focus was shifted to the use of AM techniques. At first, two variants of a dome antenna were fabricated; the substrates were 3D printed with ABS plastic, and metal tracks subsequently defined by damascening conductive silver paint onto the substrate. Due to unavoidable print defects in the indented grooves, the fabricated tracks had poor definition; moreover, the integrity of connections between the meanderlines and feed lines was compromised during soldering. As a result, measurements and simulations were not closely aligned.

Finally, the suitability of PBF-AM to directly fabricate metallic prototypes was investigated. Through this technique, it was possible to fabricate variants of the CDPIFAs discussed in Chapter 3 with varying heights (or volume). Measurements show an increase in the radiation efficiency with an increase in volume; this trend is corroborated with simulations. As the height of the antenna is increased, the measured radiation efficiencies for a flat, part-spherical, and full-spherical are 11%, 59%, and 68% (averaged between two samples), respectively. However, a key limitation in the confidence of the actual efficiency values is a lack of knowledge of the material properties, and how these change as the powdered form of raw materials is sintered and melted to form solid structures.

It can be argued that the techniques used to realize holographic photolithography may be incorporated into existing industrial processes (of photolithography). As such, this technique may be better suited in the near term as a means of fabricating inherently 3D antenna designs (note that underlying

features would still require careful attention; thus, monolithic fabrication would still not be possible). On the other hand, this past decade has seen exponential growth in the availability and sophistication of AM techniques, prompting further research into the fabrication of RF components. As material properties are better understood and the printing process optimized for electronics (and especially RF components), PBF-AM is poised to be uniquely suitable for both rapid prototyping and mass fabrication of antennas.

It is hoped that results presented here catalyze further research into 3D printed RF components, to drive further maturation of the technology. Possible next steps are detailed investigation of the material properties under flux, the use of higher conductivity metals, and continued improvements in the surface finish and integrity of printed structures. With better understanding of material properties, reliability analyses would be an immediate next step. Ultimately, future research can investigate the suitability of AM for mass manufacture of RF parts.

CHAPTER 6

6. Conclusions

The aim of this Thesis was to investigate the miniaturization and optimization of antennas, with considerations for fabrication. Like the many modern antennas found in mobile electronic devices, an antenna is classed as electrically small if it operates at a wavelength(s) many times its physical size. More specifically, taking the radius of the smallest sphere (termed the Chu sphere) that would completely encapsulate a particular antenna as a, an antenna is classed as electrically small if the product of the wavenumber k ($= 2\pi/\lambda$) and the parameter a is less than or equal to 0.5 (also acceptable is $ka \leq 1.0$). These values represent an imaginary spherical boundary containing the first order radiation modes, and the demarcation between near and far fields of a Hertzian antenna, respectively. Furthermore, it is widely accepted that as the electrical size of an antenna is reduced, its performance (in terms of gain, efficiency, and bandwidth) deteriorates. Generally, the radiation resistance decreases, while the reactive component of its impedance increases, leading to a poor match with the feed line or network. The following is a summary of the contributions of this Thesis.

An extensive literature review was presented, covering a range of miniaturization techniques applied to antennas. The relative advantages and disadvantages were discussed, and geometrical shaping was identified as a miniaturization technique which could be intuitively applied and would result in an antenna that would be simple to fabricate with traditional techniques. To these ends, a novel, digitated structure was integrated into an IFA to reduce its electrical size by increasing the antenna's self-inductance and self-capacitance. The presence of a large number of tuneable parameters means that the antenna is well suited for computational optimization algorithms, in order to determine the best possible impedance match at a desired frequency. Additionally, the

digitated structure can be abstracted into a simpler, two-element design, which is more suitable for gaining an intuitive understanding. In terms of ease of manufacture, the uni-planar CDIFA is well suited to traditional fabrication techniques, such as photolithography and machine etching. Through vias are employed to feed the antenna, which is a standard process in PCB manufacture. The absence of lumped reactive components (i.e. chip capacitors or inductors) further simplifies the fabrication process, lowering manufacturing costs. Furthermore, the antennas are very low profile, capable of integration directly into the main PCB of an electronic device. The compact profile of the antenna is especially suited to handheld mobile devices such as 'smart' watches, as proposed in [114].

Bandwidth enhancement was investigated through a variant of the IFA, with the new structure closely resembling a PIFA. Termed the CDPIFA, the front metallization of this antenna is similar to that of the CDIFA; the back is completely metallized, and therefore does not require any extra processing for etching techniques. A shorting pin between the radiator and ground sections is realized with copper tape, though it can be replaced by through vias in future iterations for increased stability. This antenna structure offers two paths (in opposing directions) for current flow, the respective lengths of which can be altered to tune two resonances (with orthogonal polarity) close together. Due mainly to losses in the substrate, these antennas were found to be very low efficiency, though the extended bandwidth makes them tolerant to environmental effects (such as detuning). With their low efficiency, the antennas are more suited to receive than transmit applications where the signal-to-noise ratio (SNR) of the incoming signal is often the main limiter in terms of system performance [22].

It is widely accepted that the 'best' compromise between miniaturization and performance is achieved when an ESA makes full use of the Chu sphere as determined by its maximum dimension. From the perspective of planar printed antennas, this implies an increase in height, and a spherical shape. Additive manufacturing was employed to fabricate variants of the CDPIFA with different heights, i.e. different fill factors with respect to the Chu sphere. Whilst the material properties of raw materials used in PBF-AM are not yet fully

characterized, measured results follow theoretical expectations of an increase in the radiation efficiency as the antenna is made more voluminous.

A planar MLA and a 3D dome antenna with meanderlines were also prototyped using traditional photolithography and additive printing (and subsequent metallization with conductive ink), respectively, to develop an intimate understanding of these fabrication processes alongside research into antenna miniaturization. Research into the investigation of computer generated holograms for holographic lithography was subsequently pivoted in favour of the investigation of the suitability and readiness of AM to prototype ESAs, primarily due to the opportunity for pioneering measured results of metallic 3D printed antennas. The PBF-AM process employed for the fabrication of 3D CDPIFAs is one of the few AM technologies able to directly print metals. As the process gains further sophistication, it could emerge as a viable option for the mass manufacture of monolithic, inherently 3D antennas.

6.1. Recommendations for Future Work

This section provides recommendations for the refinement of the results and ideas presented in the Thesis, and offers some clues for further research work which can be built on the current work.

6.1.1. Antenna Design

The design methodology employed for antenna miniaturization was based on geometrical shaping, mainly due to the subsequent ease of manufacture using traditional methods; this was achieved with the use of a centrally populated digitated structure in variants of IFAs. A natural extension of the work would be to investigate the effects of similar structures on other antenna types, such as loop or slot, and to produce simple predictive models for a first estimate of antenna performance based on only a few parameters.

Furthermore, having established the usefulness of PBF-AM in rapid prototyping and potential for mass manufacture, the antenna design stage may be revisited with added freedoms in terms of inherently 3D designs. For instance, layered

conducting structures may be incorporated in a conformal configuration to further miniaturize multi-element antenna structures; one example is passive directive elements on patch or Yagi-Uda type antennas, another is underhanging capacitive ‘top hats’. The technique is particularly suited to the fabrication of all-metal, space-filling, wire-type antenna structures generated using computational algorithms. As printing speeds are increased, PBF-AM can be integrated more closely into the design process, offering a quick first estimate of the measured performance of antenna structures designed in CAD and simulation software such as CST MWS.

6.1.2. Antenna Measurements

A range of different antennas were measured and their results presented in the course of the discussion thus far. It can be observed that the radiation patterns obtained for antennas with *ka* greater than 1 are far better defined than those whose *ka* value is less than 1 (i.e. ESAs). Part of the low resolution and precision of these measurements is the difficulty in correct alignment of the (also) physically small antenna structures, which can be improved with careful design of the support apparatus around the AUT.

The use of a copper-clad coaxial feed cable further contributed to any imprecisions and inaccuracies in the measured results, and made straightforward simulation of the antenna structures difficult. This is understood to be primarily due to leakage currents forming on the feed cable and contributing to the EM fields radiated by the antenna itself. These unwanted effects may be eliminated with the use of an optical fibre cable instead of the traditional coaxial cables, together with some type of opto-electric field sensors and RF-optical transducers [11]. Efforts were made to employ such a measurement setup at the National Physical Laboratory (NPL) [115, 116], but were ultimately set aside due to financial constraints. This sort of setup might appear more cost-effective for potential future work where measurement accuracy is of greater concern.

6.1.3. Additive Manufacture and Material Characterization

It was emphasized that PBF-AM is currently limited only to prototyping of antennas, due to the dearth of knowledge regarding the EM properties of raw materials used. This has been identified as a key challenge in the development of AM in general [110-113], with future progress poised to extend the application of AM to general mass manufacture. In particular, unknown changes to material properties during the fabrication process limit the usefulness of raw material properties. However, existing measurement techniques can be employed to approximate the electrical permittivity and loss tangent of dielectrics (e.g. coaxial probe and free-space methods for powders, and transmission line method for 3D printed solids) [117, 118], as well as the electrical conductivity of metals [119, 120] fabricated using AM. As process tolerances are better understood and formalized, such methods can be used to create a database of the properties of various AM fabricated materials.

It was also demonstrated that there is room for improvement in the quality (in terms of resolution and surface finish) of parts that can presently be produced. Further optimization of the printing process, together with the use of materials traditionally employed for electronics (e.g. copper) can lead to improvements in the quality of antenna parts realized with the current state of art. (The liaising Mercury Centre recently started its investigation of copper as a raw material for AM processes.)

Lack of flexibility in AM parts is currently a major limitation for the technique compared to processes such as conformal direct-write printing or direct transfer patterning. Recently though, the concept of four dimensional (4D) printed metal has been publicized [121, 122], whereby flexible, shape-altering metallic structures can be realized using enhanced AM techniques; typically, the material properties are a function of potential external stimuli such as temperature or pressure. Such advances have the potential to significantly hasten the proliferation of AM in antenna research and development.

6.2. Concluding Remarks

Through this report, I have presented findings on an intuitive design methodology covering the integration of digitated structures in inverted-F and related antennas, and produced pioneering measured results for voluminous (3D) metallic antennas fabricated with PBF-AM.

A ‘design matrix’ was produced, linking key parameters of a simplified digitated structure to antenna miniaturization and efficiency; its use as a means for antenna designers to obtain rapid first estimates over a range of frequencies without the use of costly computational simulations was also demonstrated. Several prototypes were fabricated as well, using traditional processes, and shown to compare well with published antennas from literature. Indeed, there is scope yet for further formalization of parametric characterization approach, either in terms of more performance metrics, or a more detailed equivalent circuit model. While practical challenges endure in the measurement of electrically small antennas such as those discussed, I remain sanguine that these will not hold hostage future practical research, and hopeful that the measurement procedures detailed here would be of aid in such undertakings.

Pilot investigations into PBF-AM fabricated antennas have demonstrated that the technology is ready for prototyping purposes, justifying further investigation of this and related AM technologies for RF components. I am optimistic that these findings will be of aid to future researchers, and that this collaborative venture will embolden an appetite for further concerted interdisciplinary teamwork.

References

[1] A. B. Frazier, R. O. Warrington, and C. Friedrich, “The miniaturization technologies: past, present, and future,” *IEEE Transactions on Industrial Electronics*, vol. 42, no. 5, pp. 423-430, 1995.

[2] R. R. Schaller, “Moore's law: past, present and future,” *IEEE Spectrum*, vol. 34, no. 6, pp. 52-59, 1997.

[3] E. Mollick, “Establishing Moore's law,” *IEEE Annals of the History of Computing*, vol. 28, no. 3, pp. 62-75, 2006.

[4] J. U. Knickerbocker *et al.*, “Three-dimensional silicon integration,” *IBM Journal of Research and Development*, vol. 52, no. 6, pp. 553-569, 2008.

[5] R. R. Tummala and M. Swaminathan, *Introduction to System-on-Package (SOP): Miniaturization of the Entire System*. USA: McGraw-Hill, 2008.

[6] R. W. Keyes, “Physical limits in digital electronics,” *Proceedings of the IEEE*, vol. 63, no. 5, pp. 740-767, 1975.

[7] R. W. Keyes, “Fundamental limits of silicon technology,” *Proceedings of the IEEE*, vol. 89, no. 3, pp. 227-239, 2001.

[8] Y. Nishi, “Lithium ion secondary batteries; past 10 years and the future,” *Journal of Power Sources*, vol. 100, no. 1, pp. 101-106, 2001.

[9] K. Lahiri, A. Raghunathan, S. Dey, and D. Panigrahi, “Battery-driven system design: a new frontier in low power design,” in *Proceedings of ASP-DAC/VLSI Design 2002. 7th Asia and South Pacific Design Automation Conference and 15h International Conference on VLSI Design*, Bangalore, India, 2002, pp. 261-267.

[10] R. Nagai, F. Kita, and M. Yamada, “Development of highly reliable high-capacity batteries for mobile devices and small-to medium-sized batteries for industrial applications,” *Energy*, vol. 450, no. 400, p. 350, 2003.

[11] K. Fujimoto and H. Morishita, *Modern Small Antennas*. USA: Cambridge University Press, 2014.

[12] A. Mieczakowski, T. Goldhaber, and J. Clarkson, “Culture, communication and change: Summary of an investigation of the use and impact of modern media and technology in our lives,” Engineering Design Centre, University of Cambridge, Cambridge, 2011.

[13] H. Z. Shi and A. Tennant, "Simultaneous, multichannel, spatially directive data transmission using direct antenna modulation," *IEEE Transactions on Antennas and Propagation*, Article vol. 62, no. 1, pp. 403-410, Jan 2014.

[14] Y. Ding and V. Fusco, "A review of directional modulation technology," *International Journal of Microwave and Wireless Technologies*, vol. 8, no. 7, pp. 981-993, Nov 2016.

[15] P. S. Carter and H. H. Beverage, "Early history of the antennas and propagation field until the end of World War I: Part I - antennas," *Proceedings of the IRE*, vol. 50, no. 5, pp. 679-682, 1962.

[16] J. D. Kraus, *Antennas*, 2nd ed. USA: McGraw-Hill, 1988.

[17] Apple Inc. (2017, Nov. 7). *Apple Watch series 2 - technical specifications* [online]. Available: https://support.apple.com/kb/SP746. (Accessed: 2017/12/11)

[18] H. A. Wheeler, "Fundamental limitations of small antennas," *Proceedings of the IRE*, vol. 35, no. 12, pp. 1479-1484, 1947.

[19] S. R. Best, "Small and fractal antennas," in *Modern Antenna Handbook*, C. A. Balanis, Ed. USA: John Wiley & Sons, 2008, pp. 475-528.

[20] J. L. Volakis, C. C. Chen, and K. Fujimoto, *Small Antennas: Miniaturization Techniques and Applications*. USA: McGraw-Hill, 2010.

[21] R. C. Hansen and R. E. Collin, *Small Antenna Handbook*. USA: John Wiley & Sons, 2011.

[22] C. A. Balanis, *Antenna Theory: Analysis and Design*, 4th ed. USA: John Wiley & Sons, 2016.

[23] A. Maiden, "Lithography in three dimensions using computer-generated holograms," Ph.D. dissertation, School of Engineering, Durham University, 2005.

[24] I. Gibson, D. W. Rosen, and B. Stucker, *Additive Manufacturing Technologies: Rapid Prototyping to Direct Digital Manufacturing*. USA: Springer, 2010.

[25] J. Hoerber, J. Glasschroeder, M. Pfeffer, J. Schilp, M. Zaeh, and J. Franke, "Approaches for additive manufacturing of 3D electronic applications," *Procedia CIRP*, vol. 17, pp. 806-811, 2014.

[26] *IEEE Standard for Definitions of Terms for Antennas*, IEEE Std 145-2013 (Revision of IEEE Std 145-1993), 2014.

[27] L. J. Chu, "Physical limitations of omni-directional antennas," *Journal of Applied Physics,* vol. 19, no. 12, pp. 1163-1175, 1948.

[28] H. A. Wheeler, "The radiansphere around a small antenna," *Proceedings of the IRE,* vol. 47, no. 8, pp. 1325-1331, 1959.

[29] J. S. McLean, "A re-examination of the fundamental limits on the radiation Q of electrically small antennas," *IEEE Transactions on Antennas and Propagation,* vol. 44, no. 5, pp. 672-676, 1996.

[30] R. F. Harrington, "Effect of antenna size on gain, bandwidth, and efficiency," *Journal of Research of the National Bureau of Standards,* vol. 64D, no. 1, pp. 1-12, 1960.

[31] R. C. Hansen, "Fundamental limitations in antennas," *Proceedings of the IEEE,* vol. 69, no. 2, pp. 170-182, 1981.

[32] H. L. Thal, "New radiation Q limits for spherical wire antennas," *IEEE Transactions on Antennas and Propagation,* vol. 54, no. 10, pp. 2757-2763, 2006.

[33] M. Gustafsson, C. Sohl, and G. Kristensson, "Physical limitations on antennas of arbitrary shape," *Proceedings of the Royal Society A: Mathematical Physical and Engineering Sciences,* vol. 463, no. 2086, pp. 2589-2607, 2007.

[34] H. R. Stuart, S. R. Best, and A. D. Yaghjian, "Limitations in relating quality factor to bandwidth in a double resonance small antenna," *IEEE Antennas and Wireless Propagation Letters,* vol. 6, pp. 460-463, 2007.

[35] D. Sievenpiper *et al.,* "Experimental validation of performance limits and design guidelines for small antennas," *IEEE Transactions on Antennas and Propagation,* vol. 60, no. 1, pp. 8-19, 2012.

[36] S. E. Sussman-Fort and R. M. Rudish, "Non-Foster impedance matching of electrically-small antennas," *IEEE Transactions on Antennas and Propagation,* vol. 57, no. 8, pp. 2230-2241, 2009.

[37] J. P. Gianvittorio and Y. Rahmat-Samii, "Fractal antennas: a novel antenna miniaturization technique, and applications," *IEEE Antennas and Propagation Magazine,* vol. 44, no. 1, pp. 20-36, 2002.

[38] J. M. Johnson and V. Rahmat-Samii, "Genetic algorithms in engineering electromagnetics," *IEEE Antennas and Propagation Magazine,* vol. 39, no. 4, pp. 7-21, 1997.

[39] D. Sievenpiper, "Review of theory, fabrication, and applications of high impedance ground planes," in *Metamaterials: Physics and Engineering*

Explorations, N. Engheta and R. W. Ziolkowski, Eds. USA: John Wiley & Sons, 2006, pp. 287-376.

[40] H. Liu, K. L. Ford, and R. J. Langley, "Miniaturised artificial magnetic conductor design using lumped reactive components," *Electronics Letters*, vol. 45, no. 6, pp. 294-295, 2009.

[41] H. L. Liu, K. L. Ford, and R. J. Langley, "Design methodology for a miniaturized frequency selective surface using lumped reactive components," *IEEE Transactions on Antennas and Propagation*, vol. 57, no. 9, pp. 2732-2738, 2009.

[42] R. W. Ziolkowski and A. Erentok, "Metamaterial-based efficient electrically small antennas," *IEEE Transactions on Antennas and Propagation*, vol. 54, no. 7, pp. 2113-2130, 2006.

[43] A. Erentok and R. W. Ziolkowski, "Metamaterial-inspired efficient electrically small antennas," *IEEE Transactions on Antennas and Propagation*, vol. 56, no. 3, pp. 691-707, 2008.

[44] Y. D. Dong and T. Itoh, "Metamaterial-based antennas," *Proceedings of the IEEE*, vol. 100, no. 7, pp. 2271-2285, 2012.

[45] H. R. Stuart and C. Tran, "Small spherical antennas using arrays of electromagnetically coupled planar elements," *IEEE Antennas and Wireless Propagation Letters*, vol. 6, pp. 7-10, 2007.

[46] S. R. Best and D. L. Hanna, "A performance comparison of fundamental small-antenna designs," *IEEE Antennas and Propagation Magazine*, vol. 52, no. 1, pp. 47-70, 2010.

[47] J. Anguera, L. Boada, C. Puente, C. Borja, and J. Soler, "Stacked H-shaped microstrip patch antenna," *IEEE Transactions on Antennas and Propagation*, vol. 52, no. 4, pp. 983-993, 2004.

[48] L. M. Feldner, C. T. Rodenbeck, C. G. Christodoulou, and N. Kinzie, "Electrically small frequency-agile PIFA-as-a-package for portable wireless devices," *IEEE Transactions on Antennas and Propagation*, vol. 55, no. 11, pp. 3310-3319, 2007.

[49] K. L. Wong, C. H. Chang, and Y. C. Lin, "Printed PIFA EM compatible with nearby conducting elements," *IEEE Transactions on Antennas and Propagation*, vol. 55, no. 10, pp. 2919-2922, 2007.

[50] R. B. Waterhouse and D. Novak, "Uni-planar folded meander line slot antenna with short circuit," *IEEE Transactions on Antennas and Propagation*, vol. 54, no. 11, pp. 3549-3551, 2006.

[51] R. N. Simons, *Coplanar Waveguide Circuits, Components, and Systems*. John Wiley & Sons, 2001.

[52] W. Hong and K. Sarabandi, "Low profile miniaturized planar antenna with omnidirectional vertically polarized radiation," *IEEE Transactions on Antennas and Propagation,* vol. 56, no. 6, pp. 1533-1540, 2008.

[53] S. I. Latif, L. Shafai, and S. K. Sharma, "Bandwidth enhancement and size reduction of microstrip slot antennas," *IEEE Transactions on Antennas and Propagation,* vol. 53, no. 3, pp. 994-1003, 2005.

[54] C. Hosung, R. L. Rogers, and L. Hao, "Design of electrically small wire antennas using a pareto genetic algorithm," *IEEE Transactions on Antennas and Propagation,* vol. 53, no. 3, pp. 1038-1046, 2005.

[55] E. E. Altshuler, "Electrically small genetic antennas immersed in a dielectric," in *IEEE Antennas and Propagation Society Symposium, 2004,* Monterey, USA, 2004, vol. 3, pp. 2317-2320.

[56] E. E. Altshuler, "A method for matching an antenna having a small radiation resistance to a 50-ohm coaxial line," *IEEE Transactions on Antennas and Propagation,* vol. 53, no. 9, pp. 3086-3089, 2005.

[57] C. T. Rodenbeck, "Planar miniature RFID antennas suitable for integration with batteries," *IEEE Transactions on Antennas and Propagation,* vol. 54, no. 12, pp. 3700-3706, 2006.

[58] U. Deepak, P. Mohanan, C. M. Nijas, and T. K. Roshna, "Compact CPW fed electrically small antenna for WLAN application," *Electronics Letters,* vol. 50, no. 2, pp. 62-64, 2014.

[59] B. Ghosh, S. M. Haque, D. Mitra, and S. Ghosh, "A loop loading technique for the miniaturization of non-planar and planar antennas," *IEEE Transactions on Antennas and Propagation,* vol. 58, no. 6, pp. 2116-2121, 2010.

[60] M. C. Tang and R. W. Ziolkowski, "A study of low-profile, broadside radiation, efficient, electrically small antennas based on complementary split ring resonators," *IEEE Transactions on Antennas and Propagation,* vol. 61, no. 9, pp. 4419-4430, 2013.

[61] N. Zhu and R. W. Ziolkowski, "Metamaterial-inspired, near-field resonant parasitic GPS antennas: designs and experiments," in *2011 IEEE International Symposium on Antennas and Propagation (APSURSI),* Spokane, USA, 2011, pp. 658-660.

[62] N. Zhu and R. W. Ziolkowski, "Broad-bandwidth, electrically small antenna augmented with an internal non-Foster element," *IEEE Antennas and Wireless Propagation Letters,* vol. 11, pp. 1116-1120, 2012.

[63] S. Zhu, K. L. Ford, A. Tennant, and R. J. Langley, "Miniaturised split ring antenna over loaded AMC surface," in *2010 Loughborough Antennas & Propagation Conference,* 2010, pp. 305-308.

[64] S. Zhu, D. G. Holtby, K. L. Ford, A. Tennant, and R. J. Langley, "Compact low frequency varactor loaded tunable SRR antenna," *IEEE Transactions on Antennas and Propagation,* vol. 61, no. 4, pp. 2301-2304, 2013.

[65] O. S. Kim, "Low-Q electrically small spherical magnetic dipole antennas," *IEEE Transactions on Antennas and Propagation,* vol. 58, no. 7, pp. 2210-2217, 2010.

[66] M. D. Chiou and S. Y. Chen, "An electrically small planar antenna using complementary split-ring resonators," in *2012 International Symposium on Antennas and Propagation (ISAP),* Nagoys, Japan, 2012, pp. 1313-1316.

[67] K. N. Madsen, Y. Zhou, and D. F. Sievenpiper, "A simplified low-Q electrically small magnetic dipole antenna," *IEEE Antennas and Wireless Propagation Letters,* vol. 15, pp. 1975-1978, 2016.

[68] M. T. Lee, K. M. Luk, K. W. Leung, and M. K. Leung, "A small dielectric resonator antenna," *IEEE Transactions on Antennas and Propagation,* vol. 50, no. 10, pp. 1485-1487, 2002.

[69] K. Y. Hui and K. M. Luk, "A miniature dielectric resonator loaded patch antenna," *IEEE Transactions on Antennas and Propagation,* vol. 53, no. 6, pp. 2118-2122, 2005.

[70] K. Y. Hui and K. M. Luk, "Bandwidth enhancement of small dielectric resonator loaded patch antenna," *IEEE Transactions on Antennas and Propagation,* vol. 54, no. 6, pp. 1882-1885, 2006.

[71] D. E. Anagnostou, A. A. Gheethan, A. K. Amert, and K. W. Whites, "A direct-write printed antenna on paper-based organic substrate for flexible displays and WLAN applications," *Journal of Display Technology,* vol. 6, no. 11, pp. 558-564, 2010.

[72] J. J. Adams *et al.,* "Conformal printing of electrically small antennas on three-dimensional surfaces," *Advanced Materials,* vol. 23, no. 11, pp. 1335-1340, 2011.

[73] J. J. Toriz-Garcia *et al.,* "Fabrication of a 3D electrically small antenna using holographic photolithography," *Journal of Micromechanics and Microengineering,* vol. 23, no. 5, p. 5, 2013, Art. no. 055010.

[74] C. Pfeiffer, X. Xu, S. R. Forrest, and A. Grbic, "Direct transfer patterning of electrically small antennas onto three-dimensionally contoured substrates," *Advanced Materials*, vol. 24, no. 9, pp. 1166-1170, 2012.

[75] M. Kgwadi, C. J. Vourch, D. J. Harrison, and T. D. Drysdale, "On-demand printing of antennas for TV white-space communications," in *2014 Loughborough Antennas and Propagation Conference (LAPC)*, Loughborough, UK, 2014, pp. 553-556.

[76] I. T. Nassar and T. M. Weller, "An electrically-small, 3-D cube antenna fabricated with additive manufacturing," in *2013 IEEE Radio and Wireless Symposium*, 2013, pp. 262-264.

[77] O. S. Kim, "3D printing electrically small spherical antennas," in *2013 IEEE Antennas and Propagation Society International Symposium (APSURSI)*, Orlando, USA, 2013, pp. 776-777.

[78] N. Arnal *et al.*, "3D digital manufacturing and characterization of antennas integrated in mobile handset covers," in *2015 IEEE 16th Annual Wireless and Microwave Technology Conference (WAMICON)*, Cocoa Beach, USA, 2015, pp. 1-5.

[79] H. Yuxiao, C. Oakley, P. Chahal, J. Albrecht, and J. Papapolymerou, "Aerosol Jet printed 24 GHz end-fire quasi-Yagi-Uda antenna on a 3-D printed cavity substrate," in *2017 International Workshop on Antenna Technology: Small Antennas, Innovative Structures, and Applications (iWAT)*, Athens, Greece, 2017, pp. 179-182.

[80] CST Computer Simulation Technology AG. (n.d.). *CST Microwave Studio - 3D EM simulation software* [online]. Available: https://www.cst.com/products/cstmws. (Accessed: 2017/12/11)

[81] D. M. Pozar, *Microwave Engineering*, 4th ed. USA: John Wiley & Sons, 2011.

[82] E. Bogatin, *Signal and Power Integrity – Simplified*, 2nd ed. USA: Prentice Hall, 2010.

[83] Rhode and Schwarz GmbH and Co. KG. (n.d.). *Brochures and Data Sheets for Product HF906 - Rhode and Schwarz United Kingdom* [online]. Available: https://www.rohde-schwarz.com/uk/brochure-datasheet/hf906/. (Accessed: 2017/12/11)

[84] E. Newman, P. Bohley, and C. Walter, "Two methods for the measurement of antenna efficiency," *IEEE Transactions on Antennas and Propagation*, vol. 23, no. 4, pp. 457-461, 1975.

[85] D. M. Pozar and B. Kaufman, "Comparison of three methods for the measurement of printed antenna efficiency," *IEEE Transactions on Antennas and Propagation*, vol. 36, no. 1, pp. 136-139, 1988.

[86] D. Agahi and W. Domino, "Efficiency measurements of portable-handset antennas using the Wheeler cap," *Applied Microwave and Wireless*, vol. 36, no. 1, pp. 34-42, 2000.

[87] H. J. Levinson, *Principles of Lithography*, 3rd ed. USA: SPIE Press, 2010.

[88] K. Seshan, Ed. *Handbook of Thin Film Deposition: Processes and Techniques*, 2nd ed. Noyes Publications, 2002.

[89] Y. N. Xia and G. M. Whitesides, "Soft lithography," *Annual Review of Materials Science*, vol. 28, no. 1, pp. 153-184, 1998.

[90] T. Ito and S. Okazaki, "Pushing the limits of lithography," *Nature*, vol. 406, no. 6799, pp. 1027-1031, 2000.

[91] D. Radtke and U. D. Zeitner, "Laser-lithography on non-planar surfaces," *Optics Express*, vol. 15, no. 3, pp. 1167-1174, 2007.

[92] M. J. Madou, *Manufacturing Techniques for Microfabrication and Nanotechnology* (Fundamentals of Microfabrication and Nanotechnology Vol. 2). CRC Press, 2011.

[93] J. W. Goodman, *Introduction to Fourier Optics*, 2nd ed. USA: McGraw-Hill, 1996.

[94] W. E. Frazier, "Metal additive manufacturing: a review," *Journal of Materials Engineering and Performance*, vol. 23, no. 6, pp. 1917-1928, 2014.

[95] C. Korner, "Additive manufacturing of metallic components by selective electron beam melting – a review," *International Materials Reviews*, vol. 61, no. 5, pp. 361-377, 2016.

[96] F. Calignano *et al.*, "Overview on additive manufacturing technologies," *Proceedings of the IEEE*, vol. 105, no. 4, pp. 593-612, 2017.

[97] *Standard Terminology for Additive Manufacturing – General Principles – Terminology*, ISO/ASTM52900-15, 2015.

[98] University of Sheffield. (n.d.). *About us - Engineering at Sheffield - Faculties - The University of Sheffield* [online]. Available: https://www.sheffield.ac.uk/faculty/engineering/about-us/research. (Accessed: 2017/12/11)

[99] Renishaw PLC. (n.d.). *Renishaw: enhancing efficiency in manufacturing and healthcare* [online]. Available: http://www.renishaw.com/en. (Accessed: 2017/12/11)

[100] Arcam AB. (n.d.). *Arcam AB - Additive Manufacturing for Implants and Aerospace, EBM* [online]. Available: http://www.arcam.com. (Accessed: 2017/12/11)

[101] EOS GmbH. (n.d.). *EOS e-Manufacturing Solutions: Industrial 3D Printing* [online]. Available: https://www.eos.info/en. (Accessed: 2017/12/11)

[102] MakerBot Industries LLC. (n.d.). *Connected 3D Printing Solutions* [online]. Available: https://www.makerbot.com. (Accessed: 2017/12/11)

[103] Y. L. Kuo and K. L. Wong, "Coplanar waveguide-fed folded inverted-F antenna for UMTS application," *Microwave and Optical Technology Letters*, vol. 32, no. 5, pp. 364-366, 2002.

[104] M. C. Huynh and W. Stutzman, "Ground plane effects on planar inverted-F antenna (PIFA) performance," *IEE Proceedings - Microwaves, Antennas and Propagation*, vol. 150, no. 4, pp. 209-213, 2003.

[105] S. R. Best, "A discussion on small antennas operating with small finite ground planes," in *IEEE International Workshop on Antenna Technology Small Antennas and Novel Metamaterials, 2006.*, 2006, pp. 152-155.

[106] J. T. Bernhard, J. J. Adams, M. D. Anderson, and J. M. Martin, "Measuring electrically small antennas: details and implications," in *2009 IEEE International Workshop on Antenna Technology (iWAT)*, Santa Monica, USA, 2009, pp. 1-4.

[107] The Editors of Encyclopædia Britannica. (2013, Oct. 04). *damascening* [online]. Available: https://www.britannica.com/art/damascening. (Accessed: 2017/12/11)

[108] M. I. Jais *et al.*, "Design analysis of 2.45 GHz meander line antenna (MLA)," in *2012 3rd International Conference on Intelligent Systems Modelling and Simulation (ISMS)*, Kota Kinabalu, Malaysia, 2012, pp. 628-631.

[109] J. J. Adams, S. C. Slimmer, T. F. Malkowski, E. B. Duoss, J. A. Lewis, and J. T. Bernhard, "Comparison of spherical antennas fabricated via conformal printing: helix, meanderline, and hybrid designs," *IEEE Antennas and Wireless Propagation Letters*, vol. 10, pp. 1425-1428, 2011.

[110] Wohlers Associates Inc. (n.d.). *Roadmap for Additive Manufacturing: Identifying the Future of Freeform Processing* [online]. Available: https://wohlersassociates.com/roadmap2009.html. (Accessed: 2017/12/11)

[111] Y. Huang, M. C. Leu, J. Mazumder, and A. Donmez, "Additive manufacturing: current state, future potential, gaps and needs, and recommendations," *Journal of Manufacturing Science and Engineering,* vol. 137, no. 1, Feb 2015, Art. no. 014001.

[112] J. A. Slotwinski and E. J. Garboczi, "Metrology needs for metal additive manufacturing powders," *JOM,* vol. 67, no. 3, pp. 538-543, 2015.

[113] S. K. Everton, M. Hirsch, P. Stravroulakis, R. K. Leach, and A. T. Clare, "Review of in-situ process monitoring and in-situ metrology for metal additive manufacturing," *Materials & Design,* vol. 95, pp. 431-445, 2016.

[114] S. Mufti, A. Tennant, and L. Seed, "Compact electrically small antenna for smart watch application," in *2015 University of Sheffield Engineering Symposium (USES)*, Sheffield, UK, 2015.

[115] T. H. Loh and M. Alexander, "New facility for minimally invasive measurements of electrically small antennas," in *2008 Loughborough Antennas and Propagation Conference (LAPC)*, Loughboroug, UK, 2008, pp. 313-316.

[116] M. Alexander, T. H. Loh, and A. L. Betancort, "Measurement of electrically small antennas via optical fibre," in *2009 Loughborough Antennas and Propagation Conference (LAPC)*, Loughborough, UK, 2009, pp. 653-656.

[117] Keysight. (2017, Mar. 07). *Basics of Measuring the Dielectric Properties of Materials (Application Note 5989-2589EN)* [online]. Available: http://literature.cdn.keysight.com/litweb/pdf/5989-2589EN.pdf. (Accessed: 2017/12/11)

[118] J. Baker-Jarvis, M. D. Janezic, and D. C. Degroot, "High-frequency dielectric measurements," *IEEE Instrumentation & Measurement Magazine,* vol. 13, no. 2, pp. 24-31, 2010.

[119] Keysight. (2016, Jan. 28). *Challenges and Solutions for Material Science/Engineering Testing Applications (Application Note 992-1182EN)* [online]. Available: https://literature.cdn.keysight.com/litweb/pdf/5992-1182EN.pdf. (Accessed: 2017/12/11)

[120] M. B. Heaney, "Electrical conductivity and resistivity," in *Electrical Measurement, Signal Processing, and Displays*, J. G. Webster, Ed. USA: CRC Press, 2003, pp. 7-1 - 7-14.

[121] NASA Jet Propulsion Laboratory. (2017, Apr. 18). *'Space Fabric' Links Fashion and Engineering* [online]. Available: https://www.jpl.nasa.gov/news/news.php?feature=6816. (Accessed: 2017/12/11)

[122] Z. X. Khoo *et al.*, “3D printing of smart materials: a review on recent progresses in 4D printing,” *Virtual and Physical Prototyping,* vol. 10, no. 3, pp. 103-122, 2015.

(This page intentionally left blank.)

Appendix – Computer Generated Holograms

This appendix provides an executive summary of the work done in the early stages of this project towards the realization of computer generated holograms (CGH). CGH are photolithographic masks synthesized using computational iterative algorithms, and may be manifested either digitally or physically. Popularized by Gabor in 1948, the concept of holography is centred on recording the interference pattern as an object is illuminated with a light source and the resulting wave-front intersected with a reference wave-front (the original illumination beam). The CGH mask stores these interference patterns; upon illumination by a suitable coherent light source, a virtual recreation of the original information is possible. The following sections give a brief overview of the laboratory setup, CGH algorithm, and the resulting CGH mask and captured optical field; lastly, some resources for further reading are listed.

Laboratory Setup

The laboratory setup used for the exposure stage in holographic lithography is shown in Figure A-1.

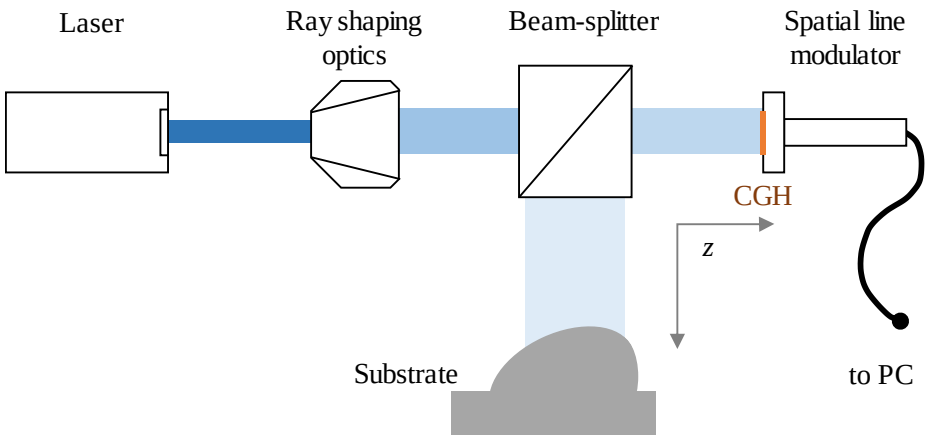

Figure A-1. Laboratory setup for holographic photolithography; exposure stage.

The optical source is a 110 mW rated laser (wavelength: 405 nm); the laser beam is subsequently expanded and collimated to be able to cover the entire area –

roughly 133 mm^2 (1920 by 1080 array of 8 μm^2 pixels) – of the spatial line modulator (digital projector) where the CGH is displayed. The desired image is projected a distance *z* cm from the CGH, where the antenna substrate is placed (metallized and covered with photoresist). In order to characterize the projected image, a specialized camera was placed in lieu of actual substrates, at the appropriate distance(s) away from the CGH.

Iterative Algorithm

The algorithm is initiated by creating a seed image based on the desired image to be propagated onto the observation plane. The seed image consists of an amplitude term closely resembling the desired image and a randomly generated phase component.

The resultant complex field is propagated to the far-field holographic plane using a transfer function, based on the angular spectrum propagation of optical fields. At the hologram plane, the phase information is retained, but amplitude is replaced by random values, or unity.

The new resultant field is subsequently propagated back to the image plane using an inverse transfer function. At this stage, the amplitude is compared to that of the desired image; if the error is above a certain threshold value, one of two alternating constraints is applied.

In the first case, phase information is retained and the amplitude replaced with the desired image amplitude. The resultant field replaces the original seed image, and the algorithm is repeated. In the second case, the phase information is combined with the phase of the original seed image, and the amplitude replaced with the desired image amplitude. The resultant field replaces the original seed image, and the algorithm is repeated. It was found experimentally that the alternating of constraints reduced stagnation in error reduction between the desired and propagated image amplitudes.

Once the error is acceptably low, the algorithm is terminated, and the phase information obtained at the holographic plane is saved as the CGH mask, after

some post-processing to make is suitable for display on the spatial line modulator.

Photographed Results

Figure A-2 shows a CGH designed to project an image 25 cm away; a photograph of the projected image is shown in Figure A-3.

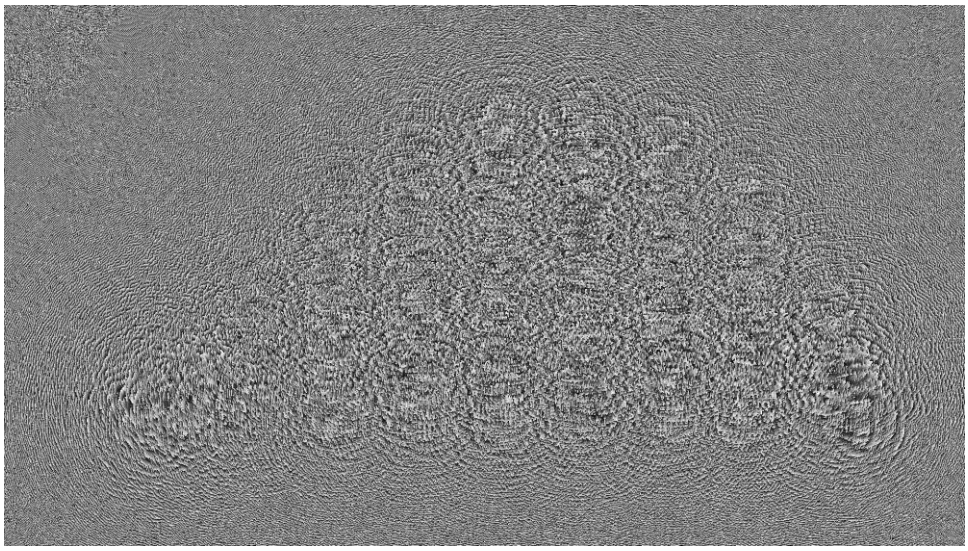

Figure A-2. 1920 by 1080 pixel CGH loaded onto SLM, designed to focus light on a single plane, 25 cm away. The CGH is designed to project the ‘negative’ of a digitated structure, intended to pattern antennas.

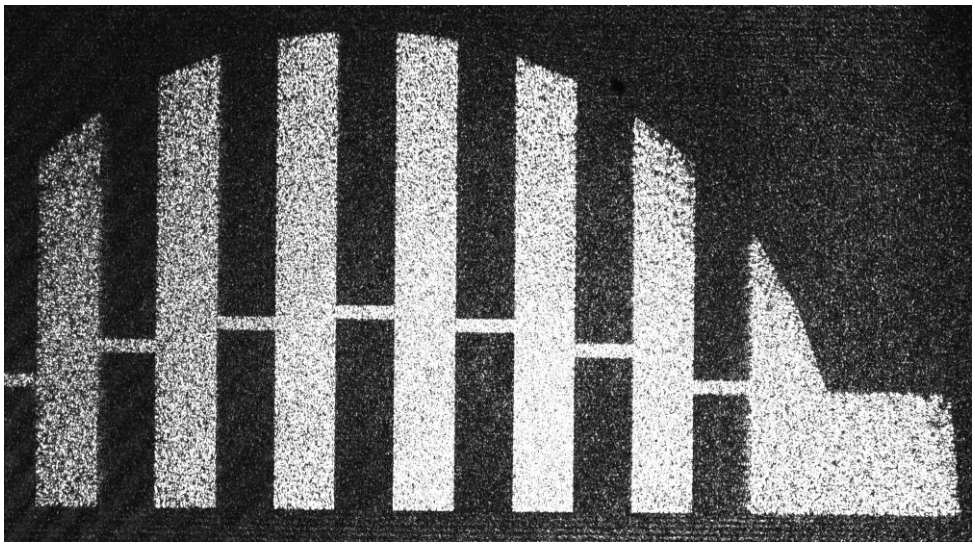

Figure A-3. Photographed image of light projected through CGH shown in Figure A-3. Laser operated at 110 mW; exposure time 120 seconds; minimum linewidth approximately 100 μm.

Further Reading

J. R. Fienup, “Phase retrieval algorithms: a comparison, “ *Applied Optics,* vol. 21, no. 15, pp. 2758-2769, 1982.

J. W. Goodman, *Introduction to Fourier Optics*, 2nd ed. USA: McGraw-Hill, 1996.

A. Maiden, “Lithography in three dimensions using computer-generated holograms,” Ph.D. dissertation, School of Engineering, Durham University, 2005.

D. G. Voelz, *Computational Fourier Optics: a MATLAB Tutorial*. USA: SPIE Press, 2011.

J. J. Cowling *et al.*, “Three-dimensional holographic lithography by an iterative algorithm,” *Optics Letters,* vol. 36, no. 13, pp. 2495-2497, 2011.

J. Cowling, “An Iterative Algorithm for Lithography on Three-Dimensional Surfaces,” Ph.D. dissertation, School of Engineering and Computing Sciences, Durham University, 2015.